A Dilating Vortex Particle Method for Compressible Flow with Application to Aeroacoustics

Thesis by
Jeff D. Eldredge

In Partial Fulfillment of the Requirements
for the Degree of
Doctor of Philosophy

California Institute of Technology
Pasadena, California

2002

(Defended July 30, 2001)

Acknowledgements

Even without proper perspective, I can state with assurance that these past five years have been wonderful, and for this I have several people to thank. Most certainly, my advisors, Professors Tim Colonius and Anthony Leonard. Each has given me his unrestricted attention during my tenure here, and their guidance has been the most important factor to my success. Tim has continually been the source of inspiration and enthusiasm, while Tony has provided me access to his wealth of experience and kindness and much-appreciated encouragement. In tandem they provide a wonderful balance. I also must thank the other members of my committee, Professors Dale Pullin and Melany Hunt. Also, I appreciate Professor Paul Dimotakis for his assistance in various capacities. And of course I must thank Professor Richard Murray for beer on Fridays at the Athenaeum.

I have developed a few lifelong friendships at Caltech that have in no small way made life much more bearable. Clancy Rowley and Martha Gallivan have, at the very least, given me dependable lunch companions. But they have been much more important than that. I also must thank Rob Griffin for being a consistent running partner—I only realized how important that was after he left! And I have plenty of gratitude for the friendships of Peter and Amy, Rob and Ann, and Chris and Shaney.

Of course I must thank my parents, because their love (and financial support!) are the real reasons that I've had the opportunities that I've had. When their funding ran out, I had a lot of help from a NSF Graduate Research Fellowship. For computational assistance I should thank CACR, and in particular Jan Lindheim for help when machines went down. I have been aided immeasurably by staff members, Dana Young, Lynn Burgess and Cecilia Lin. For other intangible assistance I thank Diet Coke®.

Most importantly I want to thank my wife and best friend, Asimina Sierou, who has given me companionship, security and confidence. And the story of our one-night trip to Las Vegas has given me cocktail party material for a lifetime!

A Dilating Vortex Particle Method
for Compressible Flow
with Application to Aeroacoustics

by
Jeff D. Eldredge

In Partial Fulfillment of the
Requirements for the Degree of
Doctor of Philosophy

Abstract

Vortex methods have become useful tools for the computation of incompressible fluid flow. In the present work, a vortex particle method for the simulation of unsteady two-dimensional compressible flow is developed and applied to several problems. The method is the first Lagrangian simulation method for the full compressible Navier-Stokes equations. By decomposing the velocity into irrotational and solenoidal parts, and using particles that are able to change volume and that carry vorticity, dilatation, enthalpy, entropy, and density, the equations of motion are satisfied. A general deterministic treatment of spatial derivatives in particle methods is developed by extending the method of particle strength exchange through the construction of higher-order-accurate, non-dissipative kernels for use in approximating arbitrary differential operators. The application of this technique to wave propagation problems is thoroughly explored. A one-sided operator is developed for approximating derivatives near the periphery of particle coverage; the operator is used to enforce a non-reflecting boundary condition for the absorption of acoustic waves at this periphery. Remeshing of the particles and the smooth interpolation of their strengths are addressed, and a criterion for the frequency of remeshing is developed based on the principal axes of the rate-of-strain tensor. The fast multipole method for the fast summation of the velocity field is

adapted for use with compressible particles. The new vortex method is applied to co-rotating and leapfrogging vortices in compressible flow, with the acoustic field computed using a two-dimensional Kirchhoff surface, and the results agree well with those of previous work or analytical prediction. The method is also applied to the baroclinic generation of vorticity, and to the steepening of waves in the one-dimensional Burgers' equation, with favorable results in both cases.

Contents

List of Figures

List of Tables

Chapter 1

Introduction

Vortex particle methods are a class of Lagrangian numerical methods for the simulation of incompressible fluid flows of which vorticity is an integral component. Significant development in the past three decades has made these methods an attractive alternative to traditional fixed-grid computational schemes such as finite difference and spectral methods. By describing the flow from the material element perspective, they intimately connect the solution with the underlying physics. The goal of the present work is to extend these methods, while retaining as many of their desirable properties as possible, to compressible flows, including those involving sound generation.

1.1 A brief account of vortex sound theory

The study of flow-generated sound, or "aeroacoustics," has been motivated in the past fifty years by several key problems in military and industrial applications. Among these problems are jet noise and the sound from other shear instabilities, combustion acoustics, and the noise from helicopter rotors.

That there is some relationship between the eddying motion in a flow and the sound that it generates has been suspected since the nineteenth century.[1] Early

[1] Although it is difficult to find classical evidence of the recognition that vorticity and sound are related, it is at least interesting to note that the words *warble* (to sing) and *whirl* (to turn) are derived from the same origin in Old French (*werbler*) (Oxford English Dictionary, 1989), a

work in the investigation of the vortex street behind a cylinder was motivated by the "singing" of telegraph wires, and Rayleigh (1894) states that the origin of the sound is "doubtless connected with the instability of vortex sheets." For the rigorous mathematical relationship of vorticity and acoustics, we can find a more concrete origin. While Lighthill (1952) is credited as the progenitor of modern aeroacoustics theory with his identification of an equivalent quadrupole field as the basic source of sound, it remained for later researchers to explicitly identify vorticity as a primary culprit. Chu and Kovásznay (1958) presented a systematic analysis of the higher-order interactions between the three basic modes of fluctuation in the linearized equations of motion: the entropy mode, the vortical mode and the acoustic mode. Their analysis clearly exhibited the importance of vorticity-vorticity and vorticity-acoustic interactions in the generation and processing of sound, but without directly expressing these interactions in terms of the vorticity.

Powell (1964) approached the problem from a different position, using physical arguments with later mathematical justification to posit that aerodynamic sound is the result of the motion of vorticity. For unbounded vortical flows of low Mach number, he argued that the largest contribution to the farfield pressure fluctuations comes from a dipole "source" term proportional to $\nabla \cdot (\boldsymbol{\omega} \times \mathbf{u})$. His expression for these fluctuations can ultimately be written in the form

$$p'(\mathbf{x},t) = -\frac{\rho_\infty}{4\pi a_\infty^2 |\mathbf{x}|^3} \frac{\partial^2}{\partial t^2} \int (\mathbf{x}\cdot\mathbf{y})\,(\mathbf{x}\cdot\boldsymbol{\omega}\times\mathbf{u})\,(\mathbf{y}, t-|\mathbf{x}|/a_\infty)\,d\mathbf{y}.$$

For the pressure field that arises in such an arrangement, Powell gave the name "vortex sound," a term that has persisted since. Howe (1975) recast the equations in the form of a convective wave equation for the stagnation enthalpy, thereby retaining the dipole source of Powell but without the complication of arguing for the removal of the density from the source. Although his equation is exact, it

relationship that is made manifest by the German word *Wirbel* for vortex. Unfortunately, the etymology does not reveal much about the reason for this commom ancestry; the explanation of the Oxford English Dictionary is disappointing.

does not readily permit solution. Only for low Mach number flows can a Green's function be found.

More recently, Möhring (1997) has been able to arrange the equations of motion into the form of a convective wave equation for the stagnation enthalpy, similar to that of Howe in that it emphasizes the vorticity as a source mechanism, but different in that his operator is self-adjoint and thus leads to a reciprocity principle. Solution of his equation is also assisted by the low Mach number assumption.

Möhring (1978) attempted to circumvent the difficulties associated with a source term that requires knowledge of both the local vorticity and velocity by forming an expression that is linear in the vorticity. His procedure requires finding a vector Green's function for the flow of interest, which is only possible for small Mach number. For flows of this type, his formula provides a useful description of the acoustic field in terms of the vorticity moments alone. Kambe (1986) used the method of matched asymptotic expansions to derive the same formula, without resorting to the vector Green's function. He has applied the formula to several problems that also allowed laboratory investigation, and has shown that the results agree remarkably well.

It is apparent that most aeroacoustic theories as predictive tools depend crucially on the assumption of low Mach number. Also, as Crow (1970) demonstrates, many also depend on the limited extent of the vortical region with respect to the eddy size. For instance, both Lighthill's and Powell's theories cast the equations of motion into the form of a linear wave equation for a quantity such as the pressure, with the expectation that those terms that are designated for the right-hand side can duly be treated as "source" terms, known *a priori*. However, this can only be justified under certain conditions. These terms also necessarily contain the *processing* effects of sound by the flow, such as refraction or scattering, as well as the modification of the flow itself by compressibility. To allow these effects to be neglected, the extent of the flow region, L, must be small in comparison with the wavelength of sound—so the character of a wave is not significantly changed by passing across the flow region—and the Mach number, M, must be small—so

that the flow can be regarded as essentially incompressible and solved for without regard for the resultant acoustic field. Equivalently, it is required that $M \ll 1$ and $L/l \sim 1$, where l is a typical eddy size.

When either of these conditions is violated, it is difficult to make any predictions about the resulting acoustic field. Even if the wave operator is amended to include some convective and refractive effects, compressibility can still significantly modify an extensive flow region. In the absence of simple cause-and-effect relationships, it is the role of computational aeroacoustics (CAA) to provide tools by which to learn something about the physics, to both complement and supplement experimental measurement. Moreover, CAA can be used to validate the theories that can be extracted. Clearly a numerical method which emphasizes the motion of vorticity in a compressible medium can be used to further explore, and possibly exploit, the relationship between vorticity and sound. It is the goal of the present work to develop such a tool.

Certainly there are other, proven computational methods that provide the necessary capabilities. The works of Colonius, Lele and Moin (1997) and Mitchell, Lele and Moin (1995) have demonstrated that high-order-accurate finite difference schemes can be sufficient. It is not the intention of the present work to supplant these methods with a superior scheme. Rather, we wish to furnish the CAA toolbox with a new set of tools that have their own unique advantages. Specifically, the Lagrangian description will provide an arguably more physical reference frame from which to view acoustical phenomena. Furthermore, the grid-free description may allow simulation of flows in complex geometries that fixed grid schemes cannot handle. Also, the present method will inherently decouple the velocity into irrotational and solenoidal components; these can be exploited in an acoustic investigation in a way not available in existing computational schemes. Finally, a velocity-based numerical scheme must deal with the pressure in a fundamentally different way with and without compressibility present; with the vorticity description, the present method can be adapted to incompressible flow computation with the flip of a switch. Note, however, that the inherent inefficiency associated with

low Mach number solution is retained when the compressible version of the equations is used.

1.2 Vortex and other particle methods

The development and application of incompressible vortex methods are described in several detailed reviews (e.g., Leonard (1980); Sarpkaya (1989)) and a recent book by Cottet and Koumoutsakos (2000). The vortex particle method describes a vorticity field by a collection of smooth, radially-symmetric particles that interpolate the field. Through the Biot-Savart integral, each particle contributes to the overall velocity field, which, in turn, advects the particles. As a method that consists of computational elements that convect with the flow, it can be regarded as a member of the larger class known as "particle methods."

Particle methods have been used in the context of compressible flows previously. Most notable of these methods is smoothed particle hydrodynamics (SPH), first introduced by Gingold and Monaghan (1977) (see also Monaghan (1985)) for astrophysical fluid dynamic applications. It relies on the same principle of kernel estimation as vortex methods, although it focuses on the velocity as the primary variable instead of the vorticity. Since its conception SPH has been used in several contexts outside of astrophysics: Monaghan and Gingold (1983), and later Monaghan (1997), applied the method to a shock-tube simulation using a special artificial viscosity to suppress spurious oscillations. The method has also been used for computing the Rayleigh-Taylor instability (Monaghan, 1989) and for blast waves.

Anderson (1985) developed a vortex method for flows in which the fluctuations in the density are small enough that the Boussinesq approximation is applicable. His method avoids computing the density gradient in the external force term by tracking this quantity directly rather than the density itself. The transport-element method developed by Krishnan and Ghoniem (1992) is an extension of this approach, except that it uses the observation that the density gradient in such

a flow is proportional to the length of a material line element—or alternatively, the distance between neighboring computational elements. The method has been applied to the Rayleigh-Taylor instability (Krishnan and Ghoniem, 1992) and to the investigation of combustion in shear layers (Soteriou and Ghoniem, 1998). Finally, recent work by Daeninck (2000) has extended the vortex particle method to non-isothermal incompressible flows by tracking the temperature along with the vorticity.

Sound generation has also been explored using incompressible vortex methods by exploiting the low Mach number approximation to ignore compressibility effects in the nearfield. Knio, Collorec and Juvé (1995) explored the sound emission from a complex system of vortices by simulating their motion in an incompressible medium and then computing the farfield sound using both the Powell-Hardin formulation and the Möhring analogy. Pothou et al. (1996) used both the vortex particle and vortex filament methods for three-dimensional simulations; they calculated the resulting acoustic field with acoustic analogies.

1.3 The present method

The present method will require no assumption regarding the Mach number. We will utilize several recent developments in incompressible vortex methods to make the extension to compressible flows. These include the deterministic method for the treatment of diffusion developed by Degond and Mas-Gallic (1989), now referred to as particle strength exchange (PSE). As we will show in Chapter 3, PSE also furnishes a useful framework for treating other physical phenomena, such as wave propagation. The expensive summation operation that once prohibited simulations of particle systems involving more than a few thousand particles has been alleviated with the development of fast methods, such as the fast multipole method (FMM) of Greengard and Rokhlin (1987). These methods reduce the number of direct particle-particle interactions by computing interactions between clusters of particles where possible. We will adapt the FMM to compressible vortex particles.

Inevitably some of the strength of vortex methods is compromised when applied to general compressible flows. Because the computational elements will carry radiating quantities in addition to vorticity, the region that they fill will necessarily be larger. But incompressible simulations that include viscosity require a surrounding buffer of particles with zero vorticity that accept the diffused quantity; in the present method waves will be allowed to propagate by the same principle of strength exchange and thus particle coverage need not be significantly larger, especially if sufficiently general boundary conditions may be developed (we propose a simple, but limited, technique in the present work). More importantly, it is inappropriate to demand that the method retain the same economy of particle coverage. We expect our method to capture the vorticity dynamics *as well as* some portion of the acoustic field, and such a task requires the particles to extend farther.

The compressible method, which we refer to as the dilating vortex particle method (DVPM), is developed progressively, relying on existing techniques where possible. In Chapter 2 the Helmholtz decomposition of the velocity field will allow incorporation of the dilatation of fluid elements into the determination of the velocity. Computational elements that expand and contract according to the dilatation are introduced in this section, as well as a set of equations governing their strengths, based on the compressible equations of motion. We will briefly illustrate some of the subtle effects that are contained in these equations through asymptotic expansion. In Chapter 3 the technique of particle strength exchange is generalized to arbitrary derivatives, and the consequences of such an extension are discussed at length. Most notably, the dispersive properties of the PSE operator are analyzed, as well as its behavior during the distortion of the particle grid. The other essential elements of the DVPM are developed in Chapter 4. These include domain truncation and the transmission of waves out of particle coverage—a scheme based on the local boundary conditions of Engquist and Majda (1977) is described using a "one-sided" derivative treatment developed in Chapter 3; fast summation of the velocity field, using the FMM; and particle remeshing, which

proves to be critical to the success of the method. In Chapter 5 the computation of the outer acoustic field from the simulation results is discussed. Finally, the method is demonstrated on several model problems in Chapter 6. Conclusions and future extensions of the method are discussed in Chapter 7.

Chapter 2

The Dilatating Vortex Particle Method

The basic principles of the method are described here, although the treatment of spatial derivatives is given only cursory discussion and will be presented in detail in Chapter 3. Also, practical aspects of implementing the method will be attended to in Chapter 4. The equations of motion are developed here and their treatment by particles is discussed. The last section of this chaper will illustrate some of the delicate effects that are contained in these equations and which a computational method must be able to treat with care.

2.1 Particle convection and dilatation

Consider the Helmholtz decomposition of the velocity field into solenoidal and irrotational components

$$\mathbf{u} = \mathbf{u}_s + \mathbf{u}_{ir}, \tag{2.1}$$

where each is derived from a potential: $\mathbf{u}_s \equiv \nabla \times \mathbf{A}$ and $\mathbf{u}_{ir} \equiv \nabla\varphi$. If $\mathbf{A}$ is chosen to be solenoidal, then the curl and the divergence of the velocity lead to, respectively,

$$\nabla^2\mathbf{A} = -\nabla \times \mathbf{u} \equiv -\boldsymbol{\omega}, \tag{2.2a}$$

$$\nabla^2\varphi = \nabla \cdot \mathbf{u} \equiv \theta. \tag{2.2b}$$

When equations (2.2) are solved using the Green's function for the negative Laplacian, G, the inversion leads to the following expressions for the potentials (within arbitrary constants):

$$\mathbf{A} = G \star \boldsymbol{\omega}, \tag{2.3a}$$

$$\varphi = -G \star \theta, \tag{2.3b}$$

where $\star$ denotes convolution. If present, an arbitrary harmonic component could be added to either expression; it will be ignored here. Substitution of these expressions into the velocity decomposition above leads to a relation for the velocity in terms of the vorticity and dilatation:

$$\mathbf{u} = (\mathbf{K}\times) \star \boldsymbol{\omega} - \mathbf{K} \star \theta, \tag{2.4}$$

where $\mathbf{K} \equiv \nabla G$. The first term on the right-hand side of (2.4) is the Biot-Savart integral, and the second is its counterpart in dilatation.

As in the incompressible vortex particle method, the vorticity field is approximated (interpolated) by a set of regularized particles, or "blobs," each of which possesses its own distribution of vorticity. In the present method these blobs will also carry dilatation to approximate that field. The particle representations of the two fields are

$$\widetilde{\boldsymbol{\omega}}(\mathbf{x}, t) = \sum_p \boldsymbol{\Gamma}_p(t) \zeta_\varepsilon(\mathbf{x} - \mathbf{x}_p(t)), \tag{2.5a}$$

$$\widetilde{\theta}(\mathbf{x}, t) = \sum_p Q_p(t) \zeta_\varepsilon(\mathbf{x} - \mathbf{x}_p(t)), \tag{2.5b}$$

where $\{\mathbf{x}_p(t)\}$ and $\{V_p(t)\}$ are the positions and volumes of the particles, respectively. A particle's vorticity strength is $\boldsymbol{\Gamma}_p = V_p \boldsymbol{\omega}_p$, where $\boldsymbol{\omega}_p(0) = \boldsymbol{\omega}(\mathbf{x}_p(0))$, and its dilatation strength is $Q_p = V_p \theta_p$, where $\theta_p(0) = \theta(\mathbf{x}_p(0))$. The blob function ζ is scaled by ε, the radius of the blob: $\zeta_\varepsilon(\mathbf{x}) = \zeta(\mathbf{x}/\varepsilon)/\varepsilon^d$, where d is the physical dimension. In the limit of $\varepsilon \to 0$, the blob function approaches a Dirac measure

and the particles approach vortex-source singularities. The particles are associated with material elements and thus their positions change according to the local fluid velocity,

$$\frac{d\mathbf{x}_p}{dt} = \mathbf{u}(\mathbf{x}_p), \tag{2.6}$$

and their volumes change according to the local fluid dilatation,

$$\frac{dV_p}{dt} = Q_p. \tag{2.7}$$

The approximations (2.5) are introduced to the velocity expression (2.4) and serve to desingularize the velocity kernels. Thus, the ordinary differential equation that governs the particle positions is

$$\frac{d\mathbf{x}_p}{dt} = \sum_q \mathbf{K}_\varepsilon(\mathbf{x}_p - \mathbf{x}_q) \times \mathbf{\Gamma}_q(t) - \sum_q Q_q(t)\mathbf{K}_\varepsilon(\mathbf{x}_p - \mathbf{x}_q), \tag{2.8}$$

where $\mathbf{K}_\varepsilon = \mathbf{K} \star \zeta_\varepsilon$ is the smoothed velocity kernel. Equation (2.8) exhibits the collaborative character of the vortex method. Each particle possesses its own velocity field, due to its vorticity and its dilatation; the superposition of all of the particles' contributions defines the velocity field to which each particle is subjected to. Note that the commonly-used notion in vortex methods that the particle "induces" a velocity is erroneous and misleading in the present context. In a compressible flow, any process of induction must necessarily involve a time delay as information requires a finite time to convect. The velocity field from (2.4) is simply that which is consistent with the instantaneous distribution of vorticity and dilatation, through the satisfaction of elliptic equations.

The convergence of the incompressible vortex blob method has been demonstrated by Hald (1979), and later by Beale and Majda (1982), Raviart (1983) and Anderson and Greengard (1985). In each it is shown that errors in the method arise because of the smoothing of the velocity kernel and the discretization of the vorticity field by particles. A necessary constraint for convergence is that the par-

ticles overlap, i.e., the ratio of blob radius to particle spacing, $\kappa = \varepsilon/\Delta x$, must be greater than unity. In the present method, no additional errors have been introduced by including the dilatational component in the velocity field. The smoothing error is determined by the choice of blob function, ζ; the order of accuracy, r, is dependent upon ζ satisfying a set of conditions on its moments:

$$\int \zeta(\mathbf{x})\, d\mathbf{x} = 1, \tag{2.9a}$$

$$\int \mathbf{x}^\alpha \zeta(\mathbf{x})\, d\mathbf{x} = 0, \quad |\alpha| \in [1, r-1], \tag{2.9b}$$

where $\alpha = (\alpha_1, \alpha_2, \ldots, \alpha_d)$ is a multi-index, $|\alpha| = \alpha_1 + \alpha_2 + \cdots + \alpha_d$ and $\mathbf{x}^\alpha = x_1^{\alpha_1} x_2^{\alpha_2} \cdots x_d^{\alpha_d}$. We refer the reader to Beale and Majda (1985) and Winckelmans and Leonard (1993) for more complete discussions of the construction of the blob function. However, the construction is very similar to that of PSE kernels and remeshing interpolation kernels (see Chapter 3 and §4.2).

From hereon the flow will be assumed two-dimensional (extension to three-dimensional flow is discussed in §2.2), so the vorticity and the vector potential each have only a single component: $\boldsymbol{\omega} = \omega \hat{\mathbf{e}}_3$ and $\mathbf{A} = \psi \hat{\mathbf{e}}_3$. The two-dimensional Green's function for the negative Laplacian is $G = -\frac{1}{2\pi} \log |\mathbf{x}|$, from which follows the velocity kernel,

$$\mathbf{K}(\mathbf{x}) \equiv \nabla G(\mathbf{x}) = -\frac{\mathbf{x}}{2\pi |\mathbf{x}|^2}. \tag{2.10}$$

The mollified velocity kernel is, after accounting for the radial symmetry of the blob function,

$$\mathbf{K}_\varepsilon(\mathbf{x}) = -\frac{\mathbf{x}}{2\pi |\mathbf{x}|^2} q(|\mathbf{x}|/\varepsilon), \tag{2.11}$$

where $q(r) \equiv 2\pi \int_0^r \tau \zeta(\tau)\, d\tau$. In our implementation we use a Gaussian template (equation (3.11)) for the blob function. The 2nd-order-accurate function derived from this template is the commonly-used Gaussian $\zeta(\mathbf{x}) = \frac{1}{\pi} e^{-|\mathbf{x}|^2}$. With this

choice the smoothed velocity kernel becomes

$$\mathbf{K}_\varepsilon(\mathbf{x}) = -\frac{\mathbf{x}}{2\pi|\mathbf{x}|^2}\left(1 - e^{-|\mathbf{x}|^2/\varepsilon^2}\right). \tag{2.12}$$

However, we use a higher-order-accurate function for our applications, as described in Chapter 6.

2.2 Equations of motion

Equation (2.8) requires the values of the vorticity and dilatation of every particle. Equations for their evolution are developed by taking the curl and divergence of the momentum equations, respectively. For simplicity, the medium is assumed to be a calorically perfect gas with constant and uniform properties. In addition to the vorticity and dilatation, the flow is described by the specific enthalpy (h), the specific entropy (s) and the density (ρ). The particle representation of these variables is

$$\tilde{f}(\mathbf{x}, t) = \sum_p V_p f_p \zeta_\varepsilon(\mathbf{x} - \mathbf{x}_p(t)), \tag{2.13}$$

where f is either h, s or ρ. The variables are made dimensionless with a compressible scaling, using a characteristic flow length, L; a characteristic speed of sound, a_∞, and density, ρ_∞; the (constant) dynamic viscosity, μ; and the specific heat capacity at constant pressure, c_p:

$$\begin{aligned}
&\widetilde{\mathbf{x}} = \mathbf{x}/L, && \widetilde{\mathbf{u}} = \mathbf{u}/a_\infty, && \widetilde{\omega} = \omega L/a_\infty,\\
&\widetilde{t} = a_\infty t/L, && \widetilde{\theta} = \theta L/a_\infty, && \widetilde{h} = h/a_\infty^2,\\
&\widetilde{s} = (s - s_\infty)/c_p, && \widetilde{\rho} = \rho/\rho_\infty, && \widetilde{a^2} = a^2/a_\infty^2,\\
&\widetilde{T} = c_p T/a_\infty^2, && \widetilde{\Phi} = \Phi L^2/(\mu a_\infty^2).
\end{aligned}$$

This scaling leads to an acoustic Reynolds number, $Re = \rho_\infty a_\infty L/\mu$, which can be related to a hydrodynamic definition through a characteristic Mach number: $\widetilde{Re} = M_0 Re$, where $M_0 = U_0/a_\infty$ and U_0 is a characteristic flow velocity. The Prandtl

number is $Pr = \mu c_p/k$, where k is the thermal conductivity. The bulk viscosity is assumed negligible. Note that, because the medium is a calorically perfect gas, the temperature and the enthalpy are equivalent after nondimensionalization.

Partitioning the momentum equations as described results in the following dimensionless set for two-dimensional flow (where the tildes have been removed for brevity):

$$\frac{D\omega}{Dt} = -\omega\theta + \nabla \times (h\nabla s) \cdot \hat{\mathbf{e}}_3 + \frac{1}{Re}\nabla \times \left[\frac{1}{\rho}\left(\frac{4}{3}\nabla\theta - \nabla \times \omega\right)\right] \cdot \hat{\mathbf{e}}_3, \tag{2.14a}$$

$$\frac{D\theta}{Dt} = -\nabla^2 h - \nabla\mathbf{u} : (\nabla\mathbf{u})^T + \nabla \cdot (h\nabla s) + \frac{1}{Re}\nabla \cdot \left[\frac{1}{\rho}\left(\frac{4}{3}\nabla\theta - \nabla \times \omega\right)\right]. \tag{2.14b}$$

The entropy equation is

$$\frac{Ds}{Dt} = \frac{1}{Re}\frac{\Phi}{\rho h} + \frac{1}{RePr}\frac{1}{\rho h}\nabla^2 h, \tag{2.14c}$$

where the viscous dissipation term, Φ, is expressed as

$$\Phi = \omega^2 + 2\nabla\mathbf{u} : (\nabla\mathbf{u})^T - \frac{2}{3}\theta^2. \tag{2.14d}$$

This form is especially convenient for computation because it shares with (2.14b) the same double contraction of the velocity gradient tensor with its transpose. The continuity equation is

$$\frac{D\rho}{Dt} = -\rho\theta, \tag{2.14e}$$

and the enthalpy is governed by an equation that is derived from (2.14c) and (2.14e):

$$\frac{Dh}{Dt} = -a^2\theta + \frac{\gamma}{Re}\frac{\Phi}{\rho} + \frac{\gamma}{RePr}\frac{1}{\rho}\nabla^2 h, \tag{2.14f}$$

where γ is the ratio of specific heats (taken to be 1.4), and $a^2 = (\gamma - 1)h$.

Far from the nonlinear flow region, the vorticity is zero and diffusive effects are negligible, so the entropy is approximately uniform. The remaining field quantities (enthalpy, dilatation and density), denoted collectively as f, undergo only small fluctuations f' from their mean values, about which the equations can be linearized. To first order in these small fluctuations the equations reduce to that of classical acoustics, the linear homogeneous wave equation,

$$\frac{\partial^2 f'}{\partial t^2} - \nabla^2 f' = 0.$$

At infinity, it is appropriate to impose that the waves there are only outgoing (Sommerfeld, 1964):

$$\lim_{r\to\infty} r^{1/2} \left(\frac{\partial f'}{\partial t} - \frac{\partial f'}{\partial r} \right) = 0. \tag{2.15}$$

Of course, a computational domain represents only a finite portion of the infinite flow domain, so we seek some expression of this condition that is approximately valid at the periphery of the particle coverage. In §4.3 we will adapt a member of the hierarchy of conditions of Engquist and Majda (1977) to accomplish this.

Evolution equations for the particle strengths are formed by appropriate treatment of the terms contained in equations (2.14). Much of the treatment is adapted from incompressible vortex methods, but some new ideas are necessary. Most spatial derivative terms are approximated by PSE, originally developed for use in convection-diffusion equations but extendable to more general contexts. This will be discussed in detail in Chapter 3; in essence, the differential operator D^β (β is a multi-index denoting the number of derivatives in each direction) is replaced by an integral operator, L^ε:

$$D^\beta f(\mathbf{x}) \approx L^\varepsilon f(\mathbf{x}) = \frac{1}{\varepsilon^{|\beta|}} \int_{I\!R^2} \left(f(\mathbf{y}) \mp f(\mathbf{x}) \right) \eta_\varepsilon^\beta (\mathbf{x} - \mathbf{y})\, d\mathbf{y},$$

where η^β is the PSE kernel appropriate for this derivative operator and $\eta_\varepsilon(\mathbf{x}) =$

$\eta(\mathbf{x}/\varepsilon)/\varepsilon^2$. The integral is subsequently discretized by a quadrature over the particles:

$$D^\beta f(\mathbf{x}_p) \approx \frac{1}{\varepsilon^{|\beta|}} \sum_q V_q \left(f_q \mp f_p\right) \eta_\varepsilon^\beta(\mathbf{x}_p - \mathbf{x}_q).$$

The sign is chosen depending on the order of derivative ($-$ for even derivatives and $+$ for odd). With the appropriate sign, application of this technique in many contexts results in exact conservation of important global quantities (e.g., the circulation). Failure to conserve a quantity such as this can have deleterious consequences on the results of a simulation.

PSE is used for Laplacian terms, as well as for the first derivatives of enthalpy, entropy, dilatation and vorticity, with separate kernels used for each order of derivative. The boundary treatment, adapted from (2.15), will be discussed in §4.3 and will also use a form of PSE for approximating the spatial derivative. For the curl terms in (2.14a), the PSE operator is applied first to the inner derivatives, and then to the outer derivatives only after the products have been evaluated; a similar procedure is followed for analogous divergence terms in (2.14b). Following this procedure ensures conservation of circulation, which would not be guaranteed if the curl was first applied to each factor in the products and then the derivatives discretized.

Spatial derivatives in the velocity are treated somewhat differently. It is noted that the double contraction term, $\nabla\mathbf{u} : (\nabla\mathbf{u})^T$, resembles the vortex stretching term in three dimensions, for which Anderson and Greengard (1985) have developed a scheme in which the gradient operator is applied to the right-hand side of (2.8), acting directly on the smoothed velocity kernels. Applying this technique leads to

$$(\nabla\mathbf{u})_p = \sum_q \Gamma_q(t) \nabla \left(\mathbf{K}_\varepsilon \times \hat{\mathbf{e}}_3\right)(\mathbf{x}_p - \mathbf{x}_q) - \sum_q Q_q(t) \nabla \mathbf{K}_\varepsilon(\mathbf{x}_p - \mathbf{x}_q). \qquad (2.16)$$

The new kernel $\mathbf{R}_\varepsilon = \nabla \mathbf{K}_\varepsilon$ can be written in terms of ζ and q as

$$R_\varepsilon^{ij}(\mathbf{x}) = \frac{\partial K_{\varepsilon,i}}{\partial x_j}(\mathbf{x}) = \left(-\zeta_\varepsilon(\mathbf{x}) + \frac{q(|\mathbf{x}|/\varepsilon)}{\pi |\mathbf{x}|^2} \right) \frac{x_i x_j}{|\mathbf{x}|^2} - \frac{q(|\mathbf{x}|/\varepsilon)}{2\pi |\mathbf{x}|^2} \delta_{ij}.$$

Note that $\lim_{r->0} R_\varepsilon^{ij}(r) = \frac{1}{2}\zeta_\varepsilon(0)\delta_{ij}$. As an example, if the 2nd-order Gaussian function is used, then

$$R_\varepsilon^{ij}(\mathbf{x}) = \frac{1}{\pi |\mathbf{x}|^2} \left[1 - \left(1 + \frac{|\mathbf{x}|^2}{\varepsilon^2} \right) e^{-|\mathbf{x}|^2/\varepsilon^2} \right] \frac{x_i x_j}{|\mathbf{x}|^2} - \frac{1}{2\pi |\mathbf{x}|^2} \left(1 - e^{-|\mathbf{x}|^2/\varepsilon^2} \right) \delta_{ij}.$$

It is certainly appropriate to ask why a uniform treatment is not used for all spatial derivatives, but velocity is not a primary variable, so using PSE to evaluate its derivatives would require an unnecessary and expensive double summation. On the other hand, using the velocity derivative treatment for derivatives of primary variables—in other words, applying the derivative operator directly to the blob function—would be analogous to the method of Fishelov (1990) for incompressible flow, which lacks the conservation properties of PSE.

The continuity equation (2.14e) is satisfied by allowing the particles to change volume according to (2.7) and computing the particle mass density through

$$\rho_p(t) = \rho_p(0) V_p(0) / V_p(t). \tag{2.17}$$

Allowing the particles to expand and contract also ensures that the Jacobian of the flow map is correctly accounted for in the quadrature approximation of volume integrals.

The equations for three-dimensional flow differ from these only with regard to the vortex stretching term, $\boldsymbol{\omega} \cdot \nabla \mathbf{u}$, and consideration of the additional components of the vorticity vector. The velocity gradient tensor is already computed, so the treatment of vortex stretching poses no extra challenge. Incompressible three-dimensional vortex particle methods have been developed and applied extensively (see, e.g., Winckelmans and Leonard (1993)), and their extension to compressible flow should not require the development of any techniques beyond those presented

in the present work.

It is useful to reformulate the equations for the vorticity and dilatation in terms of the integral values of these quantities: the particle circulation, Γ_p, and source strength, Q_p. This approach, when combined with (2.7), eliminates the θ term from equation (2.14a) and an analogous term embedded in the double contraction term in equation (2.14b). The final set of equations for the particle strengths are written in particle-discretized form in Appendix A. By allowing the particles to follow the integral curves of the flow map, the substantial derivatives of the continuous equations are replaced by ordinary time derivatives for the particle strengths. These particle evolution equations may be solved simultaneously using a standard time integration scheme; we use the fourth-order Runge-Kutta method.

We also must specify initial conditions for the primary variables. Often it may be sufficient to set the initial dilatation and entropy to zero (unless the circumstances of a particular problem require otherwise), and then compute the initial enthalpy from the initial vorticity (or velocity, rather) through a solution of the following Poisson problem:

$$\nabla^2 h = -\nabla \mathbf{u}_s : (\nabla \mathbf{u}_s)^T. \tag{2.18}$$

This equation is solved using the same Green's function technique used to invert the Poisson problems (2.2) for the velocity potentials. This effectively reduces the magnitude of the transient that results from not specifying these initial conditions in an exactly consistent manner. With the initial enthalpy and entropy of a particle specified, the initial particle mass density can then be computed through the integral of Gibbs' equation, $dh = Tds + dp/\rho$, which when combined with the perfect gas equation of state leads to

$$\rho_p(0) = [(\gamma - 1)h_p(0)]^{1/(\gamma-1)} \exp\left(-\frac{\gamma}{\gamma - 1} s_p(0)\right). \tag{2.19}$$

Note that this relation is not valid for the particle strengths at later times; it relates the field quantities, which only initially coincide with the particle strengths. The

particles are initially located on a uniform Cartesian grid, with $V_p(0) = \Delta x^2$, where Δx is the inter-particle spacing.

2.3 Expansions of flow equations

When the flow Mach number is much less than unity and the extent of the flow region is much smaller than the wavelength of sound, we can construct asymptotic expansions of the equations of motion (2.14) with respect to the Mach number. This procedure, which follows that of Crow (1970), will illustrate the importance of the various terms in the equations, and in particular the balance between them. For simplicity, we will assume an inviscid, non-heat-conducting flow. The terms that we neglect are rarely important to the production of sound (Obermeier, 1984).

The procedure relies on the Helmholtz decomposition (2.1) and the observation that the vorticity dynamics to leading order do not depend on the acoustic field. Thus, the solenoidal part is regarded as a known forcing term as a function of the vorticity, $\mathbf{u}_s(\boldsymbol{\omega})$. The remaining irrotational portion of the velocity is left as the gradient of the potential, $\nabla\varphi$. The reduced set of equations that we wish to expand are

$$\frac{\partial\theta}{\partial t} + (\mathbf{u}_s + \nabla\varphi)\cdot\nabla\theta = -\nabla^2 h - \frac{\partial}{\partial x_j}\left(u_{s,i} + \frac{\partial\varphi}{\partial x_i}\right)\frac{\partial}{\partial x_i}\left(u_{s,j} + \frac{\partial\varphi}{\partial x_j}\right), \quad (2.20a)$$

$$\frac{\partial h'}{\partial t} + (\mathbf{u}_s + \nabla\varphi)\cdot\nabla h' = -\frac{1}{M^2}\theta - (\gamma-1)h'\theta, \quad (2.20b)$$

$$\nabla^2\varphi = \theta, \quad (2.20c)$$

where the variables have been scaled differently from the compressible scaling used in §2.2. Now, the variables are scaled as follows:

$$\begin{aligned} u_s &\sim U_0, & \varphi &\sim U_0 l, \\ h &\sim a_\infty^2, & h' &= h - h_\infty \sim U_0^2, \\ \theta &\sim U_0/l, & t &\sim l/U_0, \end{aligned}$$

where l is a typical eddy size, which may be different from the overall flow length-

scale, L.

Because of the difference in length scales between the nearfield flow and the far acoustic field, there is no uniformly-valid expansion. We can only construct separate expansions in each region and then attempt to match them in an intermediate region. In the present work we will only present the expansions, and refer the reader to Crow (1970) for a discussion of the matching process.

In the nearfield, the spatial variables are scaled by l: $\mathbf{x} \sim l$. The dependent variables are expanded in powers of M_0,

$$\begin{aligned}
\theta &= \Theta_0 + M_0\Theta_1 + M_0^2\Theta_2 + \cdots, \\
h' &= H'_0 + M_0 H'_1 + M_0^2 H'_2 + \cdots, \\
\varphi &= \Phi_0 + M_0\Phi_1 + M_0^2\Phi_2 + \cdots.
\end{aligned}$$

Note that $h = \frac{1}{\gamma-1} + M_0^2 h'$. We introduce these expansions into the equations (2.20) and match terms that are proportional to a common power of M_0. The resulting equations through M_0^2 are as follows:

$$O(1)\begin{cases} \nabla^2 H'_0 = -\dfrac{\partial^2 T_{ij}^{(0)}}{\partial x_i \partial x_j}, \\ T_{ij}^{(0)} = u_{s,i} u_{s,j}. \end{cases} \tag{2.21}$$

and

$$O(M_0^2)\begin{cases} \Theta_2 = -\dfrac{D_0 H'_0}{Dt}, \\ \nabla^2 \Phi_2 = \Theta_2, \\ \nabla^2 H'_2 = \dfrac{\partial^2 H'_0}{\partial t^2} - \dfrac{\partial^2 T_{ij}^{(2)}}{\partial x_i \partial x_j}, \\ T_{ij}^{(2)} = u_{s,i} u_{s,j} H'_0 + u_{s,i}\dfrac{\partial \Phi_2}{\partial x_j} + u_{s,j}\dfrac{\partial \Phi_2}{\partial x_i} + \dfrac{1}{2} H_0'^2 \delta_{ij}. \end{cases} \tag{2.22}$$

We have defined a hydrodynamic material derivative, $D_0/Dt \equiv \partial/\partial t + \mathbf{u}_s \cdot \nabla$. The $O(1)$ equation (2.21) governs the hydrodynamic enthalpy field that balances the acceleration of the fluid due to its rotational motion. It comprises the bulk of the

nearfield enthalpy. Note that this equation is clearly present on the right-hand side of the dilatation equation (2.14b). The balance of these two terms in (2.14b) is crucial to compute accurately for the sake of the dilatation and the stability of the method. Both the high-order-accurate treatment of derivatives and the smooth interpolation of remeshing that we develop in subsequent chapters are in large part motivated by this balance. Also note that (2.22) is precisely equation (2.18), which provides the initial enthalpy field.

The $O(M_0)$ terms all vanish. However, higher odd powers are present, but not considered. The $O(M_0^2)$ terms demonstrate that the nearfield dilatation is largely a reaction to the rate of change of the hydrodynamic enthalpy carried by a fluid element. The irrotational component of the velocity is thus proportional to M_0^2. The next term in the enthalpy represents the leading-order effect of compressibility to that quantity in the nearfield.

In the outer acoustic field, the relevant length scale is the wavelength of sound, λ. Thus, since $l/\lambda = M_0$, we define a new spatial variable, $\boldsymbol{\xi} = M_0\mathbf{x}$, and let $\nabla_\xi = \frac{1}{M_0}\nabla$. With the outer expansions

$$\begin{aligned}
\theta &= \theta_0 + M_0\theta_1 + M_0^2\theta_2 + \cdots, \\
h' &= h'_0 + M_0 h'_1 + M_0^2 h'_2 + \cdots, \\
\varphi &= \varphi_0 + M_0\varphi_1 + M_0^2\varphi_2 + \cdots,
\end{aligned}$$

we can construct the following equations that are valid in the farfield:

$$\left.\begin{aligned}
\frac{\partial^2 h'_n}{\partial t^2} - \nabla_\xi^2 h'_n &= 0, \\
\frac{\partial h'_n}{\partial t} + \nabla_\xi^2 \varphi_n &= 0.
\end{aligned}\right\} n = 2, 3, 4, 5$$

The lower-order coefficients ($n < 2$) are zero because it can be shown that there are no equivalent terms in the nearfield with which to match them (Crow, 1970). Thus, in the farfield, the enthalpy satisfies the linear homogeneous wave equation, as anticipated. It should be noted that the velocity potential coefficients, φ_n, do

not. Rather, it is the *sum* of φ and the scalar potential χ consistent with the solenoidal velocity u_s in the irrotational region, that obeys this equation.

Chapter 3

The generalized treatment of derivatives

In this chapter we propose a general approach to the treatment of spatial derivatives in particle methods. We are of course motivated by the need to approximate several such derivatives in the governing equations (2.14) of the DVPM, but the approach we present can also be applied to other particle methods. The challenge of a particle method is to accurately compute a spatial derivative from information only available at scattered locations.

Most approaches to this task are based on the same principle, that particles are collaborative entities with global rather than local, isolated behavior, so it is natural to use cumulative (i.e., integral) operators to approximate local (i.e., differential) operators. Some schemes connect the derivative treatment with the interpolation. In smoothed particle hydrodynamics (see, e.g., Monaghan (1985)), the pressure gradient is computed by simply applying the gradient operator directly to the interpolation kernel. For her viscous VPM, Fishelov (1990) used the same idea as in SPH, applying the differential operator directly to the blob function for computing the Laplacian of the vorticity. However, neither of these schemes is naturally conservative in global quantities (although with a slight modification the SPH formula is made to conserve linear and angular momentum).

Particle strength exchange, or PSE, was developed from a different approach. Degond and Mas-Gallic (1989) built from both the SPH treatment and from work by Cottet and Mas-Gallic (1990), but created a method that is more general and

that possesses natural conservation properties. The treatment developed in this chapter is based on the ideas presented by Degond and Mas-Gallic (1989). We will generalize this methodology to treat arbitrary derivatives in various contexts, such as wave propagation, and then present an analysis of their behavior in these contexts. This development will lead to the construction of higher-order-accurate kernels that prove crucial to the success of the DVPM.

We introduce some notation first. For differential operators we use the notation

$$D^\beta = \frac{\partial^{|\beta|}}{\partial x_1^{\beta_1} \partial x_2^{\beta_2} \cdots \partial x_d^{\beta_d}},$$

where $\beta = (\beta_1, \beta_2, \ldots, \beta_d)$ is a multi-index, $|\beta| \equiv \beta_1 + \beta_2 + \cdots + \beta_d$, and d is the physical dimension. Also, $\mathbf{y}^\beta = y_1^{\beta_1} y_2^{\beta_2} \cdots y_d^{\beta_d}$. A sum

$$\sum_{|\beta|=1}^{\infty}$$

denotes a double sum: an inner sum over all multi-indices β with sum equal to $|\beta|$, and an outer sum over all values of $|\beta| \geq 1$.

3.1 Particle strength exchange

The general integral PSE operator for approximating the action of D^β on f has the form

$$L^\beta f(\mathbf{x}) \equiv \frac{1}{\varepsilon^{|\beta|}} \int (f(\mathbf{y}) \mp f(\mathbf{x})) \eta_\varepsilon^\beta (\mathbf{x} - \mathbf{y})\, d\mathbf{y}, \tag{3.1}$$

where η^β is the kernel and $\eta_\varepsilon(\mathbf{x}) = \eta(\mathbf{x}/\varepsilon)/\varepsilon^d$, where ε is the kernel radius. For conservation reasons to be discussed shortly, the sign chosen for the term in parentheses depends on whether $|\beta|$ is even or odd. If even, then the negative sign is chosen, and if odd, the positive sign is used. The integral is discretized by midpoint quadrature over the particles, using the particle locations and volumes as

the control points and weights, e.g.,

$$\int g(\mathbf{y})\, d\mathbf{y} \approx \sum_q V_q(t) g(\mathbf{x}_q(t)).$$

Applying this rule produces an approximation of $L^\beta f(\mathbf{x})$, defined as

$$\hat{L}^\beta f(\mathbf{x}) \equiv \frac{1}{\varepsilon^{|\beta|}} \sum_q V_q(t) \left(f(\mathbf{x}_q) \mp f(\mathbf{x})\right) \eta_\varepsilon^\beta(\mathbf{x} - \mathbf{x}_q(t)). \tag{3.2}$$

In the particle-discretized equations in which PSE is applied, a discrete PSE operator is used, defined as

$$L_h^\beta(t) f_p \equiv \frac{1}{\varepsilon^{|\beta|}} \sum_q V_q(t)(f_q(t) \mp f_p(t)) \eta_\varepsilon^\beta(\mathbf{x}_p(t) - \mathbf{x}_q(t)). \tag{3.3}$$

Effectively, this definition can be regarded as an approximation of (3.2), in which the field value at each particle location has been replaced by the particle strength, $f(\mathbf{x}_p) \approx f_p$. This replacement cannot be made in general (recall that the field quantity is interpolated by several nearby blobs). However, it can be shown (Degond and Mas-Gallic, 1989, Theorem 2) that in applying (3.3) to the convection-diffusion equation, the error between the exact solution and the solution of the particle-discretized equation is bounded. The proof of boundedness when (3.3) is applied to equations (2.14) should follow by similar arguments.

The rationale for the "strength exchange" label becomes clear if we consider the application to specific equations. From hereon, the time dependence of the quantities will not be explicitly written except to avoid ambiguity. Applying (3.3) to the Laplacian operator in the convection-diffusion equation, the particle strengths evolve according to

$$\frac{dF_p}{dt} = \frac{1}{\varepsilon^2} \sum_q (V_p F_q - V_q F_p) \eta_\varepsilon^{\text{lap}}(\mathbf{x}_p - \mathbf{x}_q), \tag{3.4}$$

where $F_p \equiv V_p f_p$ and the superscript of η denotes its use for the Laplacian. For reasons explained in the next section, the kernel for this operator is constructed

to be even in both coordinate directions. Thus, the right-hand side has a skew-symmetry such that when the equation is integrated, the portion of strength lost by particle p in its interaction with q will be exactly equal to the portion gained by q. If both sides of (3.4) are summed over all the particles, the right-hand side cancels identically and thus the total strength is conserved. If the equation considered had instead a first derivative, then the kernel would be odd in its argument, and conservation would be guaranteed if the strengths in the summand were added.

3.2 Methodology

The derivation of formula (3.1) is not restricted to the Laplacian operator. In fact, *any* differential operator can be given an integral approximation of *any* order of accuracy, provided the kernel obeys the appropriate set of moment conditions.

3.2.1 Full-space integral approximations

Consider a Taylor expansion of the function, f, about a point, $\mathbf{x}$, and evaluate the expansion at another point, $\mathbf{y}$:

$$f(\mathbf{y}) = f(\mathbf{x}) + \sum_{|\alpha|=1}^{\infty} \frac{1}{|\alpha|!}(\mathbf{y}-\mathbf{x})^{\alpha} D^{\alpha} f(\mathbf{x}).$$

We desire the approximation of the operator D^{β}, which is included in the sum on the right-hand side. Now $f(\mathbf{x})$ is subtracted from both sides and each term is convolved with the unknown kernel η^{β} scaled by ε. The result is

$$\varepsilon^{|\beta|} L^{\beta} f(\mathbf{x}) = \sum_{|\alpha|=1}^{\infty} \frac{1}{|\alpha|!} D^{\alpha} f(\mathbf{x}) \int (\mathbf{y}-\mathbf{x})^{\alpha} \eta_{\varepsilon}^{\beta}(\mathbf{x}-\mathbf{y})\, d\mathbf{y},$$

where the operator L^{β} is defined in equation (3.1), with the negative sign chosen. The variables of integration are translated and rescaled to simplify the integrals

to

$$L^\beta f(\mathbf{x}) = \sum_{|\alpha|=1}^{\infty} \frac{(-\varepsilon)^{|\alpha|-|\beta|}}{|\alpha|!} D^\alpha f(\mathbf{x}) M_\alpha, \tag{3.5}$$

where for notational simplicity, the α-moment has been defined as

$$M_\alpha = \int \mathbf{y}^\alpha \eta(\mathbf{y})\, d\mathbf{y}. \tag{3.6}$$

Now the derivative that will be approximated is isolated on the left-hand side. A linear combination of derivatives can also be approximated, of course, but only one is considered here:

$$D^\beta f(\mathbf{x}) = \frac{(-1)^{|\beta|}|\beta|!}{M_\beta} L^\varepsilon f(\mathbf{x}) - \sum_{\substack{|\alpha|=1 \\ |\alpha|\neq|\beta|}}^{\infty} \frac{(-\varepsilon)^{|\alpha|-|\beta|}}{(|\alpha|-|\beta|)!} D^\alpha f(\mathbf{x}) \frac{M_\alpha}{M_\beta} - \sum_{\substack{|\alpha|=|\beta| \\ \alpha\neq\beta}} D^\alpha f(\mathbf{x}) \frac{M_\alpha}{M_\beta}.$$

To construct a useful approximation, the moments that appear inside the summations on the right-hand side must vanish to some degree, and the β-moment in the denominator must be nonzero. Thus, the following set of moment conditions is imposed for an approximation of order r:

$$M_\alpha = \begin{cases} (-1)^{|\beta|}|\beta|!, & \alpha = \beta, \\ 0, & |\alpha| = |\beta|,\ \alpha \neq \beta, \\ 0, & |\alpha| \in [1, |\beta|-1] \cup [|\beta|+1, |\beta|+r-1], \end{cases} \tag{3.7a}$$

as well as

$$\int |\mathbf{y}|^{|\beta|+r} |\eta^\beta(\mathbf{y})|\, d\mathbf{y} < \infty. \tag{3.7b}$$

Provided these conditions are satisfied, the L_2 error in approximating the differential operator by (3.1) is bounded by (Degond and Mas-Gallic, 1989):

$$||D^\beta f - L^\beta f||_{0,2} \leq C_1 \varepsilon^r ||f||_{r+|\beta|,2}, \tag{3.8}$$

where C_1 is some constant and $||\cdot||_{k,m}$ is the norm of the $W^{k,m}(\mathbb{R}^d)$ Sobolev space. The quadrature approximation of the integral operator incurs additional error, which is bounded by

$$||L^\beta f - \hat{L}^\beta f||_{0,2} \leq C_2 \frac{\Delta x^m}{\varepsilon^{m+|\beta|-1}} ||f||_{m,2}, \tag{3.9}$$

provided that $\eta \in W^{m,1}(\mathbb{R}^d)$ and $f \in W^{m,2}(\mathbb{R}^d)$, and that the flow map is smooth as well. Thus, the error bound accounts for distortion in the particle grid, but it should be noted that the proportionality constant, C_2, is dependent upon the duration of the simulation and the velocity field to which the particles are subjected to. In practice it is found that the particles must occasionally be reinitialized to control their dispersion, which ultimately degrades the quadrature. This is explored in §3.4.4.

Gaussian kernels such as those considered below belong to $W^{\infty,1}(\mathbb{R}^d)$, which appears to make the quadrature spectrally accurate, provided that $\varepsilon > \Delta x$. In fact, the proof of the error estimate also assumes that the function f is either periodic, or that the function and its derivatives vanish on the boundary of the domain. It is well known that midpoint quadrature leads to superb accuracy under these conditions, but if these do not hold, then the estimate reverts to second-order. However, reducing the error in (3.8) through an increase of the order of accuracy, r, is still very effective at mitigating the overall error, as the examples in §3.4 will show. Furthermore, high-order-accurate kernels are essential for computing the delicate balance of terms in (2.14b), as explained in §2.3.

The construction of the kernel is simplified considerably if we assume some symmetry in its form. For instance, if the derivative we wish to approximate is even in the x_l-direction (i.e., β_l is even), then we will construct $\eta^\beta(\mathbf{x})$ to be even with respect to this direction, and consequently all moments in (3.7a) for which α_l is odd automatically vanish. Similarly, if β_l is odd, then $\eta^\beta(\mathbf{x})$ should be odd

in this direction. With this symmetry,

$$\eta^\beta(-\mathbf{x}) = (-1)^{|\beta|}\eta^\beta(\mathbf{x}). \tag{3.10}$$

With this form of kernel, the PSE operator (3.1) can take either sign in the integrand. The operator resulting from the Taylor expansion above can be expressed as

$$L^\beta f = \frac{1}{\varepsilon^{|\beta|}}(\eta_\varepsilon^\beta \star f - M_0 f),$$

where $\star$ denotes convolution. The second term is zero if $|\beta|$ is odd because the 0-moment vanishes. Thus, the subtraction may be replaced by addition without affecting the approximation. However, the discretized operator (3.3) retains both terms because of the conservation that it allows. The choice of sign is made because of (3.10).

Some examples will serve to illustrate the procedure of constructing a kernel. Consider the original intent of the formula, to approximate the Laplacian operator. A kernel of order $r = 2$ will be constructed for two-dimensional applications. In this case, the differential operator is $\nabla^2 = D^{(2,0)} + D^{(0,2)}$, and the moment conditions are

$$\begin{aligned} &M_{(1,0)} = 0, \qquad M_{(0,1)} = 0, \\ &M_{(2,0)} = 2, \qquad M_{(1,1)} = 0, \qquad M_{(0,2)} = 2. \end{aligned}$$

At first sight, it looks as though the kernel would need 5 degrees of freedom to satisfy the entire set of 5 conditions. However, if the form of the kernel is chosen carefully, then many of these conditions are redundant. For instance, choose the template

$$\eta(\mathbf{x}) = \frac{1}{\pi}\left(\sum_{j=0}^{m} \gamma_j |\mathbf{x}|^{2j}\right) e^{-|\mathbf{x}|^2}. \tag{3.11}$$

The kernel possesses the symmetric form discussed above, so all of the moments with at least one odd index vanish immediately without consideration of the coefficients, γ_j. Also, it can be shown that all of the remaining conditions for a given value of $|\alpha|$ (i.e., on a given row in the above array) are satisfied if one of the conditions is satisfied (including the $M_{(2,0)}$ and $M_{(0,2)}$ conditions, due to the symmetry of the kernel). Thus, only *one* coefficient is needed to satisfy 5 conditions. The reason for this reduction is that the conditions were expressed in Cartesian coordinates, whereas a cylindrical system would be more appropriate for this particular operator. In fact, for a kernel of order r, we would need only $r/2$ coefficients (i.e., $m = r/2 - 1$). Upon substituting the template (3.11) into (3.6) and then expressing the integral in the more natural cylindrical system, each moment becomes a linear combination of the coefficients, γ_j:

$$M_\alpha = \frac{1}{\pi}\Gamma\left(\frac{\alpha_1+1}{2}\right)\Gamma\left(\frac{\alpha_2+1}{2}\right)\sum_{j=0}^{r/2-1}\gamma_j\frac{\Gamma\left(\frac{2j+|\alpha|+2}{2}\right)}{\Gamma\left(\frac{|\alpha|+2}{2}\right)}, \tag{3.12}$$

where Γ is the gamma function. Continuing with the $r = 2$ example, an algebraic equation is formed for the coefficient:

$$\frac{1}{\pi}\Gamma(3/2)\Gamma(1/2)\gamma_0 = 2,$$

and the resulting kernel is $\eta^{\text{lap}}(\mathbf{x}) = \frac{4}{\pi}e^{-|\mathbf{x}|^2}$.

Now we derive a 4th-order-accurate kernel for application to first derivatives in two-dimensional problems. Derivatives in the x_1-direction are considered, but adaptation to the other direction is straightforward. The moments conditions are

$$\begin{aligned}
&M_{(1,0)} = -1, \quad && M_{(0,1)} = 0, && && \\
&M_{(2,0)} = 0, && M_{(1,1)} = 0, && M_{(0,2)} = 0, && \\
&M_{(3,0)} = 0, && M_{(2,1)} = 0, && M_{(1,2)} = 0, && M_{(0,3)} = 0, \\
&M_{(4,0)} = 0 && M_{(3,1)} = 0, && M_{(2,2)} = 0, && M_{(1,3)} = 0, \quad && M_{(0,4)} = 0.
\end{aligned}$$

Again, many of these conditions are redundant if we choose our kernel template

wisely. We use

$$\eta(\mathbf{x}) = \frac{x_1}{\pi}\left(\sum_{j=0}^{m}\gamma_j|\mathbf{x}|^{2j}\right)e^{-|\mathbf{x}|^2}, \tag{3.13}$$

for which all of the moments with at least one even index vanish, and in fact $m = r/2 - 1$ once again. The moments are then

$$M_\alpha = \frac{1}{\pi}\Gamma\left(\frac{\alpha_1+2}{2}\right)\Gamma\left(\frac{\alpha_2+1}{2}\right)\sum_{j=0}^{r/2-1}\gamma_j\frac{\Gamma\left(\frac{2j+|\alpha|+3}{2}\right)}{\Gamma\left(\frac{|\alpha|+3}{2}\right)}. \tag{3.14}$$

For the present example, only two coefficients are needed to satisfy 14 conditions. The set of algebraic equations for the two coefficients is

$$\begin{bmatrix} \Gamma(2) & \Gamma(3) \\ \Gamma(3) & \Gamma(4) \end{bmatrix}\begin{pmatrix} \gamma_0 \\ \gamma_1 \end{pmatrix} = \begin{pmatrix} -2\Gamma(2) \\ 0 \end{pmatrix}.$$

The resulting kernel is $\eta^{(1,0)}(\mathbf{x}) = \frac{x_1}{\pi}(-6+2|\mathbf{x}|^2)e^{-|\mathbf{x}|^2}$; for derivatives in the other direction, the factor x_1 need only be replaced by x_2. Appendix B contains a list of kernels of several orders of accuracy for many applications in both one and two space dimensions.

3.2.2 One-sided integral approximations

In some circumstances, it is useful to have integral approximations that are "one-sided." In other words, the integration proceeds only over a half-space, with the particle defining the local origin. In this way, a particle only interacts with particles in this half-space, and more precisely, only with particles in the intersection of this half-space with the kernel support. This is particularly useful near boundaries, where particles only have a partial set of neighbors, and we will use this type of operator for enforcing the radiation boundary condition in §4.3.

A "left-sided" integral operator L_L^β is defined as

$$L_L^\beta f(\mathbf{x}) \equiv \frac{1}{\varepsilon^{|\beta|}} \int_{\Omega^L} (f(\mathbf{y}) - f(\mathbf{x}))\, \eta_\varepsilon^{L,\beta}(\mathbf{x}-\mathbf{y})\, d\mathbf{y}, \tag{3.15}$$

where the integration is over the half-space defined as $\Omega^L = \{(y_1, y_2, \ldots, y_d) \in \mathbb{R}^d \,|\, y_1 \le x_1\}$ (i.e., the left-half space). Similarly, a "right-sided" operator is integrated over $\Omega^R = \{(y_1, y_2, \ldots, y_d) \in \mathbb{R}^d \,|\, y_1 \ge x_1\}$. Note that there is no choice to make about the sign in the integrand as there was in the full-space case, because these operators lack the symmetry to conserve strength. The discrete form of the left-sided operator is

$$L_{L,h}^\beta f_p \equiv \frac{1}{\varepsilon^{|\beta|}} \sum_{\substack{q \\ \mathbf{x}_q \in \Omega^L}} V_q\, (f_q - f_p)\, \eta_\varepsilon^{L,\beta}(\mathbf{x}_p - \mathbf{x}_q). \tag{3.16}$$

This special treatment does not change the derivation of the last section significantly. We define a right-sided moment of the kernel as

$$M_\alpha^R = \int_{-\infty}^{\infty} \int_{-\infty}^{\infty} \cdots \int_{0}^{\infty} \mathbf{y}^\alpha \eta^L(\mathbf{y})\, dy_1\, dy_2 \cdots dy_d, \tag{3.17}$$

subject to the same conditions (3.7a)–(3.7b) as before. A right-sided moment appears in the derivation of the left-sided operator because when the integrals are expressed in the local particle-centered coordinate system, convolution uses a reflected form of the kernel and thus swaps the limits of integration. However, it should be noted that, if the same symmetry form is assumed for one-sided kernels as for full-space ones, then the right-sided and left-sided moments are related very simply: $M_\alpha^R = (-1)^{|\alpha|-|\beta|} M_\alpha^L$. In particular, $M_\beta^R = M_\beta^L$, and since all other moments are constrained to be zero, *kernels derived for left-sided PSE operators can also be used in right-sided operators, and vice versa.*

We derive here a 2nd-order left-sided kernel for approximating $\frac{\partial}{\partial x_1}$ in two dimensions. The same kernel template (3.13) will be used, although the kernel's oddness in the x_1 direction cannot be exploited as in the full-space case because

of the new limits of integration in (3.17). The set of moment conditions is

$$\begin{aligned} M^R_{(1,0)} &= -1, \qquad M^R_{(0,1)} = 0, \\ M^R_{(2,0)} &= 0, \qquad M^R_{(1,1)} = 0, \qquad M^R_{(0,2)} = 0, \end{aligned} \tag{3.18}$$

and because the kernel is even in the x_2 direction, the moments with odd second index are identically zero. Also, for the same reasons as in the full-space case, the rows on which all moments are constrained to be zero collapse to one condition. We thus need only two coefficients to satisfy the five conditions. The moments have analytical expression (c.f. equation (3.14))

$$M^R_\alpha = \frac{1}{2\pi}\Gamma\left(\frac{\alpha_1+2}{2}\right)\Gamma\left(\frac{\alpha_2+1}{2}\right)\sum_{j=0}^{m}\gamma_j\frac{\Gamma\left(\frac{2j+|\alpha|+3}{2}\right)}{\Gamma\left(\frac{|\alpha|+3}{2}\right)}, \tag{3.19}$$

which are assigned the appropriate values to form two equations for the coefficients. Proceeding in this way we find that the 2nd-order left-sided kernel is $\eta^{L,(1,0)}(\mathbf{x}) = \frac{x_1}{\pi}(-20+8|\mathbf{x}|^2)e^{-|\mathbf{x}|^2}$. Again, the same kernel can be used in a right-sided PSE operator, as well as for one-sided derivatives in the x_2-direction by replacing the x_1 factor.

3.2.3 Stability

The stability of the quadrature (3.3) relies on the condition that the ratio of kernel radius to inter-particle spacing, $\kappa = \varepsilon/\Delta x$, be greater than unity (i.e., the particles must overlap with their neighbors). As time progresses the flow will distort the particle grid, and locally this overlap restriction may fail. Without overlap, the particles cannot communicate and thus strength exchange breaks down. As we will discuss in §4.2, it is important to reinitialize the particles occasionally. Some examples in §3.4 will clarify the importance of this remeshing.

The time discretization of an equation in which PSE is used carries further stability restrictions. The proof of Degond and Mas-Gallic (1989) for PSE applied to a convection-diffusion equation relies on the assumption that the kernels are non-

negative, so stability cannot be guaranteed for kernels that violate this assumption (although positivity is only a sufficient condition). It should be noted that kernels derived from the template (3.11) will often have negative portions—most of the kernels listed in Appendix B do. Without proof, we posit that an upper limit on the time-step size of the problem is necessary for stability, as in conventional finite-difference schemes, except that the kernel radius, ε, is the relevant length scale rather than the inter-particle spacing. For instance, in a diffusion problem with diffusivity ν, it is required that $\Delta t < C_d \varepsilon^2 / \nu$, where C_d is some constant near unity, and in a convection problem, the "CFL" number is restricted, $\Delta t < C_c \varepsilon / c_0$, where c_0 is a typical wave speed. The constants will obviously depend on the time integration scheme used.

3.3 Fourier analysis of the error

The original intent of the PSE method was for application to convection-diffusion equations. When applied in such a parabolic context, the approximation modifies the original differential equation by adding diffusive error terms. The strength of this diffusion is related to the order of accuracy of the kernel. The application of PSE in this paper is extended to many different settings, including those involving wave propagation. In this setting, the role of the extra terms in the modified equation is *dispersive* rather than *diffusive*. As a demonstration of this effect, consider the one-dimensional linear wave equation:

$$\frac{\partial^2 f}{\partial t^2} - \frac{\partial^2 f}{\partial x^2} = 0.$$

This equation is satisfied by a travelling wave, $e^{i(kx-\omega t)}$, for which the frequency is related to the wavenumber by $\omega(k) = \pm k$, indicating that it travels either to the left or the right at unit speed, regardless of the wavenumber. If the spatial derivative is approximated by a full-space PSE integral, the dependence of the frequency on the wavenumber for solutions of the modified equation is changed. The local slope of this dispersion relation for some wavenumber k is the group

velocity of energy associated with k. Thus, a packet of waves with wavenumbers centered at k will propagate at this speed, and if this speed varies with k, then waves of larger bandwidth will be dispersed.

We explore this PSE-modified dispersion relation here:

$$\frac{\partial^2 f}{\partial t^2} - \frac{1}{\varepsilon^2}\int_{-\infty}^{\infty} (f(y) - f(x))\, \eta_\varepsilon^{(2)}(x-y)\, dy = 0.$$

Substitute the representative waveform $f(x,t) = e^{i(kx-\omega t)}$ and simplify to get

$$\omega^2 = \frac{1}{\varepsilon^2}\left(M_0 - \hat{\eta}^{(2)}(\varepsilon k)\right),$$

where $\hat{\eta}$ denotes the Fourier transform of the kernel and M_0 is the 0-moment. Thus, for the travelling wave to be a solution of the modified equation,

$$\omega(k) = \pm\frac{1}{\varepsilon}\sqrt{M_0 - \hat{\eta}^{(2)}(\varepsilon k)}.$$

With respect to the exact relation, the right-hand side can be regarded as a modified wavenumber, $k_{mod}(k)$:

$$k_{mod}(k) = \frac{1}{\varepsilon}\sqrt{M_0 - \hat{\eta}^{(2)}(\varepsilon k)}. \tag{3.20}$$

Expanding $\hat{\eta}^{(2)}(\varepsilon k)$ in a Taylor series about $\varepsilon k = 0$, and assuming that the rth-order-accurate kernel is symmetric with respect to x, the modified wave number can be written as

$$\begin{aligned} k_{mod}(k) &= k\left[1 + \sum_{n=r/2+1}^{\infty} \frac{(\varepsilon k)^{2(n-1)}(-1)^{n-1}}{(2n)!} M_{2n}\right]^{1/2} \\ &\approx k\left[1 + \frac{1}{2}\frac{(\varepsilon k)^r(-1)^{r/2}}{(r+2)!} M_{r+2}\right]. \end{aligned} \tag{3.21}$$

Thus, the wavenumber is modified by the second term in brackets. This term is dependent upon k, so the speed of a travelling wave will depend upon k as well

and thus the PSE approximation is dispersive. However, increasing the order of accuracy of η clearly reduces the strength of this dispersion, as the leading-order modification of the wave number is proportional to ε^r. It is also important to note that the relationship is purely real, due to the symmetry of the kernels used, and thus PSE is nondissipative.

We have so far only considered the dispersive effects of the integral PSE approximation, but in practice we use a discretized form of this. The discrete analog of (3.20) is

$$k_{mod}(k) = \frac{1}{\varepsilon}\sqrt{\widetilde{M_0} - \tilde{\eta}^{(2)}(k)}, \tag{3.22}$$

where $\widetilde{M_0}$ is the discrete 0-moment,

$$\widetilde{M_0} = \frac{\Delta x}{\varepsilon} \sum_{p=-\infty}^{\infty} \eta^{(2)}(p\Delta x/\varepsilon),$$

and $\tilde{\eta}^{(2)}$ is the discrete Fourier transform of the kernel,

$$\tilde{\eta}(k) = \frac{\Delta x}{\varepsilon} \sum_{p=-\infty}^{\infty} e^{ikp\Delta x} \eta^{(2)}(p\Delta x/\varepsilon).$$

We have assumed here a grid of infinite extent with spacing Δx, which is a reasonable approximation to an actual grid of finite length, provided that in the latter we consider the solution away from the ends of the grid.

Figure 3.1(a) depicts the modified wavenumber—computed numerically—for the discrete PSE operator using kernels of various orders of accuracy. By the Nyquist sampling theorem, the maximum wavenumber we can resolve on this grid is $\pi/\Delta x$. When the data of nearby particles varies on a spatial scale that approaches the inter-particle spacing, the wavenumber content of the data extends to $\pi/\Delta x$. For the 2nd-order-accurate kernel, the group velocity, dk_{mod}/dk, strays from unity even for small wavenumbers. However, increasing the order of accuracy of the PSE kernel has a considerable effect on its approximating ability. The 8th-order-accurate PSE scheme is much less dispersive.

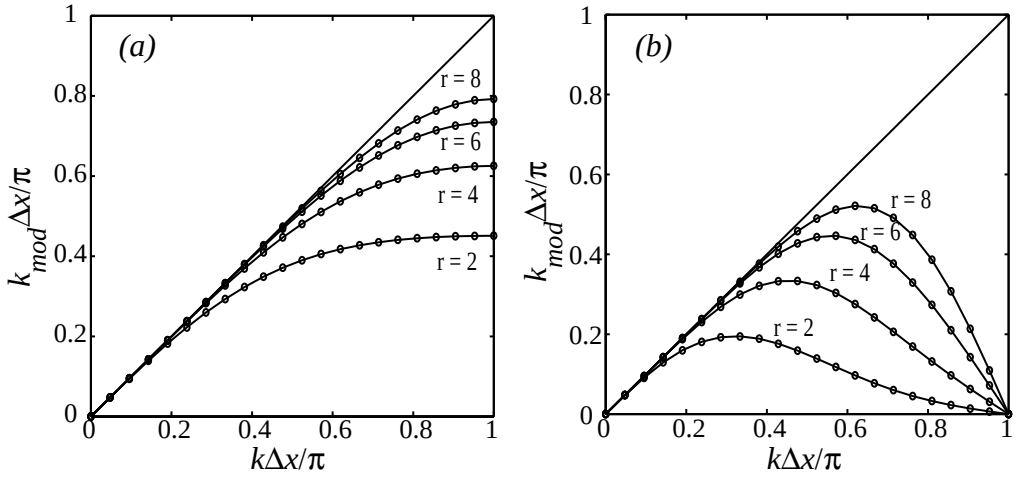

Figure 3.1: Modified wavenumber in applying PSE to (a) wave equation, and (b) first-order convection equation, with 2nd, 4th, 6th and 8th order kernels, $\kappa = 1.4$. Exact: '———'; Discrete PSE: '—○—'.

A similar analysis can be performed for the first-derivative PSE operator in the context of the one-dimensional convection equation,

$$\frac{\partial f}{\partial t} + \frac{\partial f}{\partial x} = 0.$$

Assuming the same form of solution as before, the frequency and wavenumber are found to be related by $\omega(k) = k$, so waves of any wavenumber travel with unit speed in the positive x direction. The modified wavenumber using the discrete PSE operator for the first derivative can be shown to be

$$k_{mod}(k) = -\frac{i}{\varepsilon}\tilde{\eta}^{(1)}(k) \tag{3.23}$$

This relation is plotted in Figure 3.1(b) for $r = 2$, 4, 6 and 8. The same poor behavior of the low-order-accurate PSE operators is apparent, as is the significant improvement using higher-order-accurate kernels.

Figure 3.2(a) demonstrates the importance of minimizing dispersion. A packet

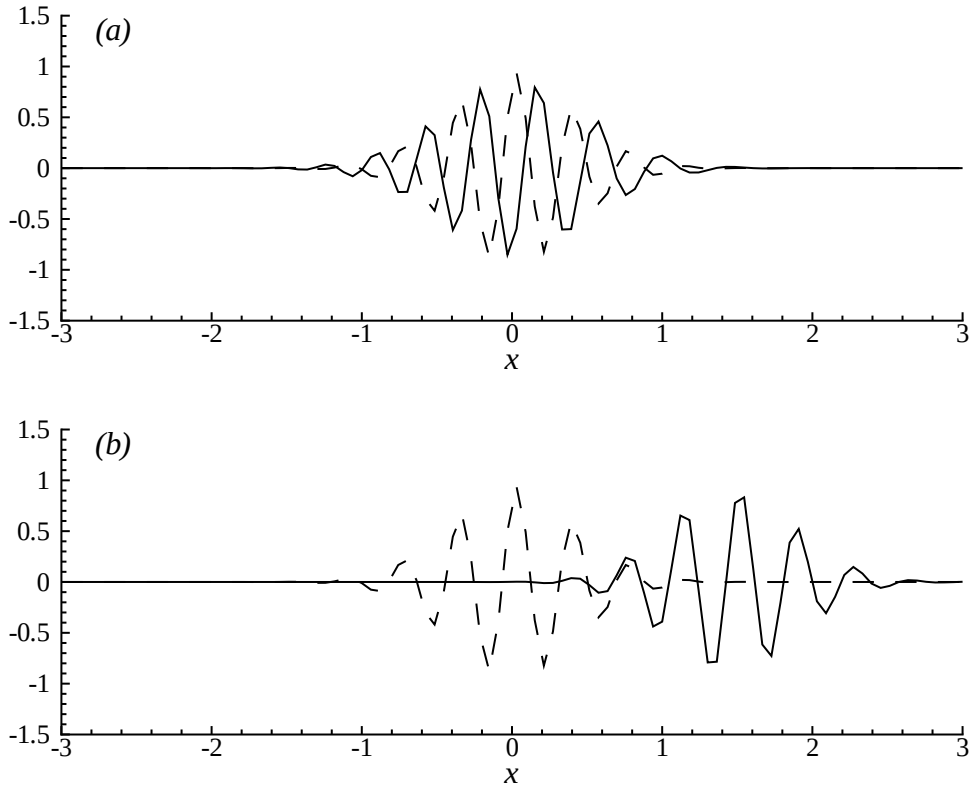

Figure 3.2: Packet of waves centered at $k_0 = 0.32\pi/h$, convected with (a) 2nd-order, and (b) 8th-order PSE, at $t = 0$: '– – –' and $t = 1.5$: '———'.

of waves of the form

$$f(x) = \frac{1}{\sqrt{\pi\sigma^2}} e^{-(x-x_0)^2/\sigma^2} \cos(k_0 x),$$

with radius $\sigma = 0.1$, is used as an initial condition for the convection equation, to which a 2nd-order PSE approximation is applied. The packet is Gaussian-distributed about the wavenumber k_0, which we set to $0.32\pi/\Delta x$. According to Figure 3.1(b), the PSE-modified group velocity at this value is approximately zero. As expected, the pulse has not moved after 1.5 units of time. In contrast, the same packet simulated using an 8th-order PSE approximation moves the correct distance, as Figure 3.2(b) shows.

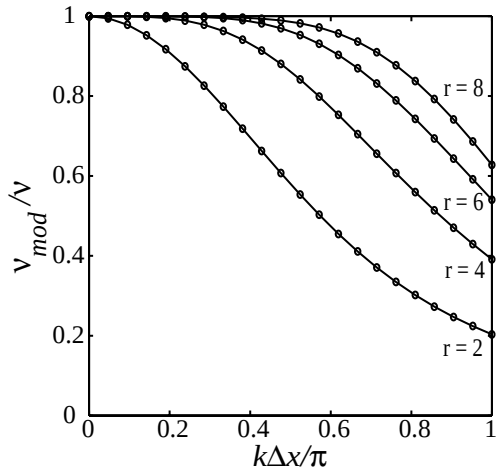

Figure 3.3: Modified viscosity in applying PSE to diffusion equation with 2nd, 4th, 6th and 8th order kernels, $\kappa = 1.4$.

The use of the modified relationship between frequency and wavenumber to assess the error of PSE need not be limited to hyperbolic problems. The analysis is equally important in a diffusive context, revealing the extent to which numerical viscosity affects the components. Consider the one-dimensional diffusion equation,

$$\frac{\partial f}{\partial t} = \nu \frac{\partial^2 f}{\partial x^2}.$$

The exact relationship between frequency and wavenumber is $\omega(k) = -i\nu k^2$. Applying PSE to the spatial derivative results in the same modified wavenumber as for the wave equation (3.20). Alternatively, the modification can be viewed as affecting the viscosity. Expressing this new viscosity in terms of the kernel's integral moments, we have

$$\nu_{mod} = \nu \left[1 - \sum_{n=r/2+1}^{\infty} \frac{(\varepsilon k)^{2(n-1)}(-1)^{n-1}}{(2n)!} M_{2n} \right].$$

The discrete counterpart of this modified viscosity is plotted in Figure 3.3 for the usual set of kernels. It is clear that high wavenumber components are under-

diffused, but that high-order-accurate kernels mitigate this discrepancy. A 2nd-order-accurate kernel leads to too little diffusion for even well-resolved data, but 8th-order-accurate PSE performs much better.

It should be added that such a modification of the viscosity can actually be exploited. For inviscid simulations, Cottet (1996) has shown that the numerical viscosity resulting from the mollifying of the velocity kernel in vortex methods—the mollifying leads to an error similar to that of PSE—can be tailored to derive an eddy viscosity model, which is essential to capture the self-organizing of vorticity into large-scale structures from an initially chaotic field. Monaghan and Gingold (1983) have used numerical viscosity to reduce the oscillations near shocks in SPH.

3.4 Examples

Model problems are described in this section in order to demonstrate fundamental characteristics of PSE that also arise when it is applied to more complex problems.

3.4.1 Rates of convergence and efficiency

The purpose of the set of tests described here is twofold: to demonstrate that the high-order-accurate PSE kernels derived in this work do indeed lead to convergence at their designed rate, and to show that increasing the order of accuracy of a kernel leads to more efficient computation. The second derivative of the function,

$$f(x) = \frac{1}{\sqrt{\pi\sigma^2}} e^{-x^2/\sigma^2},$$

is used as the model for evaluation, with $\sigma = 0.05$. The derivative is approximated on a uniform grid of points on the domain $[-1/2, 1/2]$. The ratio of kernel radius to inter-particle spacing, κ, is set at either 1.5 or 2. The discrete L_2 error between the exact derivative and its PSE approximation is computed for a variety of grid resolutions; kernels of 2nd, 4th, 6th and 8th order of accuracy are used. The results for $\kappa = 2$ are shown in Figure 3.4. The error, ϵ, converges as expected for all four kernels: $\epsilon \propto \Delta x^r$, or equivalently, $\epsilon \propto \varepsilon^r$. Moreover, as the order of accuracy of the

kernel increases, the error converges uniformly with respect to the inter-particle spacing.

A question we may ask is: What is the minimum number of grid points needed to achieve some specified tolerance of error? The computational effort appears to be proportional to the square of the number of grid points, N^2, but with appropriate truncation of point-to-point interactions it can be made proportional to N. Thus, the minimum number of points required to reach a specific level of error is directly related to the *efficiency* of the kernel, a very useful metric. This information is readily available from Figure 3.4 by choosing a level on the vertical axis and reading across to where the level intersects each kernel's convergence curve, then inverting the corresponding grid spacing to get N. For the level $\epsilon = 10^{-4}$, the results for each kernel are tabulated in Table 3.1. Also displayed is the CPU time required to compute this derivative, on a SGI Octane with an R10000 processor. The 2nd-order-accurate kernel requires a very large number of points to achieve the tolerance, while the 4th-order-accurate kernel needs only about 1/10 of this number, and the 6th- and 8th-order-accurate kernels require successively fewer.

The data can be reduced to the following approximate relation:

$$\epsilon \approx 0.9(18\varepsilon)^r.$$

The appearance of a constant factor inside the parentheses may seem surprising. However, the error bound (3.8) contains the Sobolev norm of f, and it can be shown that this particular norm of the Gaussian is proportional to $1/\sigma^r$, so the error is bounded by $\epsilon \leq C'(\varepsilon/\sigma)^r$, where C' is another constant. In our tests $1/\sigma = 1/0.05 = 20$, so the results are consistent with the expected bound. This form of the error bound explains why the successive improvement in efficiency of each kernel over the previous one becomes less striking as r increases in Table 3.1. The minimum number of grid points required to reach a fixed level of error is proportional to $(C'')^{1/r}$, where C'' is constant. Thus, past a certain point, increasing the order of accuracy of the kernel does not markedly improve the

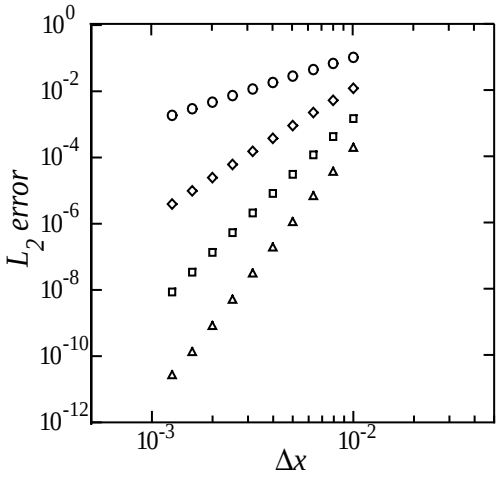

Figure 3.4: Error in computing second derivative for several grid resolutions and kernels of varying order of accuracy. Order 2: '$\circ$'; Order 4: '$\diamond$'; Order 6: '$\square$'; Order 8: '$\triangle$'.

Order r	minimum N	CPU time (sec.)
2	3440	4.28
4	354	0.0478
6	165	0.0114
8	111	0.00705

Table 3.1: Minimum number of particles required to achieve error of 10^{-4} and the corresponding CPU time.

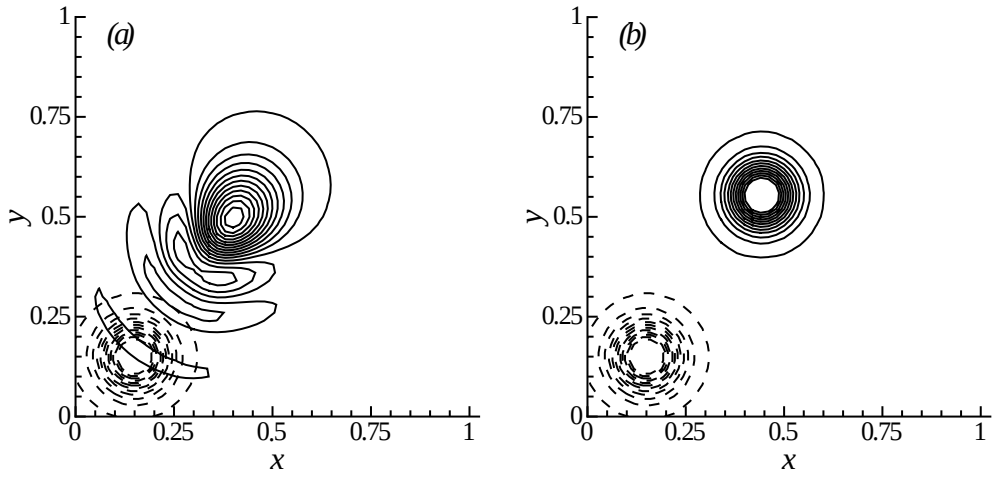

Figure 3.5: Gaussian pulse convecting in direction $\hat{c} = (0.59, 0.81)$. At $t = 0$: '– – –' and $t = 0.5$: '———' using (a) a 2nd-order kernel, and (b) an 8th-order kernel.

efficiency.

3.4.2 Wave propagation using full-space kernels

The dispersive character of PSE when applied to hyperbolic problems was analyzed in §3.3. This character is exhibited in the following example involving a two-dimensional Gaussian pulse, initially

$$f(x, y) = \frac{1}{\pi\sigma^2} e^{-((x-x_0)^2+(y-y_0)^2)/\sigma^2},$$

that is allowed to convect at unit speed in a direction 54° relative to the x-axis, or the direction $\hat{\mathbf{c}} = (0.59, 0.81)$, on particles that are held fixed. Convection in this arbitrary direction avoids alignment with any grid symmetry. The initial configuration is shown in each plot of Figure 3.5; the pulse radius σ is 0.1. The spatial derivative in the convective operator is approximated with PSE, with $\kappa = 1.8$, first using a 2nd-order-accurate kernel and then an 8th-order-accurate one, on a uniform 51×51 grid. Thus, the core of the pulse is 11 particles in diameter.

After 0.5 units of time, the pulse in the 2nd-order case has significantly dispersed, as Figure 3.5(a) shows, but in the 8th-order case of Figure 3.5(b), the pulse has not deformed and is located at the correct position.

3.4.3 Wave propagation using one-sided kernels

The previous example illustrated the use of PSE in convection problems when particle coverage is sufficiently isotropic about the kernel center. But this is not the case near the edge of the computational domain, and one-sided kernels are useful in such circumstances. We solve the same problem here as in the previous example, situating the pulse initially at the center of the domain. Eventually the pulse travels to the upper right corner of the domain. Figure 3.6 demonstrates the instability that results from a waveform trying to pass out of a domain using an 8th-order-accurate full-space kernel. When the particles near the corner acquire strength, they lack neighbors downwind of the propagation direction with which to exchange their strength.

When a one-sided kernel is used, with the half-plane of integration chosen to coincide with the upwind direction, the instability of the full-space kernel is avoided, as demonstrated in Figure 3.7. The kernel used here, which is 3rd-order-accurate, only exchanges strength with particles on the upwind side of the pulse and thus has no difficulty near the boundary. Only slight dispersion of the pulse is apparent.

3.4.4 Assessment of the effects of grid distortion

The previous examples were computed on stationary grids for simplicity; a clear assessment of how PSE behaves when its quadrature points are dispersed by the flow map is also important. Consider the same Gaussian pulse, now convected with the velocity field $\mathbf{u} + \hat{\mathbf{c}}$, where $\hat{\mathbf{c}} = (0.59, 0.81)$ as before, and $\mathbf{u}$ is to be specified. Though not based on physics, this problem exhibits features that arise in physical phenomena. For instance, an acoustic wave that travels through a vortical region is convected by a velocity that is the sum of the fluid velocity and the local speed

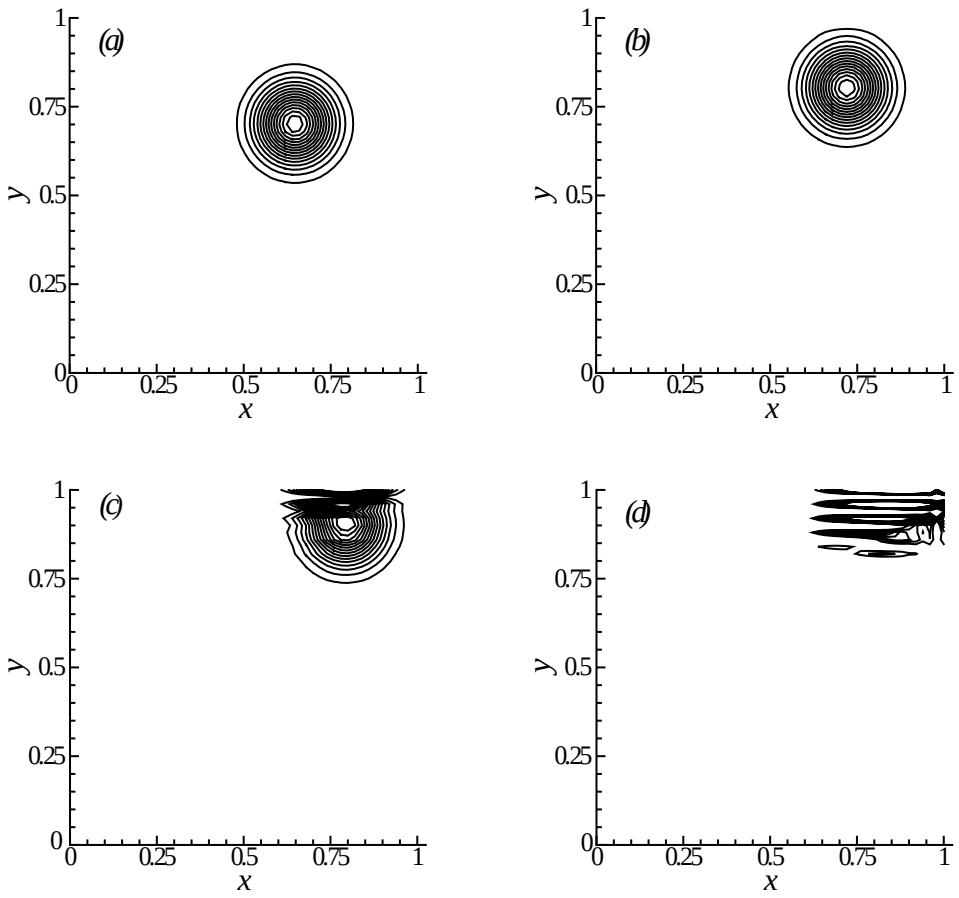

Figure 3.6: 8th-order full-space kernel in convection near corner. At (a) $t = 0.25$, (b) 0.375, (c) 0.5, and (d) 0.625.

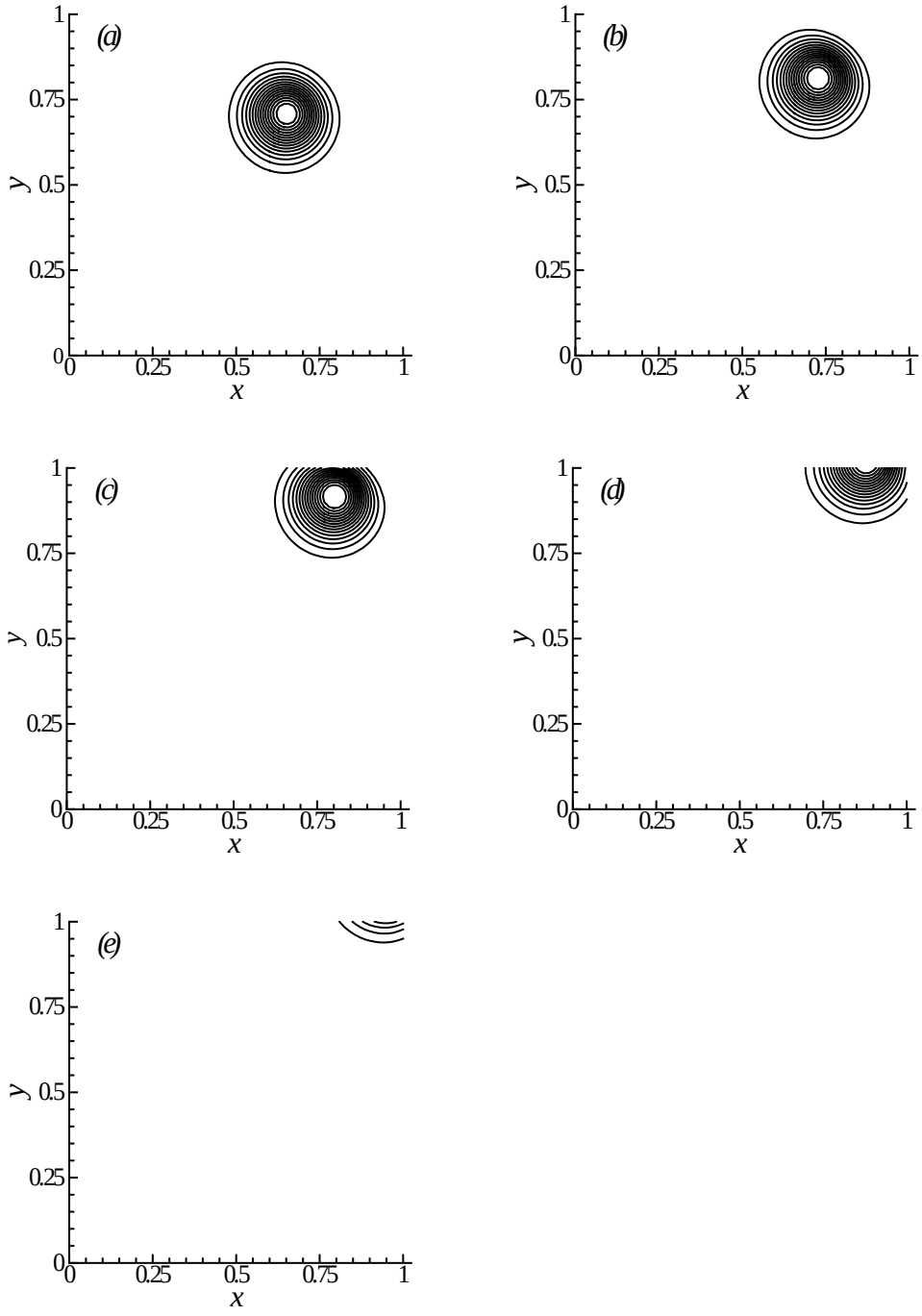

Figure 3.7: 3rd-order one-sided kernel in convection near corner, with one-sided integration plane aligned with upwind of propagation direction. At (a) $t = 0.25$, (b) 0.375, (c) 0.5, (d) 0.625, and (e) 0.75.

of sound. The equations governing the particles in the convecting frame are taken to be

$$\begin{aligned}
\frac{d\tilde{f}_p}{dt} &= 0, \\
\frac{d\tilde{\mathbf{x}}_p}{dt} &= \mathbf{u}(\tilde{\mathbf{x}}_p(t)) + \hat{\mathbf{c}}, \\
\frac{d\tilde{V}_p}{dt} &= \operatorname{div} \mathbf{u}(\tilde{\mathbf{x}}_p(t))\tilde{V}_p(t).
\end{aligned}$$

If initially $\tilde{\mathbf{x}}_p(0) = \xi_p$, $\tilde{f}_p(0) = g(\xi_p)$ and $\tilde{V}_p(0) = \Delta x^2$, then the solution is simply $\tilde{f}_p(t) = g(\xi_p)$, $\tilde{\mathbf{x}}_p = \xi_p + \hat{\mathbf{c}}t + \int_0^t \mathbf{u}(\tilde{\mathbf{x}}_p(\tau)\, d\tau$, and $\tilde{V}_p(t) = J(t;\xi_p)\Delta x^2$, where $J(t;\xi)$ is the Jacobian of the flow map. However, this problem can also be solved by convecting the particles with velocity $\mathbf{u}$ and treating the convection by $\hat{\mathbf{c}}$ through a modification of the particle strengths. In this new frame,

$$\begin{aligned}
\frac{df_p}{dt} &= -(\hat{\mathbf{c}} \cdot \nabla f)(\mathbf{x}_p(t)), \\
\frac{d\mathbf{x}_p}{dt} &= \mathbf{u}(\mathbf{x}_p(t)), \\
\frac{dV_p}{dt} &= \operatorname{div} \mathbf{u}(\mathbf{x}_p(t))V_p(t).
\end{aligned}$$

As in the previous examples, the right-hand side term of the first equation is treated with PSE. We will separately consider two different types of velocity fields, $\mathbf{u}$: the first induced by a Gaussian-distributed vortex with circulation Γ_0 at the center of the domain, the second induced by a Gaussian source of strength Q_0 at the same position. Both Gaussians have the same radius as the pulse, $\sigma = 0.1$, which is initially placed at $(0.25, 0.25)$.

Under the vortex-induced velocity with $\Gamma_0 = 0.5$, the grid distortion after 0.25 units of time (or 25 time steps) is as shown in Figure 3.8. The solution using 8th-order-accurate PSE with $\kappa = 1.8$ is plotted with the exact solution at this time level in Figure 3.9. The agreement is quite good, despite the dramatic stretching of the grid near the center of the domain. However, increasing the strength of the vortex to $\Gamma_0 = 0.85$ leads to break-up of the pulse as it passes through this

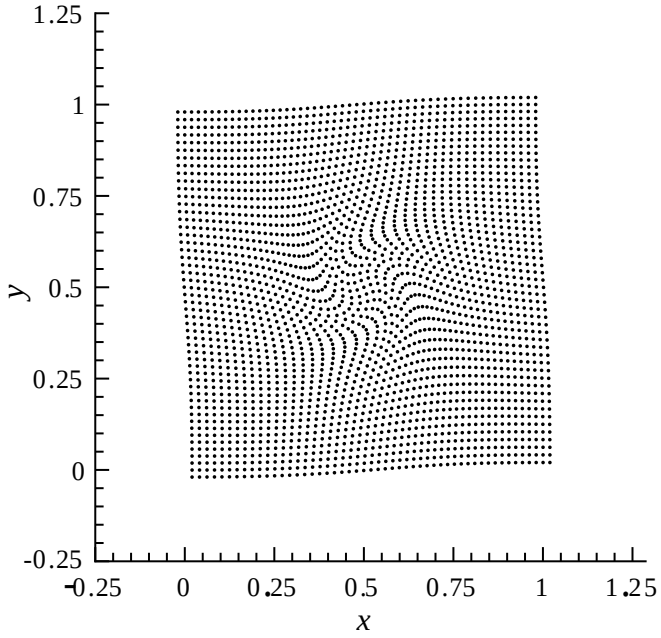

Figure 3.8: Particle grid distorted by Gaussian vorticity field, $\Gamma_0 = 0.5$, at $t = 0.25$.

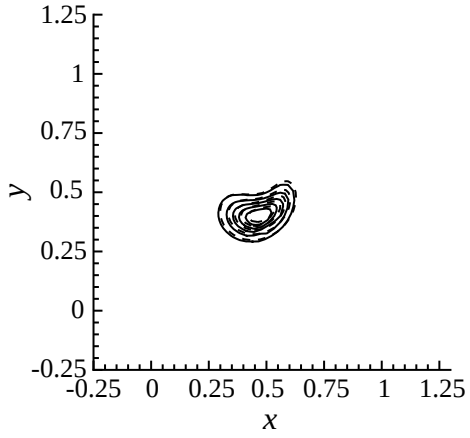

Figure 3.9: Convection in $\hat{c} = (0.59, 0.81)$ plus Gaussian vorticity field, $\Gamma_0 = 0.5$, at $t = 0.25$. Using PSE: '———'; exact: '– – –'.

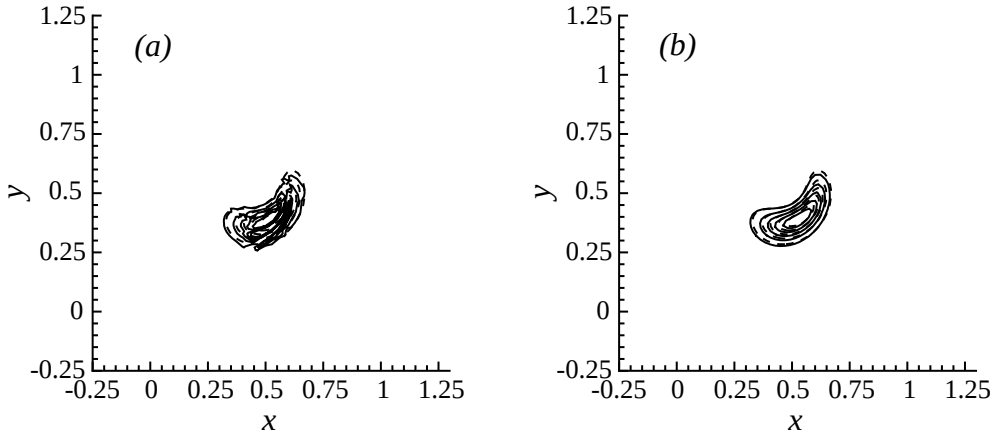

Figure 3.10: Gaussian vorticity field, $\Gamma_0 = 0.85$, at $t = 0.25$. (a) Without remeshing, and (b) remeshing every 10 steps. Using PSE: '———'; exact: '– – –'.

straining region, as shown in Figure 3.10(a). Remeshing onto a uniform grid every 10 steps prevents the particles from becoming too dispersed, and Figure 3.10(b) shows that the the exact solution is well-approximated.

A source-induced velocity leads to dilatation of the particles, as shown in Figure 3.11 for $Q_0 = 0.2$ at $t = 0.35$, from which the obvious consequence is a loss of overlap of particles, as the kernel radius is held constant. Indeed, the pulse has become unstable at $t = 0.35$, depicted in Figure 3.12(a). Remeshing every 10 steps prevents the particle spacing from growing beyond ε, and the pulse convects cleanly through the center of the domain as shown in Figure 3.12(b).

If the particle grid undergoes dilatation without significant anisotropic straining, as in this example, then the need for remeshing may be delayed, or eliminated altogether. PSE can be adapted to account for variably-sized particles, using a known mapping to a uniform grid, as shown by Cottet, Koumoutsakos and Salihi (2000), or by simply allowing variable kernel radius in the PSE operator, as described by Ploumhans and Winckelmans (2000). We demonstrate the latter method here. The local kernel radius is continuously adjusted to keep its ratio to the inter-particle spacing near κ. To preserve the symmetry of the PSE operator,

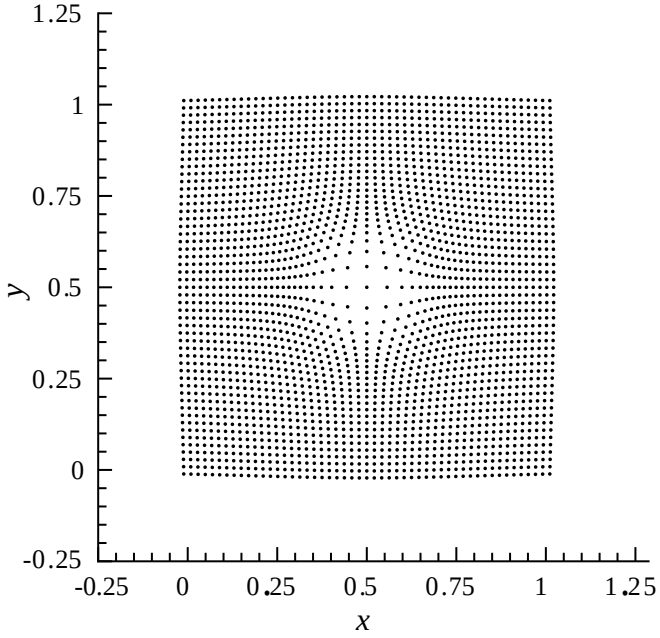

Figure 3.11: Particle grid distorted by Gaussian source field, $Q_0 = 0.2$, at $t = 0.35$.

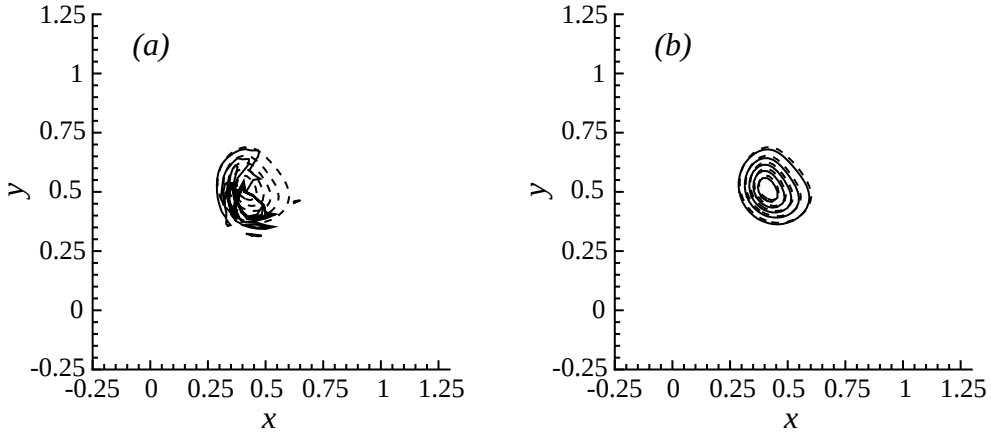

Figure 3.12: Gaussian dilatation field, $Q_0 = 0.2$, at $t = 0.35$. (a) Without remeshing, and (b) remeshing every 10 steps. Using PSE: '———'; exact: '– – –'.

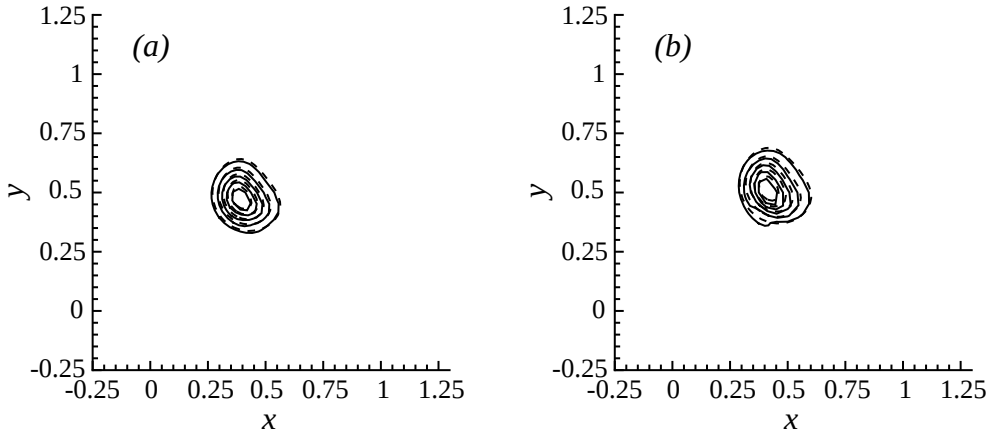

Figure 3.13: Gaussian dilatation field, $Q_0 = 0.2$. (a) At $t = 0.30$, and (b) at $t = 0.35$. Variable-kernel-size PSE: '———'; exact: '– – –'.

a mean of the squares of the kernel radii of particles p and q is used:

$$\varepsilon_{pq}^2 = \frac{\kappa^2}{2}(V_p(t) + V_q(t))$$

The results using this technique are shown in Figure 3.13. In (a), at $t = 0.30$, the pulse is passing through the region of expanded particles, but still matches the exact solution quite well. The pulse at $t = 0.35$ exhibits some deformation, depicted in (b). However, it is apparent that variable-kernel-size PSE has at least delayed the need for remeshing. This adjustment is useful for flows of larger Mach number, in which fluid dilatation can cause faster growth of particle volumes.

Although remeshing is essential to vortex particle methods, strategies for its frequency are traditionally based on trial and error. In §4.2.2 we develop a criterion for the frequency with which to remesh. The principle of the criterion is based on the distortion of neighboring particles by the flow map and uses the eigenvalues and principal axes of the rate-of-strain tensor.

Chapter 4

Practical considerations

The DVPM requires some additional work before it is ready for high-fidelity flow simulation. Some of these features are essential elements of the incompressible method and only require some simple modification to adapt them for use with compressible particles. For instance, the velocity computation is prohibitively expensive as it stands, but with careful treatment can be made much more efficient. We will adapt a popular technique in particle methods to improve this efficiency. Also, the induced velocity field invariably contains regions of high strain rate in which particles are pulled apart or pushed together, thereby degrading the accuracy of the computation. It is thus important to occasionally reinitialize the particles on a uniform grid. Such a treatment is common to vortex methods, although there has evidently been no discussion of the necessary frequency with which it should be applied aside from trial and error. We will describe the remeshing procedure and its caveats in compressible flow, as well as offer a theoretically-motivated criterion for the frequency.

Finally, the application of a vortex method to wave phenomena is unique to the present work, and thus a procedure by which waves are allowed to be transmitted from limited particle coverage must be developed without guidance from other Lagrangian methods. We will draw on previous experience of fixed-grid schemes in these matters and propose a simple treatment.

4.1 Fast summation

Each particle possesses a velocity field, due both to its vorticity and its dilatation, to which every other particle is subjected. With N particles, this means that without special treatment, $O(N^2)$ operations are required every time the particle velocities must be computed, which prohibits practical simulations using more than a few thousand particles. It is apparent, however, that the velocities induced by two nearby particles at a point some distance away are almost identical. In fact, an entire cluster of particles can be regarded as inducing a collective velocity field at this point. Several "fast summation methods" exploit this principle to reduce the number of operations to $O(N \log N)$ or $O(N)$ (Barnes and Hut, 1986; Greengard and Rokhlin, 1987; Draghicescu and Draghicescu, 1995).

4.1.1 The fast multipole method for dilating vortex particles

We present here an adaptation of the fast multipole method (FMM) of Greengard and Rokhlin (1987) to dilating vortex particles. This method recognizes particles as singular monopole sources of a Poisson equation. The interactions of two well-separated monopole sources are lumped into interactions between the clusters to which they belong, through multipole expansions about the centers of the clusters. A cluster-cluster interaction is translated to an affected particle by a local Taylor expansion about the cluster center. The method consists of the repeated application of formulae that shift the centers of these multipole and local expansions to centers of parent or child clusters. A quad-tree structure is used to precisely define the interaction types. A quad-tree is constructed by forming a master box, subdividing it into four child boxes, subdividing each of those into four, and so on until some level of refinement is reached. The level of the master box is labelled 0, and all finer levels are numbered sequentially upward to the finest level, $nlev$. At a given level, a box has at most nine "near neighbors" (itself and the eight adjacent boxes); the remaining boxes on a level are called "well-separated". The particles are grouped into boxes at the finest level. Interactions between particles

in near-neighbor boxes are computed directly, while those between particles in well-separated boxes are accounted for through the various expansions.

The application of the FMM to vortex methods is discussed in detail by Puckett (1993), and consequently most details of the implementation will be omitted here. In the context of a fluid flow, each particle is regarded as a singularity in an otherwise irrotational and solenoidal flow. With this in mind, the FMM is adapted to the present method by regarding each particle as the collocation of a point vortex and point source—forcing terms of the Poisson equations (2.2). It is convenient in two dimensions to describe physical coordinates in terms of the complex variable $z = x_1 + ix_2$. Through this description the particle strength is also complex, $S_p = Q_p - i\Gamma_p$. The velocity field induced on a distant point z by a cluster of m particles centered at z_0 is

$$F(z) = u_1 - iu_2 = \sum_{k=0}^{P} \frac{a_k}{(z - z_0)^{k+1}},$$

where

$$a_k = \frac{1}{2\pi} \sum_{p=1}^{m} S_p (z_p - z_0)^k, \quad k = 0, \ldots, P,$$

and P is the truncated number of terms. The velocity gradient tensor (2.16) can be computed efficiently with the same method, with little extra work, by using the derivative of the complex multipole expansion of the velocity field. Thus, the velocity gradient induced by the same cluster on a point z is

$$F'(z) = \frac{\partial u_1}{\partial x_1} - i\frac{\partial u_2}{\partial x_1} = -\sum_{k=1}^{P+1} \frac{k a_{k-1}}{(z - z_0)^{k+1}},$$

and the Cauchy-Riemann equations can be used to get the other components of the tensor. Figure 4.1 depicts the CPU time required to complete a single time step on a 500 MHz Compaq Alpha XP1000 workstation. The number of particles was varied from about 38,000 to about 277,000. The CPU time scales as $O(N)$ as

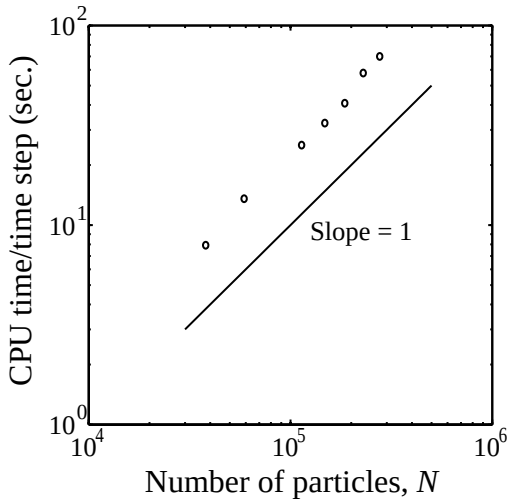

Figure 4.1: CPU time for several different particle populations.

predicted.

It is important to note that despite the description in terms of complex coordinates, the FMM is not limited to two-dimensional flows. The method has been extended to three-dimensional problems using the same basis of the multipole expansion, albeit with different formulae that employ spherical harmonics and an oct-tree structure in lieu of the quad-tree. Formulae are given by Epton and Dembart (1995) and the appendix of Cottet and Koumoutsakos (2000) provides a useful discussion.

4.1.2 A criterion for quad-tree refinement

The FMM was originally designed for singular particles. Since the width of such particles is zero, only one particle per box is required at the finest level of the quad-tree. A particle thus only directly communicates with eight neighbors. However, the blobs used in the present method have a finite size. For the multipole expansion of a cluster to be valid at a given point, the members of that cluster should be indistinguishable from the singularities that they are designed to resemble. This restriction necessitates larger boxes at the finest level to ensure only

direct interactions between particles that appear as blobs to one another. As the number of particles is changed, the quad-tree must be adjusted to keep the number of particles per box, N_{box}, within a certain range: if N_{box} is too small, then the near-neighbor list is too small and important direct interactions are neglected; if N_{box} is too big, then the computation time is dominated by unnecessary direct near-neighbor interactions.

We develop here a criterion for the degree of refinement of the quad-tree, based on the principles just described. Suppose that our blob function, ζ, has some radius ε. Then the smoothed velocity kernel (2.11) only significantly differs from the unmollified one within a sphere of radius $\phi\varepsilon$, where ϕ is a factor that is determined by the blob function and our definition of "significant." The blob functions considered in the present method are all proportional to a Gaussian, and their radial decay rate is almost entirely determined by the decay of the Gaussian. Thus, if we suppose an error tolerance tol, it follows that the discrepancy in the velocity kernels is not apparent beyond $\phi\varepsilon$, determined by $e^{-\phi^2\varepsilon^2/\varepsilon^2} = \text{tol}$, which leads to $\phi = \sqrt{\log(1/\text{tol})}$. For instance, if $\text{tol} = 10^{-6}$, then $\phi = 3.7$. Two particles that interact through the expansions of their clusters—in other words, two particles that are well-separated—must appear singular to each other. The minimum separation between two such particles is the side length, Δ_{nlev}, of a box at the finest level (e.g., particles A and B in Figure 4.2). Thus, we must have that $\Delta_{nlev} > \phi\varepsilon$. This is our criterion for the degree of refinement.

It would be more useful, however, to express this in terms of $nlev$ itself. If Δ_0 is the side length of the master box, then $\Delta_{nlev}/\Delta_0 = 2^{-nlev}$. Thus, we require that $2^{-nlev}\Delta_0 > \phi\varepsilon$. If we simply fix the size of the master box to just enclose all of the particles, however, our refinement scheme will not always be efficient. Consider the situation shown in Figure 4.2. The circle centered at particle A only slightly intersects the nearest well-separated box, but if we decrease $nlev$ by one, the blob is well within the confines of the near-neighbor region. The goal should be to make this inequality as near to an equality as possible by simultaneously varying Δ_0 and $nlev$. Let L be the maximal extent of the particle coverage along either

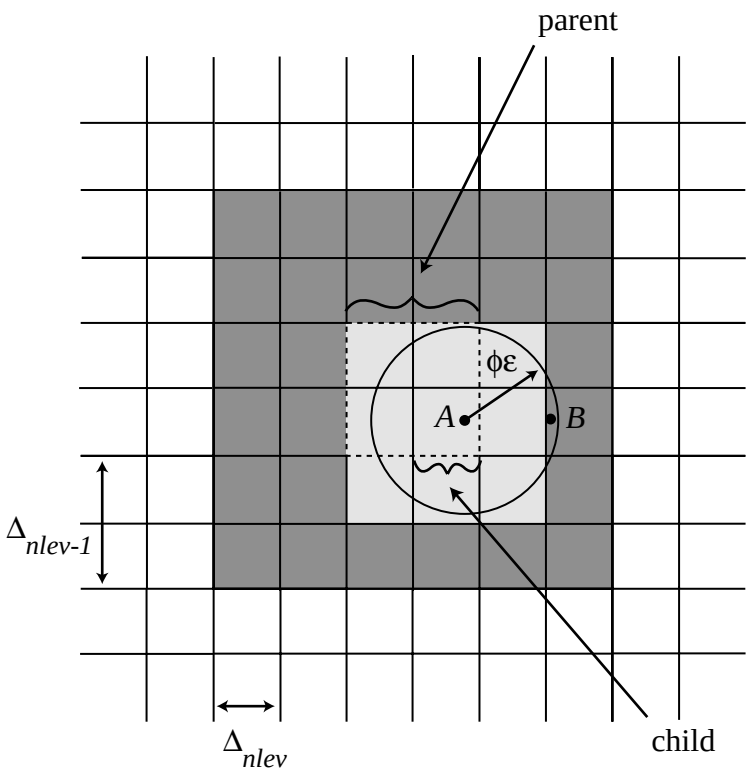

Figure 4.2: Schematic of finest boxes of quad-tree structure. The light gray boxes are the nearest neighbors of the labelled child box, and the dark gray boxes are the nearest neighbors of its parent.

of the coordinate directions (i.e., $L = \max(|x_{1,max} - x_{1,min}|, |x_{2,max} - x_{2,min}|)$). Then we restrict Δ_0 to the range $L \leq \Delta_0 < 2L$. Let $\Delta_0 = \lambda L$. Our procedure is as follows:

1. Propose a preliminary refinement, $\widetilde{nlev}$, based on the lower bound for Δ_0:

$$\widetilde{nlev} = \text{int}\left(\frac{\log(L/(\phi\varepsilon))}{\log(2)}\right)$$

2. Check if $\Delta_{\widetilde{nlev}}$ is within 5% of $\phi\varepsilon$:

$$\frac{\Delta_{\widetilde{nlev}} - \phi\varepsilon}{\Delta_{\widetilde{nlev}}} \overset{?}{<} 0.05 \Longrightarrow \widetilde{nlev} \overset{?}{>} \frac{\log(0.95L/(\phi\varepsilon))}{\log(2)}$$

If so, then set $nlev = \widetilde{nlev}$. If not, then

3. Set $nlev = \widetilde{nlev} + 1$ and set λ such that $\lambda L 2^{-nlev} = \phi\varepsilon$, or

$$\lambda = \frac{\phi\varepsilon 2^{nlev}}{L}$$

When λ is near 2, there will likely be several boxes on the finest level that do not contain particles. However, these boxes are simply ignored in the calculations.

We can further improve the efficiency of the calculations by noting that not *all* particles in the near neighbor boxes fall within the disk of radius $\phi\varepsilon$. For example, imagine that the circle in Figure 4.2 is wholly contained in the light gray region, as our criterion prescribes. While most of the box to the east of the main box would be enclosed by the circle, all of the other seven neighboring boxes are only partially enclosed. Thus, we are free to treat the interactions of particles in the unenclosed space with particle A as singular. In principle we could include these particles in clusters in the dark gray region and compute the interactions through the multipole expansions, but instead we compute the interactions directly, *without smoothing*, and avoid some extraneous work.

It is important to note that the hierarchy of boxes used in the FMM also provides a natural framework for efficiently computing other terms in the equations of the method. The PSE summations are truncated to include only interactions between particles in near-neighbor boxes—and among those interactions only those between particles within $\phi\varepsilon$ are considered. This treatment is consistent with the defining principle of the criterion, that particles only resemble blobs inside a disk of radius $\phi\varepsilon$, because PSE kernels are closely related to the blob function and decay with nearly the same rapidity. Although high-order-accurate PSE kernels have larger support than lower-order ones, their support is still confined to this disk, and interactions beyond this are neglected.

4.1.3 Performance

At this point it is appropriate to discuss the performance of the DVPM in comparison with a common fixed-grid scheme, such as a finite difference method. Such a comparison only makes sense with regard to problems that permit simulation by both methods. With the fast summation treatment, the most expensive part of the DVPM is the set of near-neighbor computations. The average number of particles per box at the finest level is $N_{box} \approx (\Delta_{nlev}/\Delta x)^2 = (\kappa\phi)^2$, where κ is the ratio of blob radius to interparticle spacing. Thus, for $\kappa = 1.5$ and $\phi = 3.7$, there are around 30 particles per box, and since a box has at most 9 near neighbors, a given particle must directly interact with around $9 \times 30 = 270$ other particles. However, by ignoring interactions between particles that are separated by more than $\phi\varepsilon$, as described in §4.1.2, we can reduce this number to around 100.

The goal of the quad-tree structure is to determine whether a particle at a given time is contained in the support of a PSE kernel centered at another particle, without explicitly computing the distance between them. A fixed grid obviates this procedure, requiring only an indexing system to determine relative positions between grid points. Moreover, a finite difference stencil consists of around 10 points, compared to the 100 in the PSE kernel support. The need for remeshing is certainly avoided by a fixed-grid scheme, but a curvilinear grid in such a method requires the additional calculation of the Jacobian. Compact finite difference schemes also require the inversion of a (sparse and well-structured) matrix. Overall, the performance of a fixed-grid scheme is likely better for problems in which both methods can be applied. However, with further development the DVPM may be capable of simulating flows in complex geometries not possible for fixed-grid schemes.

4.2 Remeshing

The need for remeshing arises because of the topology of the flow. The flow will often contain regions of high accumulated strain where fluid elements have been

stretched. Such behavior is reflected in those regions becoming sparsely populated with computational elements, thus violating the convergence requirement of vortex methods that the blobs overlap. Particles must periodically be redistributed to prevent such accumulation. It is desirable to conserve global flow quantities such as the mass, circulation and angular impulse in this process. Interpolation of this type was addressed by Schoenberg (1973) and has proved an essential part of SPH (Monaghan, 1985) and vortex particle methods (Cottet and Koumoutsakos, 2000).

Extra care must be taken when interpolating in the present method because of the sensitivity of the dilatation field to small error. This occurs because the first and second terms on the right-hand side of (2.14b) are in many cases in near-perfect balance[1]. The slight imbalance, however, is crucial to the production of sound as well as the stability of the method (see §2.3), and thus extremely important to compute accurately. Through trial and error, we have found that interpolation can degrade the smoothness of the enthalpy and introduce an error which is subsequently amplified by PSE. This error can overwhelm (2.14b) unless the interpolation error is substantially reduced. To ensure stability in the DVPM, many common interpolation kernels, such as the M_4' kernel of Monaghan (1985), carry stringent requirements of particle spacing and remeshing frequency. For instance, using the M_4' kernel in the co-rotating vortex problem discussed in §6.2, we found that stability demands that 21 particles be placed across the diameter of each vortex and that the particles be remeshed every step. We discovered that a higher-order interpolation with some degree of smoothing as described below, using kernels of Gaussian type, is much less restrictive, but at the cost of not exactly conserving the global quantities (although the departure is only slight). For the same problem, the 6th-order kernel derived presently requires only 13 particles and remeshing only every ten steps to remain stable. Further refinement reduces

[1] A rearrangement of the equations does not avoid this difficult balance, but merely transfers it to another set of terms. In a velocity-based scheme this delicate balance is apparent in the computation of the dilatation from $\frac{\partial u_1}{\partial x_1} + \frac{\partial u_2}{\partial x_2}$, in which each summand is often much larger than the sum.

the smoothing, thus making it necessary to remesh more frequently. In practice we remesh every one or two steps.

It should be pointed out that the need for smoothing in remeshing is not new to vortex methods. Cottet (1996) found in his incompressible simulations of decaying two-dimensional turbulence that a slightly dissipative remeshing scheme was necessary to prevent noise build-up from impeding the self-organizing of small-scale vorticity into large coherent eddies.

4.2.1 Interpolation

The interpolation can be expressed in a continuous sense as

$$\tilde{f}(\mathbf{x}) = \int W_\sigma(\mathbf{x}-\mathbf{y}) f(\mathbf{y})\, d\mathbf{y} \tag{4.1}$$

where $\tilde{f}(\mathbf{x})$ is the new value of the function at position $\mathbf{x}$, $W_\sigma(\mathbf{x}) = W(\mathbf{x}/\sigma)/\sigma^2$ is the interpolation kernel scaled by the interpolation radius, σ, alternatively regarded as the degree of smoothing in the interpolation. The error of this interpolation is $||\tilde{f} - f|| = O(\sigma^r)$, where r is the order of accuracy of the interpolation kernel. The form of equation (4.1) is similar to the integral operator of PSE. Using the same Taylor expansion approach here as in the PSE derivation in Chapter 3, we develop the relation

$$f(\mathbf{x}) = \frac{1}{M_{(0,0)}} \left[\int W_\sigma(\mathbf{x}-\mathbf{y}) f(\mathbf{y})\, d\mathbf{y} - \sum_{j=1}^{\infty} \sum_{k=0}^{j} \frac{(-\sigma)^j}{j!} D^{(k,j-k)} f(\mathbf{x}) M_{(k,j-k)} \right],$$

where $D^{(\alpha_1,\alpha_2)}$ is the usual differential operator and the moments M_α are defined as in Chapter 3:

$$M_\alpha = \int_{-\infty}^{\infty} \int_{-\infty}^{\infty} y_1^{\alpha_1} y_2^{\alpha_2} W(\mathbf{y})\, dy_1\, dy_2. \tag{4.2}$$

The conditions on these moments are given by

$$M_\alpha = \begin{cases} 1, & \alpha = (0,0), \\ 0, & |\alpha| \in [1, r-1], \end{cases} \tag{4.3}$$

as well as

$$\int_{-\infty}^{\infty}\int_{-\infty}^{\infty} |\mathbf{y}|^r |W(\mathbf{y})|\, dy_1\, dy_2 < \infty. \tag{4.4}$$

Note that these conditions are *identical* to those imposed on the blob function, ζ. We have chosen to use a template that is the product of two one-dimensional polynomials and a Gaussian:

$$W(x_1, x_2) = \frac{1}{\pi}\left(\sum_{j=0}^{m} \gamma_j x_1^{2j}\right)\left(\sum_{j=0}^{m} \gamma_j x_2^{2j}\right) e^{-(x_1^2+x_2^2)}, \tag{4.5}$$

where $m = r/2-1$. Kernels of this family are more smooth than the M_4' kernel—the M_4' kernel does not have continuous derivatives at distances of one and two particle spacings away—and thus have better stability properties. Through experience we have found that a 6th-order kernel works well for interpolation:

$$W(x_1, x_2) = \frac{1}{\pi}\left(\frac{15}{8} - \frac{5x_1^2}{2} + \frac{x_1^4}{2}\right)\left(\frac{15}{8} - \frac{5x_2^2}{2} + \frac{x_2^4}{2}\right) e^{-(x_1^2+x_2^2)}.$$

The particle vorticity, dilatation, density, entropy and enthalpy are interpolated using the discrete analog of (4.1),

$$\tilde{f}_p = \sum_q W_\sigma(\tilde{\mathbf{x}}_p - \mathbf{x}_q) V_q f_q, \tag{4.6}$$

where $\sigma = 1.7\Delta x$, $\{V_p\}$ are the old particle volumes, and $\{\tilde{\mathbf{x}}_p\}$ are the new particle positions.

The integral moment conditions on W ensure the invariance of the corresponding integral moments of the interpolated quantities during remeshing, some of

which are governed by physical conservation laws in two-dimensional flows. For instance, the zeroth moments of density and vorticity—the mass and circulation, respectively—are conserved. It is thus important that these quantities not change appreciably during remeshing.

4.2.2 A criterion for the frequency of remeshing

It would be helpful to have some guidance on how frequently remeshing is necessary to preserve the integrity of a flow simulation. As we showed in §3.4.4, the PSE operators are sensitive to distortion of the particle grid. The quadrature of the integral operator over a set of particle locations relies on those particles having some degree of uniformity in their distribution. While some distortion is acceptable, the accuracy is quickly degraded beyond some threshold.

The development of a remeshing criterion will depend on somehow quantifying this threshold. The stability of the PSE approximation is contingent upon the maintenance of overlap of adjacent particles, but the accuracy of the approximation can be poor even while overlap is maintained. It proves to be quite difficult to determine a general rule by which to measure acceptable grid distortion. If, for instance, we use the experience of practitioners of finite element methods, which share a common interpolating principle with quadrature, and adapt their guidelines for element distortion, then we are tempted to use as measures the aspect ratio or the internal angles of the quadrilaterals formed by neigboring particles. However, finite elements are self-contained entities that do not rely on the quality of neighboring elements, whereas quadrature in a particle method requires a larger region of acceptably distributed particles. Also, midpoint quadrature is more sensitive to distortion than higher-order finite elements.

Certainly there are many factors that the degradation of quadrature will depend on, for examples the local strain rate and the magnitude of the derivative that we are approximating with PSE. Instead of attempting to establish a strict cause-and-effect relationship between particle distortion and quadrature degradation, we will construct a criterion that is based on empirical observation of previous results,

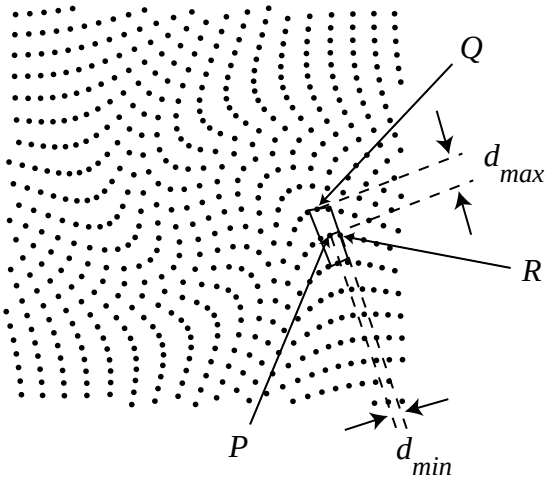

Figure 4.3: Definition of aspect ratio of neighboring particles, $\rho = d_{max}/d_{min}$.

and connect it with an analysis of the distortion of the particle grid by a general flow map. For this connection we will use the largest aspect ratio of neighboring particles at the time of remeshing in these previous computations. Such a choice is only meant to serve as a loose guideline and should be interpreted liberally.

Consider the distorted particle configuration depicted in Figure 4.3. A quadrilateral surrounding a typical particle P is drawn through its four cardinal neighbors (i.e., these four particles were originally located at the cardinal directions from P on the Cartesian grid). We define the aspect ratio, ρ, as the ratio of the largest radius of this quadrilateral to its smallest radius, $\rho = d_{max}/d_{min}$. The quadrilateral shown has been simultaneously stretched and rotated by the flow, but we argue that the rotation is unimportant to the quadrature. We will derive an approximate expression for the largest such aspect ratio for a given flow map, and use the criterion described to find the time between remeshings.

Consider a material point P initially located at ξ_P, whose position at some time t is given by the flow map: $\mathbf{x}_P(t) = \mathbf{X}(\xi_P; t)$. A nearby point Q with initial position $\xi_Q = \xi_P + \Delta\xi$ has the subsequent position

$$\mathbf{x}_Q(t) = \mathbf{X}(\xi_Q; t) = \mathbf{X}(\xi_P + \Delta\xi; t) \approx \mathbf{x}_P(t) + \frac{\partial \mathbf{X}}{\partial \xi_j}\Delta\xi_j.$$

Thus, $\Delta x_i(t) = x_{Q,i} - x_{P,i} \approx J_{ij}\Delta\xi_j$, where $J_{ij} = \partial X_i/\partial\xi_j$ is the strain tensor of the flow map. We are concerned with how this strain tensor distorts the initially uniform particle grid, and for this we must consider the relative velocities of the two points. The velocity of P at $t = 0$ is $\mathbf{u}(\xi_P, 0)$ and that of Q is

$$\mathbf{u}(\xi_Q, 0) \approx \mathbf{u}(\xi_P, 0) + \frac{\partial \mathbf{u}}{\partial x_j}\Delta\xi_j.$$

The rate of change of the distance between P and Q, $s = \sqrt{\Delta x_i \Delta x_i}$, is determined by the velocity gradient tensor, $\Sigma_{ij} = \partial u_i/\partial x_j$:

$$\begin{aligned}\frac{ds^2}{dt} &= \frac{d}{dt}(\Delta x_i \Delta x_i) \\ &= 2\Delta x_i \Delta u_i \\ &\approx 2\Delta x_i \Sigma_{ij} \Delta x_j.\end{aligned}$$

Because of the symmetry of the right-hand side, only the symmetric part of the velocity gradient tensor, which is called the deformation tensor and whose elements are $D_{ij} = \frac{1}{2}\left(\frac{\partial u_i}{\partial x_j} + \frac{\partial u_j}{\partial x_i}\right)$, contributes to the rate of change of s. Thus, the fractional rate of change of s is given by

$$\frac{1}{s}\frac{ds}{dt} = D_{ij}\frac{\Delta x_i}{s}\frac{\Delta x_j}{s}.$$

The ratios on the right-hand side are the components of the unit vector at P in the direction of Q, which we call l_i. Consider now the expansion of s about the initial time $t = 0$. Then at a later time $t = \Delta t$,

$$\begin{aligned}s(\Delta t) &\approx s(0) + \Delta t \frac{ds}{dt}(0) \\ &= s(0) + \Delta t\; D_{ij} l_i l_j|_{t=0}\, s(0) \\ &= s(0)\left(1 + D_{ij} l_i l_j|_{t=0}\, \Delta t\right).\end{aligned}$$

Suppose now that material point P is associated with a computational particle, and Q and R are material points associated with particles that are located at

neighboring points of a uniform grid at $t = 0$. Thus, the initial separation of P from both Q and R is $s_{Q,R}(0) = \Delta x$. After some time, the particle positions are distorted, as for instance in Figure 4.3. We define the aspect ratio as the ratio of the larger to the smaller of the distances between P and the two neighbors:

$$\rho = \frac{\max\limits_{j=(Q,R)} s_j}{\min\limits_{j=(Q,R)} s_j}.$$

Our criterion requires that at this later time Δt, $\rho(\Delta t)$ shall not exceed some threshold ρ_{max}. The deformation tensor contains both the effects of pure strain and dilatation of fluid elements. The dilatation changes the distance to neighboring particles isotropically, so we can fairly ignore its contribution in this criterion. Thus, we only consider the rate-of-strain tensor, $\mathbf{S} = \mathbf{D} - \frac{1}{2}\theta\mathbf{I}$ (the factor of 1/2 is for two-dimensional flow only). Additionally, it is clear that the aspect ratio threshold will be violated at a point where the principal axes of strain are aligned with P–Q and P–R (i.e., aligned with the coordinate axes, x_1 and x_2). The magnitude of $S_{ij}l_il_j$ in these principal directions are λ_1, the largest eigenvalue of $\mathbf{S}$, which is necessarily positive; and λ_2, which is necessarily $-\lambda_1$ because of the zero trace of $\mathbf{S}$. Thus, the aspect ratio that we will use in comparison with ρ_{max} is

$$\rho = \frac{1 + \lambda_1 \Delta t_{rm}}{1 - \lambda_1 \Delta t_{rm}},$$

where it is understood that this expression is to be evaluated at $t = 0$. If we define Δt_{rm} as the time interval between remeshings, then we find that we must have

$$\Delta t_{rm} < \frac{1}{\lambda_{1,max}} \left(\frac{\rho_{max} - 1}{\rho_{max} + 1} \right), \tag{4.7}$$

where the maximum of λ_1 is evaluated over all particle positions at which the principal axes are aligned with the grid axes. The location of this maximum is termed the "point of critical strain."

We now turn our attention to finding the conditions under which these principal

axes are so aligned. In two-dimensional flow,

$$S_{11} = -S_{22} = \frac{1}{2}\left(\frac{\partial u_1}{\partial x_1} - \frac{\partial u_2}{\partial x_2}\right),$$
$$S_{12} = S_{21} = \frac{1}{2}\left(\frac{\partial u_1}{\partial x_2} + \frac{\partial u_2}{\partial x_1}\right).$$

It is simple to show that the largest eigenvalue of $\mathbf{S}$ is $\lambda_1 = \sqrt{S_{11}^2 + S_{12}^2}$ and the corresponding normalized eigenvector is

$$\boldsymbol{\xi}_1 = \frac{1}{\sqrt{2}} \begin{pmatrix} \mathrm{sgn}(S_{12})\sqrt{1 + S_{11}/\lambda_1} \\ \sqrt{1 - S_{11}/\lambda_1} \end{pmatrix},$$

except when $S_{12} = 0$, in which case the eigenvector is

$$\boldsymbol{\xi}_1 = \begin{pmatrix} 1 \\ 0 \end{pmatrix} \quad \text{or} \quad \begin{pmatrix} 0 \\ 1 \end{pmatrix}$$

if $S_{11} > 0$ or $S_{11} < 0$, respectively. Therefore, the eigenvector of maximum strain is aligned with the x_1-axis when $S_{12} = 0$ and $S_{11} > 0$, and the x_2-axis when $S_{12} = 0$ and $S_{11} < 0$. Our search for the point of critical strain should be confined to those particle positions at which $\frac{\partial u_1}{\partial x_2} = -\frac{\partial u_2}{\partial x_1}$, and among these the positions at which $|S_{11}|$ is maximum. Once this is determined, the time interval between remeshings is computed through (4.7). Note that this parameter can sometimes be determined prior to a simulation, based only on the initial conditions, but its determination throughout the course of a computation adds very little cost as the velocity gradient is already computed.

As an example, consider the velocity field of a Gaussian distribution of vorticity, as in §3.4.4:

$$\omega(\mathbf{x}, 0) = \frac{\Gamma_0}{\pi\sigma^2} e^{-|\mathbf{x}|^2/\sigma^2}.$$

It can be shown for such a configuration that the local eigenvectors are aligned with the coordinate axes for all points along the diagonal axes, and the maximum

eigenvalue among these points is at a radial location of $r/\sigma = 1.34$, with a value of $\lambda_{1,max} = 0.0474\Gamma_0/\sigma^2$. In this example, then, the maximum aspect ratio after Δt units of time is approximately

$$\rho = \frac{1 + 0.0474\Gamma_0\Delta t/\sigma^2}{1 - 0.0474\Gamma_0\Delta t/\sigma^2}.$$

We found in the convecting pulse example of §3.4.4 that remeshing needed to occur every 0.1 units of time when $\Gamma_0 = 0.85$ and $\sigma = 0.1$. The maximum aspect ratio at this time is approximately 2.35. As a general threshold for the aspect ratio, we will take the much more conservative value of $\rho_{max} = 1.25$, and by (4.7), require

$$\lambda_{1,max}\Delta t_{rm} < 1/9. \tag{4.8}$$

We have found that this value works well in practice. However, it is important to note that this criterion should be interpreted as only a guideline, and not a hard rule. Ultimately the decision of remeshing frequency is problem-specific.

4.3 Spatial compactness and domain truncation

Extending a vortex particle method from its common use in hydrodynamics to compressible flows introduces the issue of dealing with an unbounded domain computationally. In hydrodynamics, the vorticity field, if initially compact, stays compact. One of the major motivations for vortex methods is that the particles that carry the vorticity *define* the computational domain, so the methods are efficient and in the absence of solid boundaries all boundary conditions are implicity accounted for by the Biot-Savart integral. Compressible flows inherently contain radiated components, which are *not* spatially compact. If this radiation is to be accomodated in a numerical method by the exchange of strengths described above, then some means must be provided that allow the outer particles to exchange strength with an infinite region exterior to the particles. Furthermore, the integral for computing the irrotational component of the velocity (the second term of equation (2.4)) must

be addressed, because its integrand does not confine itself to the particle coverage.

We note that in general it may be possible to retain some measure of the spatial compactness associated with incompressible vortex methods in the extension to compressible flow. It is known that the sources of acoustic waves can be written in terms that are linear in the vorticity and entropy, provided that the stagnation enthalpy, $B = h + \frac{1}{2}|\mathbf{u}|^2$, is taken as the acoustic variable[2]. This shows, then, that the radiated acoustic field may only need to be discretized to a distance, beyond which its amplitude is small enough that its effect on the particle's motion can be neglected. In this external field, the irrotational flow is governed by a linear wave equation. We believe that this feature could be exploited to obviate the need for particle placement in this outer region, but have not yet developed a systematic procedure to carry it out.

Instead, we propose here a simpler approach, wherein particles are retained to a somewhat larger distance into the acoustic field. At this distance, we merely truncate the computational domain, and apply an artificial boundary condition to attempt to allow for only outgoing acoustic waves (i.e., we apply a so-called non-reflecting boundary condition). Non-reflecting boundary conditions remain an active area of research (see reviews by Givoli (1991) and Tsynkov (1998)). While much progress has been made in developing conditions for linear problems, nonlinear boundary conditions are still in their nascent stage. It will be assumed that, away from the "source" region (usually the region of rotational flow), the particle velocities and fluctuations in the other flow quantities will be much smaller than their characteristic values in the source region. Under such conditions, the governing equations reduce to the linear wave equation and thus, linear boundary conditions are justified.

[2]This result is embodied in Howe's acoustic analogy (Howe, 1975), but we refer here primarily to the form developed by Möhring (1997), for which the wave operator in the otherwise irrotational and isentropic media takes on a somewhat simplified and self-adjoint form.

4.3.1 Boundary condition and enforcement

The Engquist-Majda (Engquist and Majda, 1977) hierarchy of conditions have been successfully applied to a variety of wave propagation problems. The conditions are developed by forming a series of Padé approximations to the Fourier-transformed pseudo-differential operator representation of Sommerfeld's radiation condition. The conditions are developed for both planar and circular boundaries. For most problems, a circular domain rather than rectangular is used to avoid complications at the corners. When the term "boundary" is used here, it denotes the farthest extent of particle coverage. The first member of the hierarchy is

$$\left(\frac{\partial f}{\partial t} + \frac{\partial f}{\partial r} + \frac{f}{2r}\right)_{r=R} = 0, \tag{4.9}$$

where f is any quantity governed by the linear wave equation and R is the radial position at which the condition is to be imposed. A means must be developed for enforcing the condition. We create a set of boundary particles, which lie on the periphery of the coverage in a "boundary zone," that has a different set of properties from the interior set. The new particles translate as the others do (albeit with a very small motion), but their enthalpy h_p is governed by

$$\frac{dh_p}{dt} = -\left(\frac{\partial h}{\partial r}\right)_p - \frac{(h_p - h_\infty)}{2R_p} \tag{4.10}$$

instead of (the particle form of) equation (2.14f), where R_p is the radial distance of the particle from the origin. Their dilatation, vorticity (which is zero by assumption) and entropy are held constant. The boundary zone has a depth that depends on the blob radius of the particles; typically only a few particles' depth is required.

The spatial derivative in (4.10) is approximated using PSE. However, the technique of approximating the derivative by a full-space integral is inaccurate. A kernel centered at a point near the boundary expects to have information available from an approximately circular (or in three dimensions, spherical) region

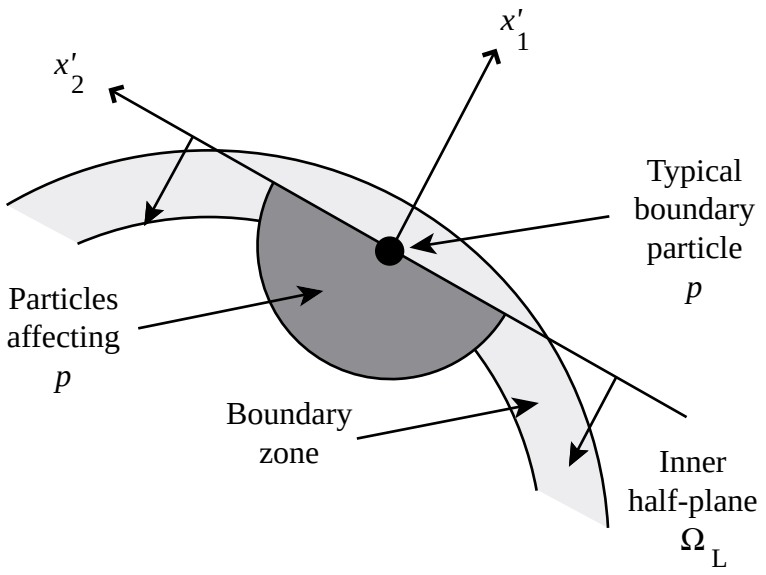

Figure 4.4: Schematic of the boundary treatment.

surrounding the point. If any portion of this region fails to intersect with the computational domain, then the subsequent quadrature of the integral will be poor. In these cases a half-space integral is used in lieu of the full-space version (see §3.2.2). The particle-discretized formula is described in Appendix A. If a line (or plane) is drawn through the point in question, parallel to a tangent of the near boundary (see Figure 4.4), then the integration proceeds over the "inner" half-space Ω_L that contains the domain. The quadrature of the integral will only involve particles located in the half-disc shown (or an analogous hemisphere in three dimensions), corresponding to the intersection of the kernel support with the half-space.

Note that for the second term in the velocity calculation (2.4), the integration is simply truncated at the boundary of particle coverage. For most flows of interest, the irrotational component is significantly smaller than the solenoidal, and furthermore the dilatation external to the domain is likely to contribute very little to this small irrotational part.

4.3.2 Error analysis

We will show that the largest contribution to the error inherent in the PSE-approximated form of (4.9) is due to the incomplete annihilation of an incident wave by the original boundary conditon. We call this PSE-modified operator $\hat{E}_1$:

$$\hat{E}_1 f = \left(\frac{\partial f}{\partial t} + L_L^\beta f + \frac{f}{2r} \right)_{r=R},$$

where the operator L_L^β is the left-sided PSE operator defined in (3.15). We wish to show that the magnitude of $|\hat{E}_1 f|$, evaluated at $r = R$, converges to zero. Use the triangle inequality:

$$\begin{aligned} |\hat{E}_1 f| &= \left| \frac{\partial f}{\partial t} + L_L^\beta f + \frac{f}{2r} \right| \\ &= \left| \frac{\partial f}{\partial t} + \frac{\partial f}{\partial r} - \frac{\partial f}{\partial r} + L_L^\beta f + \frac{f}{2r} \right| \\ &\leq |E_1 f| + \left| \frac{\partial f}{\partial r} - L_L^\beta f \right|, \end{aligned}$$

where it is understood that the terms on the right-hand side are evaluated at $r = R$. We consider the magnitude of both of these terms separately. The first term is due to the boundary condition itself. Let us assume the general expansion form for a quantity f that is propagated outward in the form of a radially-symmetric cylindrical wave:

$$f(r,t) = \sum_{n=0}^{\infty} r^{-n-1/2} f_n(t-r) \tag{4.11}$$

When we substitute this form into the boundary condition operator (4.9), the residual is

$$\mathcal{R} = -\sum_{n=1}^{\infty} n r^{-n-3/2} f_n(t-r)$$

Thus, the leading-order error due to E_1 is proportional to $R^{-5/2}$, and we can write $|E_1 f| < C_1 R^{-5/2}$. In this analysis we have assumed that the wave is normally

incident upon the boundary; skewness in this incidence will lead to further error. For a discussion on the effects of angular dependence on this error, the reader is referred to Engquist and Majda (1977).

The second term in the error bound of $|\hat{E}_1 f|$ is due to the PSE approximation. Recall the derivation of the PSE operator in §3.2. The leading-order error of this approximation is bounded by $C\varepsilon^r |D^\alpha f|$, where $|\alpha| = r + 1$ here. (Note that the symbol r is used to denote the order of accuracy of the PSE approximation here, not the radial coordinate—the meaning should be clear from the context.) Now, the largest magnitude that the derivative $D^\alpha f$ can take with regard to the radially-symmetric form for f considered here is $\partial^{r+1} f / \partial r^{r+1}$. The leading-order behavior of this derivative, applied to the expansion (4.11) at $r = R$, is $R^{-1/2} f_0^{(r+1)}(t - R)$. Thus, the magnitude of $|\hat{E}_1 f|$ is bounded by

$$|\hat{E}_1 f| \leq C_1 R^{-5/2} + C_2 \varepsilon^r R^{-1/2} \tag{4.12}$$

Although the decay of the second term is slower than the first, the proportionality factor of ε^r ensures that its magnitude will be negligibly small. We have not considered the quadrature error here in approximating the PSE integral by a sum, but its effect is similarly negligible compared to the leading-order error in (4.12). Thus, the error of the boundary condition is dominated by the curvature of the boundary, but its magnitude is easily mitigated by increasing the size of the domain.

4.3.3 Testing the condition

The boundary treatment is tested by simulating a radially symmetric pulse of enthalpy of strength 0.1% of the ambient value, offset slightly from the center of the computational domain. For such a weak perturbation the equations of motion would reduce to the linear wave equation for the enthalpy and dilatation since particle velocities are negligible. Nevertheless we use the full compressible equations in order to test the full method. An 8th-order PSE kernel, developed by

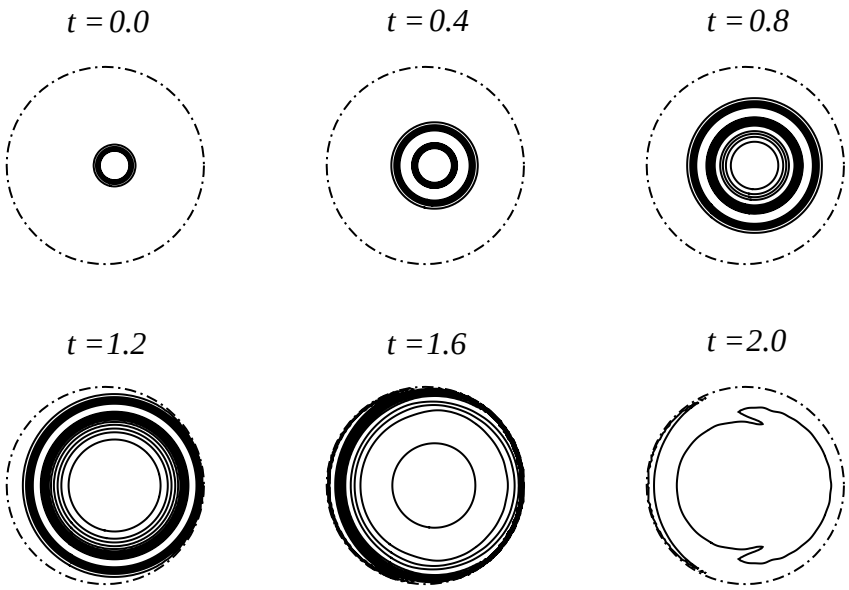

Figure 4.5: Results of simulation of enthalpy pulse. The dotted line represents the boundary of the domain.

the procedure in §3.2,

$$\eta^{\text{lap}}(\mathbf{x}) = \frac{1}{\pi}(40 - 40|\mathbf{x}|^2 + 10|\mathbf{x}|^4 - \frac{2}{3}|\mathbf{x}|^6)e^{-|\mathbf{x}|^2},$$

is used in the interior for the Laplacian; surrounding the domain is a boundary zone with a depth of four particles, enforcing equation (4.10) with the 2nd-order one-sided kernel

$$\eta^{L,(1,0)}(\mathbf{x}) = -\frac{4}{\pi}x_1(5 - 2|\mathbf{x}|^2)e^{-|\mathbf{x}|^2}.$$

The initial distribution of enthalpy is Gaussian with a radius 1/10 the radius of the domain, and 13 particles are distributed across the diameter of the Gaussian. Thus, a total of 13,040 particles are used.

The results of the simulation are depicted in the panels of Figure 4.5. As expected the pulse spreads out in a cylindrical wave that travels at the correct speed

(the times labeled are in acoustic units). The wave front reaches the boundary and passes through it with very little reflection—approximately 2% of the incident wave. This reflection can be reduced by making the domain larger, thus decreasing the radius of curvature of the boundary.

Chapter 5

Computation of acoustic field

The development of the present method has been motivated in part by the desire to compute the sound produced by fluid motion. In principle, we could fill a very large region of space with computational particles and solve the full equations on this set of particles, thereby obtaining both the nearfield dynamics and farfield acoustic radiation simultaneously. The primary difficulty with this proposal is its impracticality. Because the time scales of radiating sound and the fluid fluctuations that generated it are the same, the ratio of their characteristic length scales is on the order of the inverse of the Mach number. Thus, a slightly compressible flow will generate sound of wavelength many times larger than its own breadth. We have not undertaken any effort in this work to design a method that allows particles of variable size, aside from those volume changes effected by fluid dilatation (although this is an obvious source of future work—see Chapter 7). Thus, the method can only *efficiently* capture a very limited portion of the acoustic region.

In the far acoustic field, disturbances are governed by linear equations, which provides for several simplified methods for computing the disturbances outside of the nearfield. The issues associated with these techniques have been discussed at length in a recent review by Lele (1997), who refers to them as "hybrid methods." He categorizes these techniques in order from least to most assumptions as follows:

1. Compressible nonlinear flow solver with linearized Euler solver.

2. Compressible nonlinear flow solver with Kirchhoff surface.

3. Nearly incompressible flow solver with acoustic solver.

4. Compressible flow solver with acoustic analogy.

5. Incompressible flow solver with acoustic analogy.

Technique 1 is the most involved, requiring a numerical solution of the wave equation in the outer wave propagation region. Technique 3 requires a splitting of the governing equations into incompressible and acoustic parts, such as the one proposed by Hardin and Pope (1994), with different solution schemes for each. Lele (1997) discusses some of the delicate issues with this approach that still must be explored. In the present work we will use techniques 2 and 4 in conjunction with the DVPM simulation of a region that contains the nonlinear flow region as well as a limited portion of the linear farfield. For the latter we will use the acoustic analogy developed by Möhring (1978) when the Mach number of the flow allows. We will provide here descriptions of these methods, as well as some discussion of their use in two-dimensional problems.

5.1 Kirchhoff surface

In the farfield, nonlinear interaction terms in the governing equations become negligible and the equations reduce to the linear homogeneous wave equation for the enthalpy (or density, pressure, etc.). Assuming that the particles in a DVPM simulation extend to the region that is considered "acoustic," we can extrapolate the entire acoustic field external to a surface from the limited information available. To do so we construct a surface in the region common to the simulation domain and acoustic region, and through a Green's function formulation develop a formula for the acoustic variable in terms of the surface data.

This Kirchhoff surface methodology has become quite common in aeroacoustic computations. For a review of the use of this method the reader is referred to Lyrintzis (1994). Since most interest in sound generation is in three-dimensional applications, it is difficult to find two-dimensional formulations of the Kirchhoff

method. We present a derivation of the two-dimensional form, as well as a discussion of its numerical implementation, in Appendix C. The result of this derivation is equation (C.7), rewritten here for reference:

$$f(\mathbf{x},t) = \frac{1}{2\pi}\int_{\partial\Omega}\int_0^{t^*} \left\{\left[\frac{1}{c_0}\frac{\partial}{\partial\tau} + \frac{1}{c_0(t-\tau)+|\mathbf{x}-\boldsymbol{\xi}|}\right] f(\boldsymbol{\xi},\tau)(\hat{\mathbf{e}}_R\cdot\mathbf{n}_\xi) - \frac{\partial f}{\partial n_\xi}(\boldsymbol{\xi},\tau)\right\} \times \frac{d\tau\, dS(\boldsymbol{\xi})}{[(t-\tau)^2 - |\mathbf{x}-\boldsymbol{\xi}|^2/c_0^2]^{1/2}}, \quad \mathbf{x}\in\Omega_{\text{far}}, \tag{5.1}$$

where f is some acoustic quantity, $\mathbf{n}_\xi$ is the unit normal at point $\boldsymbol{\xi}$ on the surface $\partial\Omega$, pointing into the acoustic region Ω_{far}, and $\hat{\mathbf{e}}_R$ is the unit vector pointing from the source at $\boldsymbol{\xi}$ to the observation point at $\mathbf{x}$. The time integral is evaluated between $\tau = 0$ and $\tau = t^* \equiv t - |\mathbf{x}-\boldsymbol{\xi}|/c_0$, the retarded time.

It is clear from (5.1) that we only require the values of f and its time and normal derivatives on the surface to compute the sound field anywhere in Ω_{far}, for all $t > |\mathbf{x}-\boldsymbol{\xi}|_{\min}/c_0$. The only restriction is that the simulation domain contains some portion of the region in which f is governed by the linear wave equation, and that all nonlinear portions are contained in the surface. The speed c_0 used is the ambient speed of sound, a_∞. The choice of the variable f is not unique, and in fact can be important to determine where this acoustic region begins. If, for example, the enthalpy is chosen, then the region in which this variable is entirely acoustic is apparently quite distant from the source. Outside of the vortical region, the enthalpy obeys Bernoulli's equation: $h = h_\infty - \frac{1}{2}|\mathbf{u}|^2 - \frac{\partial\chi}{\partial t}$, where χ is the scalar potential consistent with the velocity induced by the vorticity. An asymptotic matching of the near- and farfield solutions reveals that, while an expansion of $\frac{\partial\chi}{\partial t}$ matches with the outer solution term by term, the $\frac{1}{2}|\mathbf{u}|^2$ term has no counterpart in the farfield, yet persists to large distances because it decays like $1/r^2$. A more appropriate acoustic variable—consistent with the discussion in §4.3—is the stagnation enthalpy, $B = h + \frac{1}{2}|\mathbf{u}|^2$. In the irrotational region, $B = B_\infty - \frac{\partial\chi}{\partial t}$, so it satisfies the acoustic equations very close to the vortical region; in the farfield, B, h and the pressure, p, are equal after nondimensionalization.

5.2 Möhring analogy

While most acoustic analogies consist of reinterpretations of the differential equations of motion, Möhring (1978) approached the sound generation process from the Green's function representation of the sound field, using the Powell source term:

$$\begin{aligned} p'(\mathbf{x},t) &= \rho_\infty \int G(\mathbf{x},t|\boldsymbol{\xi},\tau)\nabla_{\boldsymbol{\xi}} \cdot (\boldsymbol{\omega}\times\mathbf{u})\, d\boldsymbol{\xi}\, d\tau \\ &= -\rho_\infty \int \nabla_{\boldsymbol{\xi}} G(\mathbf{x},t|\boldsymbol{\xi},\tau)\cdot(\boldsymbol{\omega}\times\mathbf{u})\, d\boldsymbol{\xi}\, d\tau, \end{aligned}$$

after integration by parts. He argued that this expression can be made linear in the flow quantities by the construction of a vector Green's function, $\mathbf{G}$, that satisfies

$$\nabla_{\boldsymbol{\xi}} G = \nabla_{\boldsymbol{\xi}} \times \mathbf{G}. \tag{5.2}$$

Then, from the inviscid relation for the vorticity, $\frac{\partial \boldsymbol{\omega}}{\partial t} = \nabla\times(\boldsymbol{\omega}\times\mathbf{u})$, we can write, after some manipulation,

$$p' = \rho_\infty \frac{\partial}{\partial t}\int \mathbf{G}(\mathbf{x},t|\boldsymbol{\xi},\tau)\cdot\boldsymbol{\omega}(\boldsymbol{\xi},\tau)\, d\boldsymbol{\xi}\, d\tau. \tag{5.3}$$

The application of this expression bears caveats. The Green's function for the wave operator only satisfies (5.2) when $\mathbf{x}\neq\mathbf{y}$ (i.e., the observation point must be outside of the vortical region), and even then it only satisfies it to lowest order in the Mach number. If, in addition to these conditions, the observation point is far from the flow region, then it can be shown in three-dimensional freespace that the expression reduces to

$$p' = \frac{\rho_\infty}{12\pi a_\infty^2}\frac{x_i x_j}{|\mathbf{x}|^3}\dddot{Q}_{ij}(t-|\mathbf{x}|/a_\infty),$$

where $Q_{ij} = \int(\boldsymbol{\xi}\times\boldsymbol{\omega})_i \xi_j\, d\boldsymbol{\xi}$. This expression is linear in the vorticity and is a clear exposition of the importance of the motion of vortices to farfield sound. The equivalent expression in two dimensions has been developed by Möhring (1979) and by Mitchell, Lele and Moin (1995), the latter using a Fourier transform in

time to assist in the asymptotic matching. It can be written as

$$p' = \frac{\rho_\infty}{4\pi a_\infty^2} \int_{-\infty}^{t-|\mathbf{x}|/a_\infty} \frac{x_i x_j}{|\mathbf{x}|^2} \dddot{Q}_{ij}(\tau) \frac{d\tau}{\sqrt{(t-\tau)^2 - |\mathbf{x}|^2/a_\infty^2}}$$
$$= \frac{\rho_\infty}{8\pi a_\infty^2} \int_{-\infty}^{t-|\mathbf{x}|/a_\infty} \left[\dddot{Q}_1(\tau)\cos(2\theta) + \dddot{Q}_2(\tau)\sin(2\theta)\right] \frac{d\tau}{\sqrt{(t-\tau)^2 - |\mathbf{x}|^2/a_\infty^2}}, \quad (5.4)$$

where $Q_1 = 2\int x_1 x_2 \omega \, dx_1 \, dx_2$ and $Q_2 = \int (x_2^2 - x_1^2)\omega \, dx_1 \, dx_2$. The integral in equation (5.4) is a composition of all of the waves that have reached the observation point by time t. The greatest contribution to the integral comes from τ near $t - |\mathbf{x}|/a_\infty$, which corresponds to the source event whose resultant wave just reaches the observation point at time t. By exploiting both this and the assumption that the observation point is far from the source, the integral can be approximated by

$$p' \approx \frac{\rho_\infty}{8\pi a_\infty^2} \sqrt{\frac{a_\infty}{2|\mathbf{x}|}} \int_{-\infty}^{t-|\mathbf{x}|/a_\infty} \left[\dddot{Q}_1(\tau)\cos(2\theta) + \dddot{Q}_2(\tau)\sin(2\theta)\right] \frac{d\tau}{\sqrt{t-\tau-|\mathbf{x}|/a_\infty}},$$

which exhibits the familar $r^{-1/2}$ spatial decay of cylindrical waves.

Equation (5.4) is integrated numerically by a procedure similar to that used for the Kirchhoff time integral and described in §C.2. The flow is assumed to begin at $t = 0$, so the lower limit of integration is changed accordingly. The vorticity moments are computed with their discrete counterparts,

$$Q_1 \approx 2 \sum_p x_{p,1} x_{p,2} \Gamma_p$$
$$Q_2 \approx \sum_p (x_{p,2}^2 - x_{p,1}^2) \Gamma_p$$

and their third time derivatives are computed with 2nd-order-accurate differencing.

Because of its dependence on the vorticity moments alone, this formula for the acoustic field is often used in conjunction with incompressible vortex method simulations of the nearfield. The approximation of incompressible nearfield flow relies on this region being acoustically compact, which is consistent with the low Mach number assumption used in deriving these formulae.

Chapter 6

Results

In this chapter we present the application of the DVPM to a variety of problems. The first problem is concerned with the treatment of the baroclinic vorticity term in the equations of motion. It exhibits the interaction of a planar expansion wave with an entropy hole, for which an exact solution is permissible. The next two involve the dynamics of vortices in a compressible flow from which sound is emitted. We evaluate the performance of the method by comparing the resulting acoustic field with previous work when available. In another problem, included in Appendix D, the particle method is applied to the one-dimensional Burgers' equation. It demonstrates the ability of the DVPM in the presence of wave steepening and subsequent shock formation.

6.1 Baroclinic generation of vorticity

The following problem exhibits the capabilities of the method when gradients in thermodynamic quantities are integral to the flow. A planar enthalpy expansion wave travels through an entropy depression, or hole, creating vorticity through the baroclinic source term. The resulting vorticity field can be predicted analytically if the wave and hole are sufficiently weak in magnitude. Suppose that the enthalpy has the initial distribution

$$h(x_1, x_2, t) = h_R + \frac{\Delta h}{2}\left[\tanh\left(\frac{x_1 - x_h}{\Delta x_h}\right) - 1\right],$$

and the entropy has

$$s(x_1, x_2, t) = s_\infty + \Delta s \exp\left[-\frac{(x_1 - x_s)^2 + x_2^2}{\sigma_s^2}\right],$$

where $\Delta h > 0$ and $\Delta s < 0$. If both of these quantities are small relative to their ambient values, and the entropy is smaller than the enthalpy $|\Delta s|/|\Delta h| \ll 1$, then the vorticity approximately satisfies

$$\frac{\partial \omega}{\partial t} = \nabla h \times \nabla s,$$

the enthalpy obeys the homogeneous linear wave equation, and the entropy is steady.

The enthalpy wave travels across the hole at a speed much faster than the velocity induced by the resulting counter-rotating vortex pair, whose distribution is given by

$$\begin{aligned}\omega(x_1, x_2, t) &= \Delta s \Delta h \left[\tanh\left(\frac{x_1 - x_h - t}{\Delta x_h}\right) - \tanh\left(\frac{x_1 - x_h}{\Delta x_h}\right)\right] \\ &\quad \times (x_2 - x_s) e^{-(x_1 - x_s)^2 - x_2^2}.\end{aligned}$$

where the variables have been scaled by a_∞ and σ_s. We use values of $\Delta h = 0.01$, $\Delta s = -0.0001$, $\Delta x_h = 0.5$, $x_h = -3.5$ and $x_s = 0$. For the numerical solution we use particles on a square grid of side length $10\sigma_s$, with 25 particles across the entropy hole and a boundary zone at the right (outgoing) boundary with 4 particles' depth, corresponding to a total of 14,637 particles. A time step size of $a_R \Delta t/\sigma_s = 0.01$ is used. The vorticity that results from the simulation is shown in Figures 6.1 (in which the vorticity above the axis of symmetry is positive and that below is negative) and 6.2. The agreement is very good.

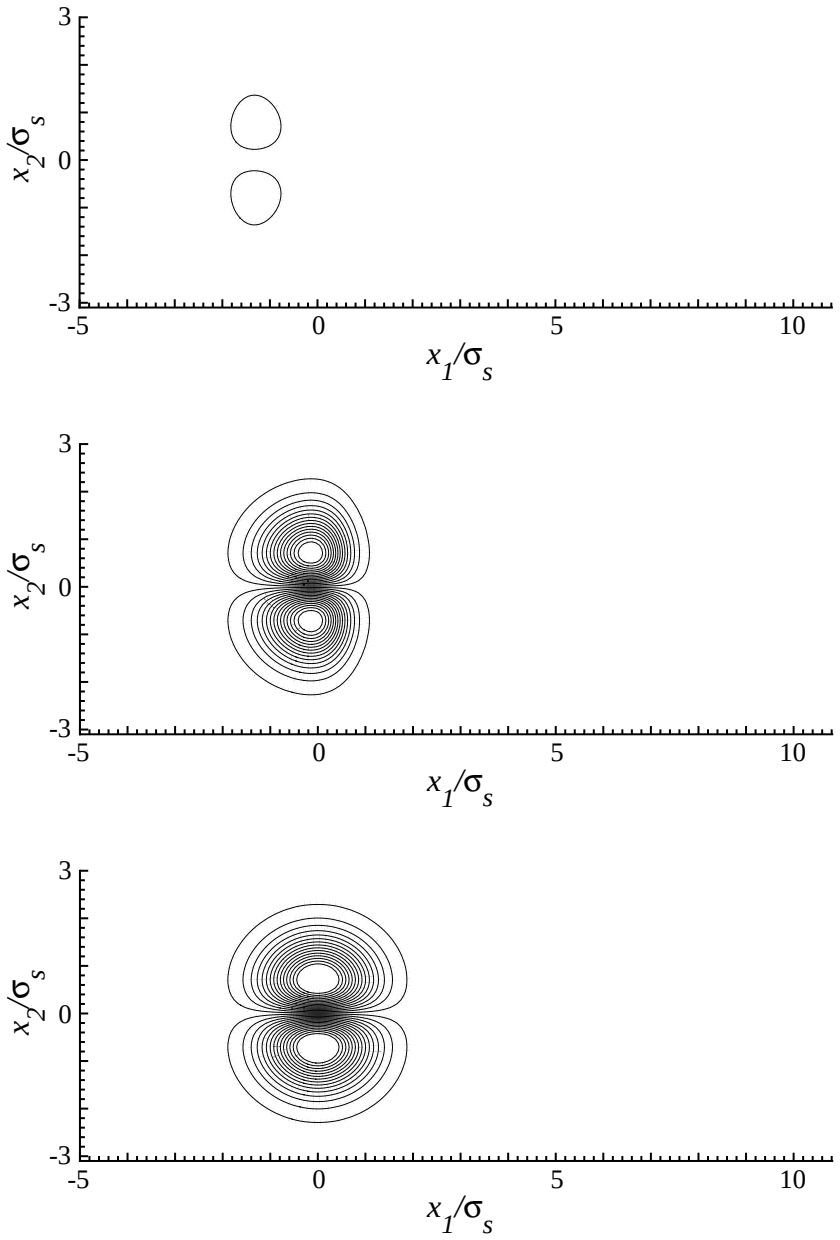

Figure 6.1: Vorticity generated by enthalpy wave/entropy spot interaction, at (a) $a_R t/\sigma_s = 0.2$, (b) 0.4 and (c) 0.6. DVPM: '——'; exact: '– – –'.

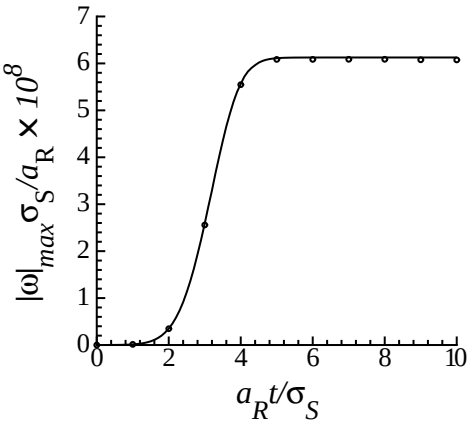

Figure 6.2: Maximum vorticity generated by enthalpy wave/entropy spot interaction as function of time. DVPM: '$\circ$'; exact: '——'.

6.2 Co-rotating vortex pair

The method is now applied to a flow from which sound is produced, a pair of identical vortices in a compressible medium. As the vortices orbit each other they generate sound at a frequency of twice their rotation rate. The problem of sound generation due to point vortices has been explored by several researchers (e.g., Müller and Obermeier, 1967; Yates, 1978; Lee and Koo, 1995; Lyamshev and Skvortsov, 1988). Tang and Ko (1997) used the method of contour dynamics and Möhring's acoustic analogy to explore the sound generation due to finite-cored vortices with constant vorticity. Mitchell, Lele and Moin (1995) simulated both the nearfield behavior of Gaussian-distributed vortices and their acoustic field using a compact finite-difference method on a stretched grid.

The initial configuration of the vortices in the present case is depicted in Figure 6.3. All quantities are scaled by the initial half-spacing between the vortices, R, and a characteristic speed of sound, a_∞. For comparison with Mitchell et al. (1995), each vortex is Gaussian-distributed according to

$$\omega = \frac{1.25\Gamma_0}{\pi r_0^2} e^{-1.25r^2/r_0^2} \tag{6.1}$$

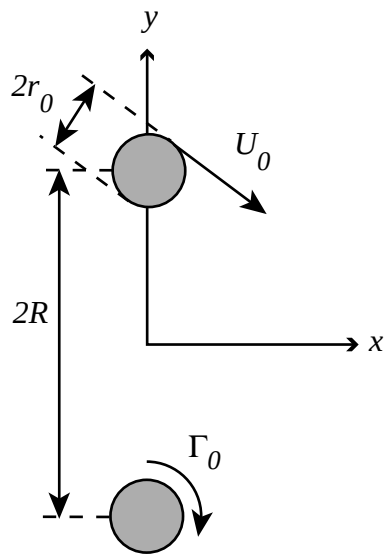

Figure 6.3: Initial configuration of vortex pair.

where the circulation and radius of each vortex are $\Gamma_0 = -2\pi(0.7)^{-1}M_0 r_0$ and $r_0 = 0.15$, respectively. The circulation Reynolds number, $Re \equiv |\Gamma_0|/\nu$ is 7500, the vortex Mach number, $M_0 \equiv U_0/a_\infty$ (where U_0 is the maximum azimuthal velocity of a single Gaussian vortex) is 0.56, and the Prandtl number is 0.7. With these flow parameters, the initial rotation time is $\tau = 105$ and the wavelength of sound is $\lambda = 52.5$. The co-rotation Mach number is $M_r = 0.7M_0 r_0 = 0.06$. Such a large separation in the acoustic and flow length scales qualifies the vortices as a compact source, which makes efficient resolution of the problem difficult. Instead of attempting to capture both the near- and farfield simultaneously, the present investigation focused on the nearfield dynamics only. The method is capable of computing both, but without particles of variable size it cannot compute both regions practically.

Initially, the flow is taken as homentropic and dilatation-free. The initial enthalpy is deduced from a solution of the Poisson equation (2.18), which is solved with the same Green's function approach used to invert the potential equations (2.2). The particles are distributed on a Cartesian grid inside a circular domain of

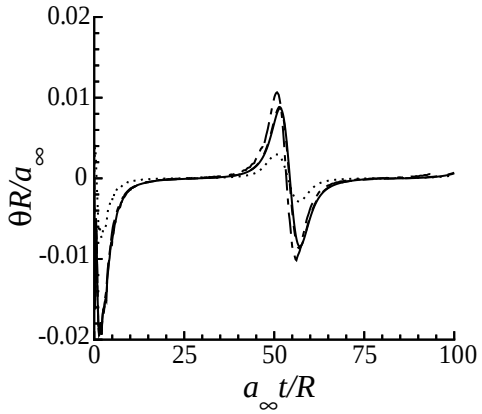

Figure 6.4: Dilatation at $(x, y) = (0, 1.2)$ for co-rotating vortex pair. $N_{core} = 10$:'$\cdots\cdots$', 13: '—·—·—', 20:'– – –', 40:'——'.

radius R_Ω with N_{core} particles laid across the diameter of each vortex; a boundary zone with a depth of 4 particles surrounds the domain. The particles are remapped to the same Cartesian grid every n_{rm} time steps. A fourth-order Runge-Kutta scheme is used for time advancement with a time-step size of $\Delta t = 0.009$. The blob radius and inter-particle spacing are related by $\varepsilon = \Delta x^{0.85}$. All of the kernels used in the interior are 8th order accurate, except for the one-sided boundary kernel, which is 2nd order accurate:

Blob function:	$\zeta(\mathbf{x}) = \frac{1}{\pi}(4 - 6\|\mathbf{x}\|^2 + 2\|\mathbf{x}\|^4 - \frac{1}{6}\|\mathbf{x}\|^6)e^{-\|\mathbf{x}\|^2}$
Laplacian:	$\eta(\mathbf{x}) = \frac{1}{\pi}(40 - 40\|\mathbf{x}\|^2 + 10\|\mathbf{x}\|^4 - \frac{2}{3}\|\mathbf{x}\|^6)e^{-\|\mathbf{x}\|^2}$
First derivative wrt x_i:	$\eta(\mathbf{x}) = \frac{x_i}{\pi}(-20 + 20\|\mathbf{x}\|^2 - 5\|\mathbf{x}\|^4 + \frac{1}{3}\|\mathbf{x}\|^6)e^{-\|\mathbf{x}\|^2}$
Bndry first deriv. wrt x_i:	$\eta^L(\mathbf{x}) = \frac{x_i}{\pi}(-20 + 8\|\mathbf{x}\|^2)e^{-\|\mathbf{x}\|^2}$

To verify that the method converges as the particle coverage is refined, we computed the problem on a domain of radius $R_\Omega = 2.5$ and let $N_{core} = 10$, 13, 20 and 40. The resulting dilatation field at a point $(x, y) = (0, 1.2)$, shown in Figure 6.4, converges as the particle spacing is halved twice.

The results of the vorticity and dilatation fields from a computation with

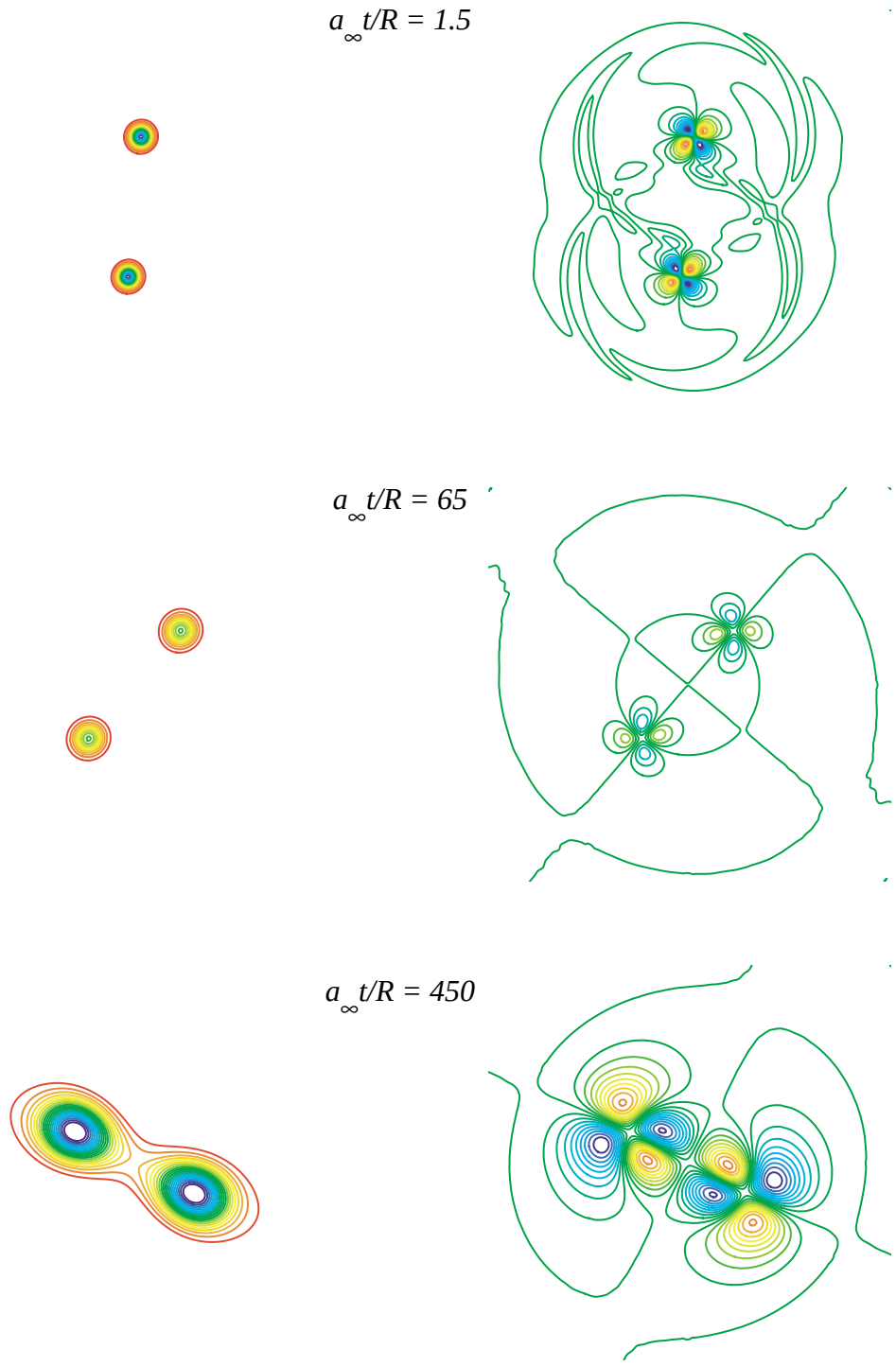

Figure 6.5: Vorticity (left) and dilatation (right) in co-rotating vortex pair.

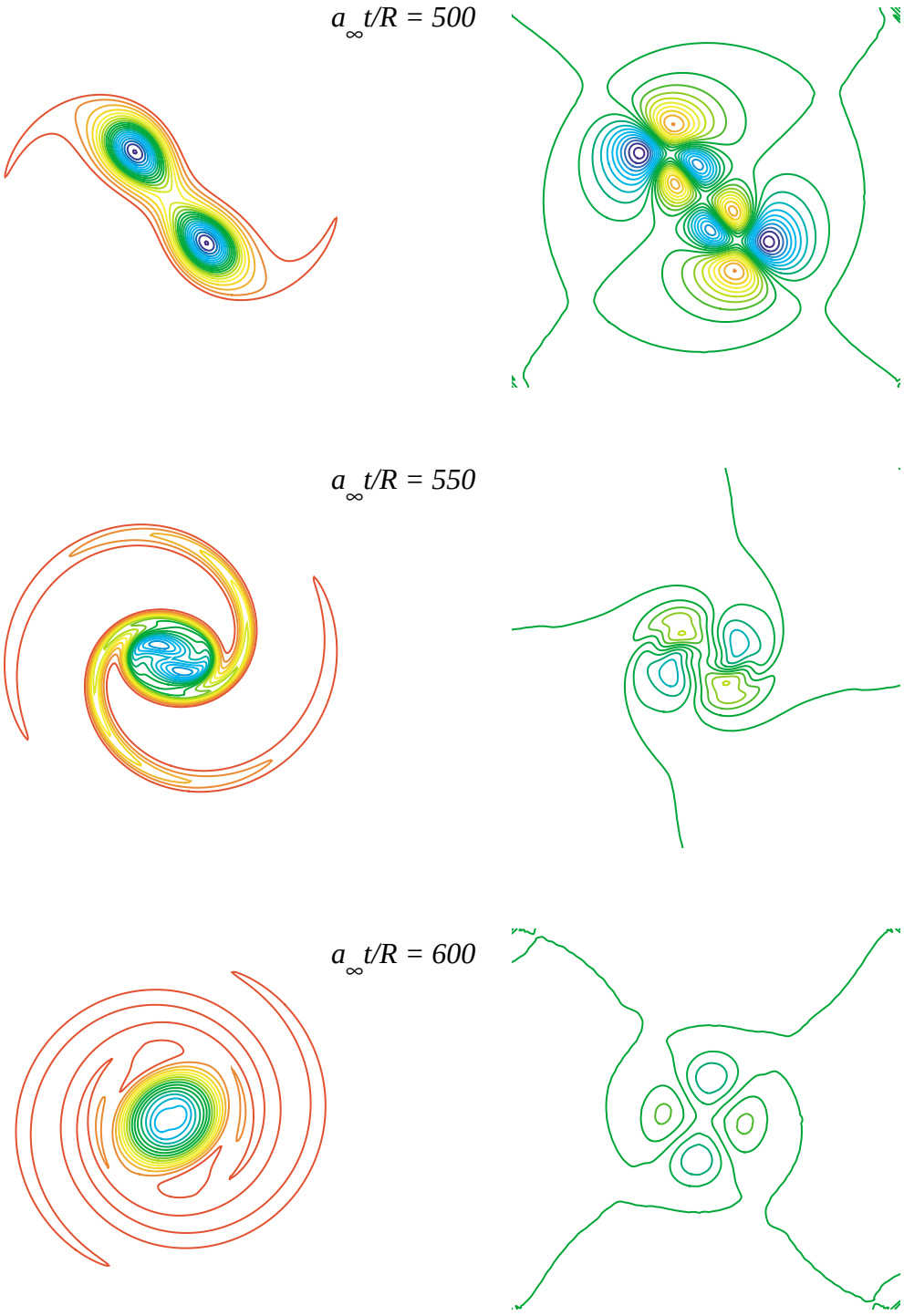

Figure 6.5: Vorticity and dilatation in co-rotating vortex problem (cont'd).

$N_{core} = 13$, $R_\Omega = 4$ (corresponding to about $83,500$ particles), and $n_{rm} = 2$ are depicted in the series of panels of Figure 6.5. Red contours denote positive values and blue denote negative. The contour levels are as follows: for the first two time levels, the vorticity levels are in the range $[-23, -1]$ in increments of $\Delta\omega = 1$ and the dilatation levels are in $[-0.06, 0.06]$ in increments of $\Delta\theta = 0.006$; the remaining four time levels have vorticity contours in $[-2, -0.05]$ in increments of $\Delta\omega = 0.103$ and dilatation contours in $[-0.005, 0.005]$ in increments of $\Delta\theta = 0.0005$. The first row of panels shows the fields soon after the initialization. An acoustic transient is emitted from each core as the dilatation settles to the correct value; the transient is not strong and exits the domain without significant reflection. A quadrupole structure is observed in the dilatation in the next row of panels. The same structure was observed by Mitchell et al. (1995), as well as by Yates (1978) in his Bernoulli enthalpy, a quantity that is closely related to the dilatation. The configurations of both fields persist for several rotations, though both quantities are diffused by viscosity over this duration, as observed in the third set of panels (in which the contour levels have been adjusted for better resolution of the diffused magnitudes). After approximately four rotations the continual effects of viscosity and compressibility force the cores to merge, depicted in the final three rows of panels. The resulting dilatation field is a much weaker quadrupole centered at the core of the new elliptical vortex. Further computation, not shown, reveals the axisymmetrization of the core and thus the disappearance of the dilatation.

The conservation properties of the DVPM are demonstrated by plotting the total mass and circulation in the domain versus time in Figures 6.6(a) and 6.6(b). The total mass of the particles rises by less than 0.02% and the total circulation decays by less than 1%. The deviations are due wholly to the fact that the interpolation kernel we have chosen does not exactly conserve the zeroth moment of interpolated quantities, as discussed above. The change in circulation is more dramatic than the change in mass. Since only the difference in a particle's density from the ambient value is interpolated, and $|\Delta\rho|/\rho_\infty$ is small, the mass is less affected by the interpolation error. Neither quantity changes enough to significantly

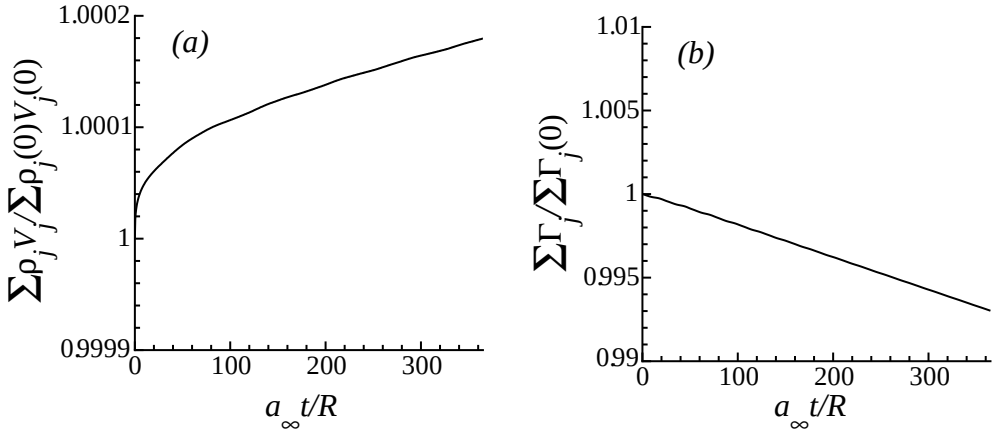

Figure 6.6: Histories of the total mass and circulation of the particles.

affect the results.

A circular Kirchhoff surface of radius $R_s = 3.5$ is constructed to surround the vortical region; at this radius it is sufficiently removed from the edge of the computational domain to avoid corruption from the boundary treatment. The stagnation enthalpy of each particle is computed from the results of the DVPM simulation and the particle data is interpolated onto the surface control points. The time derivative is computed from backward differencing and the normal derivative from a PSE calculation.

The resulting pressure fluctuations—equal to the stagnation enthalpy after non-dimensionalizing—observed at one half-wavelength from the origin (on the y-axis) are depicted in Figure 6.7. Note that because of the symmetry of the problem each rotation of the vortices corresponds to two wavelengths of sound. The magnitude and phase of the pressure agree quite well for the first two rotations. The large spike in the data of Mitchell et al. (1995) at the outset is due to the acoustic transient. Such a spike is not exhibited in the present results because the initial transient period is ignored in the Kirchhoff calculation.

After a little more than three rotations, the vortices of Mitchell et al. (1995) merge, reflected by a small rise and then quick decay of the pressure. Merger in the

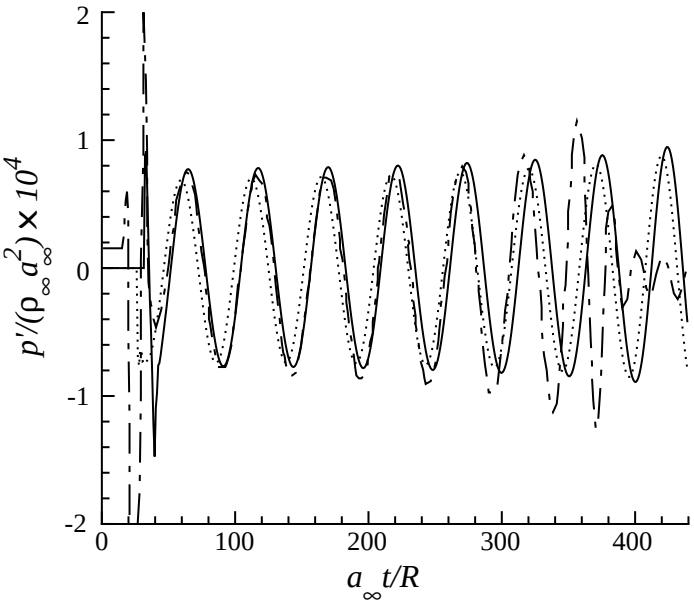

Figure 6.7: Pressure fluctuations observed at $(x, y) = (0, \frac{1}{2}\lambda)$ from co-rotating vortex pair. Mitchell et al. (1995): '–·–'; DVPM and Kirchhoff surface at $R_s = 3.5$: '——'; DVPM and Möhring analogy: '· · · · · · '.

present simulation is delayed by an extra one-and-a-half rotations, as the results in Figure 6.5 show. As demonstrated by Melander, Zabusky and McWilliams (1988), vortex merger is a convective phenomenon that occurs between two vortices initially separated by less than a critical distance—in the case of Gaussian vortices, $R/r_0 < 1.49$. More precisely, in their theory, merger is parametrized by a constant value, σ, defined as

$$\sigma \equiv \frac{2\pi M}{\Gamma_0 A},$$

where M is the angular impulse and A is the area of each vortex. Merger occurs if σ is less than some critical value, σ_{cr}. Their approach to determining this critical value is based on a low-order moment model of the Euler equations.

Melander et al. (1988) amended their moment model to include the role of

dissipation. In viscous flow, M increases linearly in time according to the Poincaré identity,

$$\dot{M} = 4\nu\Gamma,$$

where Γ is the constant total circulation and ν is the viscosity. However, the area of each vortex also increases on a viscous timescale, and in the balance σ decreases with time. While σ is larger than some threshold (approximately equal to σ_{cr}), the vortices continue to co-rotate in a "metastable" state, but eventually σ will fall below this threshold and convective merger will occur.

The time at which σ crosses this threshold can be quite sensitive to small discrepancies in its decay, as a simple illustration will reveal. For a general distribution of vorticity, we may define A as the area surrounding a vortex whose contained circulation is some fraction, α, of the total circulation of the vortex. While it is difficult to compute this quantity in general, for a single viscous vortex we can show that it leads to $A(t) = 4\nu t \log(1/(1-\alpha))$. Thus, σ is constant for a single vortex. For a pair of vortices, we should not expect the area of each vortex to increase significantly faster than linearly (because its behavior should not differ significantly from the single vortex, but σ *will* decrease), and thus the decay of σ will be quite slow. For the purposes of illustration, consider a power law behavior for A, $A \propto t^{1+\epsilon}$, where $\epsilon \ll 1$. Thus, $\sigma \propto t^{-\epsilon}$. A slight discrepancy in the value of ϵ between two simulations can lead to a much larger discrepancy in the time at which σ crosses a given threshold. It is difficult to assess which simulation predicts the more accurate merger time, but this is probably not as important as predicting the qualitative behavior of merger.

The compactness of the vortical flow region allows the use of one of several acoustic analogies for computing the farfield sound. For completeness we include the results from the Möhring formula, equation (5.4), in Figure 6.7. The results agree favorably with the Kirchhoff results and those of Mitchell et al. (1995).

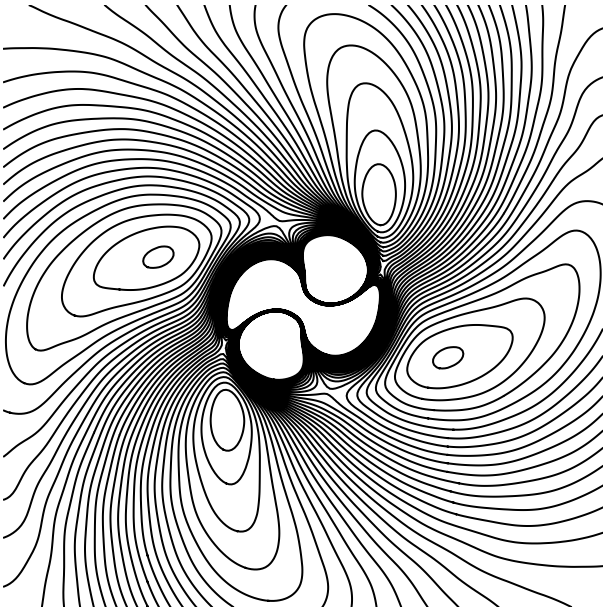

Figure 6.8: Dilatation field at $a_\infty t/R = 81$ for a noncompact vortex pair. The contours are saturated for clarity of the outer dilatation field.

6.2.1 Noncompact flow field

The difficult task of capturing both the nearfield dynamics and the farfield acoustics is alleviated when the acoustic wavelength is not so large compared to the extent of the vortical region. As a further demonstration of the capabilities of the DVPM, the same problem was simulated with larger vortex cores, $r_0 = 0.45$, which corresponds to a wavelength of $\lambda = 17.5$. Larger cores with the same particle resolution permit a larger region to be covered by the same number of particles. The computational domain was thus enlarged to a radius $R_\Omega = 12$. The resulting dilatation field at $t = 81$ is depicted in Figure 6.8. The contour levels are distributed evenly in the range $[-0.0025, 0.0025]$ in increments of $\Delta\theta = 1.67 \times 10^{-4}$, saturated to elucidate the outer dilatation. At the time shown, the vortices are merging. It is interesting to note that Mitchell et al. (1995) did not observe merger after five

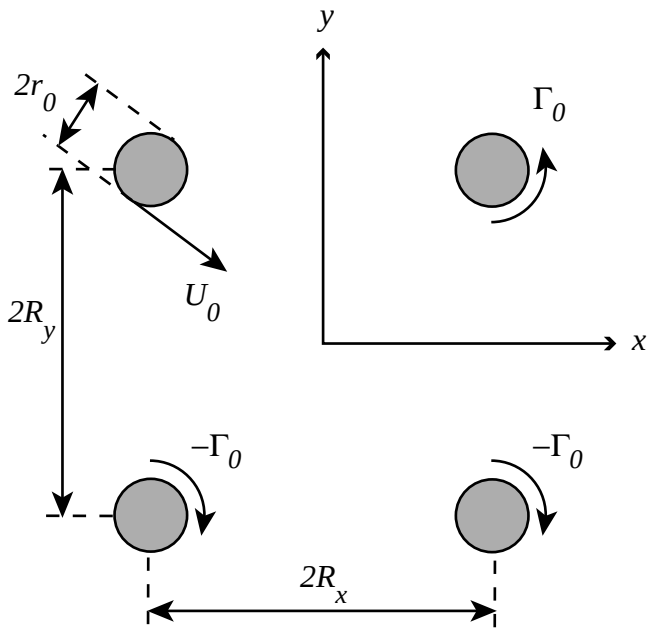

Figure 6.9: Initial configuration of leapfrogging vortices.

full rotations, or 175 units of time, using vortices of the same size but with a much larger Reynolds number. The counterclockwise tilting of the dilatation structure in the outer regions is due to the phase lag of compressibility.

6.3 Leapfrogging vortices

We demonstrate here the application of the DVPM to the slightly more complex problem of two vortex pairs with symmetry about the x-axis. The initial configuration is depicted in the schematic of Figure 6.9. Two counterclockwise-rotating vortices with circulation Γ_0 are placed at $(x, y) = (\pm R_x, R_y)$, and two identical, clockwise-rotating vortices are situated at the image locations $(x, y) = (\pm R_x, -R_y)$. In this configuration the vortex pairs "leapfrog," similar to the mutual threading of two same-sense vortex rings in three dimensions (see, e.g., Lamb (1932); Shariff and Leonard (1992) and references therein). A vortex and its image advect each other in the positive x direction, but simultaneously the vortices of

same sign induce motion in the y direction. Consequently, the rear vortex-image system draws closer together, increasing its mutual advection speed in the x direction, while the forward system is pulled away from the x-axis, thus decreasing its forward speed. The two systems thus swap positions as they both propagate forward at a steady mean velocity, and the motion repeats periodically. Such a configuration can be regarded as a model for the pairing of vortices in a two-dimensional jet, or, alternatively, for the behavior of a co-rotating pair near a plane wall. The sound field from four point vortices in this configuration, with the restriction that $R_y/R_x > 3$, has been explored by Stüber (1970), and the sound sources from finite-sized vortices with constant vorticity, at several values of R_y/R_x, were investigated by Tang and Ko (2000) using the method of contour dynamics and Möhring's analogy.

We present the results for three cases. In each, we set $R_x = R_y = R$ and scale all variables by this length; the distribution of the vorticity in each vortex is given by (6.1). We vary the thickness of the vortex core, r_0, but maintain the same circulation by changing the Mach number so that the product $M_0 r_0$ is constant. The Prandtl number is still 0.7 and the circulation Reynolds number is 10^5. We set $R_\Omega = 4$ and $\Delta t = 0.009$. The ratio of the blob radius to the inter-particle spacing is $\varepsilon/\Delta x = 1.45$, and the particles are remeshed every $n_{rm} = 5$ steps. The same blob functions and PSE kernels are used in this example as in the co-rotating pair. Clearly, the forward motion of the vortex system is not a problem for a Lagrangian numerical method. However, in the interest of capturing the acoustic field without the complexity of a moving Kirchhoff surface, we subtract a uniform velocity from each particle to cancel the mean motion. For this mean speed we numerically compute the motion of four point vortices of the same strength and initial configuration, from which the result is $U_{avg} = 0.108$. Using this same point vortex model, we calculate the period of the leapfrogging motion to be $\tau = 72.3$.

6.3.1 Case 1: $r_0 = 0.15$, $M_0 = 0.56$

In the first case we set $r_0 = 0.15$ and $M_0 = 0.56$. We place 13 particles across the core of each vortex, corresponding to around $83,500$ total particles, as in the previous example. The resulting vorticity and dilatation of the DVPM simulation are depicted in the panels of Figure 6.10. The contour levels of the vorticity are distributed in increments of $\Delta\omega = 0.552$ in the range $[-8, 8]$, and those of the dilatation in $[-0.1, 0.1]$ in increments of $\Delta\theta = 0.00690$. Once again, the dilatation exhibits the initial transient wave. The quadrupole structure seen in the last example is also apparent in the vortex cores here, but its shape and strength change as the relative position of the vortex varies through the cycle. As the diameter of a vortex-image pair decreases, its dilatation grows and reaches a maximum at its most contracted stage. The dilatation weakens as the pair expands and is at its minimum as the other pair passes through it. Because of the symmetry of the pairs, all of this behavior is exhibited in only half of a cycle. Due to some numerical effects discussed below, the period of the present example, $\tau \approx 75.6$, is slightly longer than for the point vortices.

Among the second moments of vorticity used for Möhring's analogy, only Q_1 is nonzero because of the symmetry of the problem. Its third time derivative, the sound "source" according to Möhring's theory, is plotted in Figure 6.11(a) from both the DVPM simulation and the point vortices. For both sets of results, $\dddot{Q}_1$ reflects the unsteady motion of each vortex during its period of revolution, quite different from the steady rotation of two vortices in the previous example. The quantity exhibits alternating intervals of zero magnitude—corresponding to the vortices situated at the corners of a square—followed by a small decay, sharp peak, and small rise—corresponding to the passage of one pair through the other. It is clear that the sound generated by these vortices is largely due to their motion during a relatively short, but active, interval.

Through one-half rotation, there is excellent agreement between the results. After three-quarters of a rotation, the period of the DVPM result begins to increase, and its peak value exhibits a slight decay. The DVPM results also develop

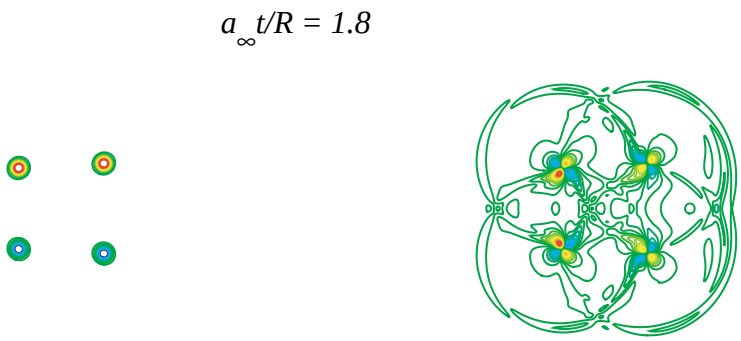

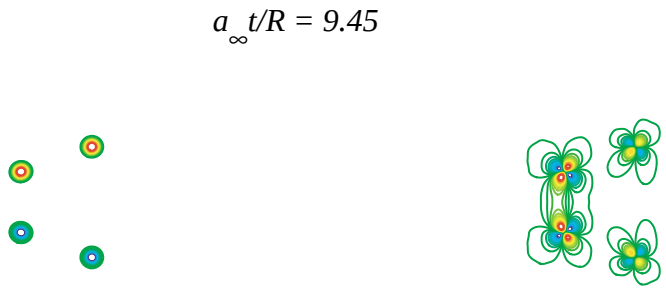

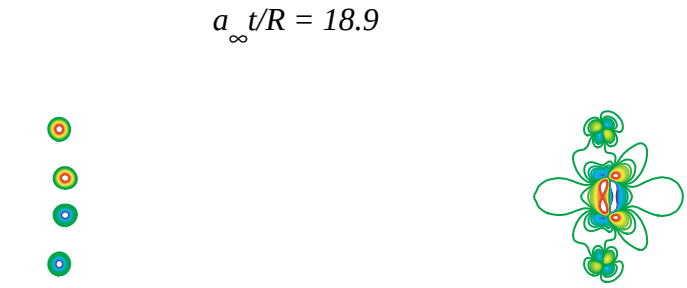

Figure 6.10: Vorticity (left) and dilatation (right) in $r_0 = 0.15$, $M_0 = 0.56$ leapfrogging vortices problem.

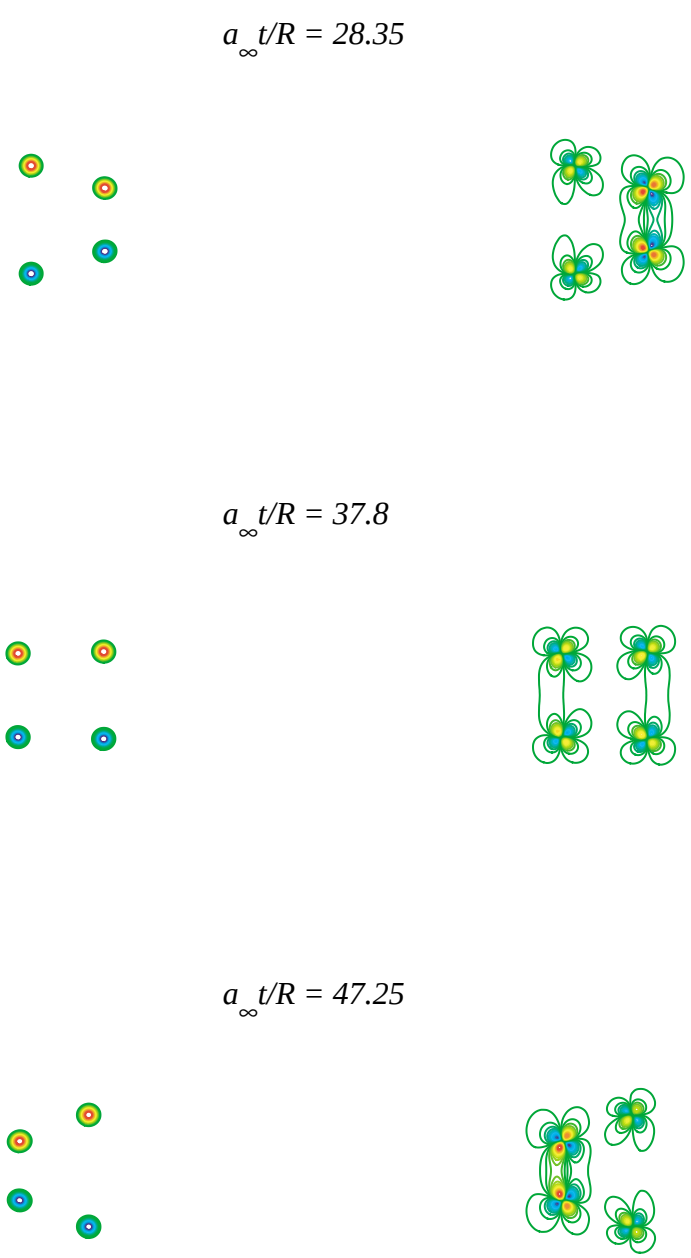

Figure 6.10: Vorticity and dilatation in $r_0 = 0.15$, $M_0 = 0.56$ leapfrogging vortices problem (cont'd).

$a_\infty t/R = 56.7$

$a_\infty t/R = 66.15$

$a_\infty t/R = 75.6 \approx a_\infty \tau/R$

Figure 6.10: Vorticity and dilatation in $r_0 = 0.15$, $M_0 = 0.56$ leapfrogging vortices problem (cont'd).

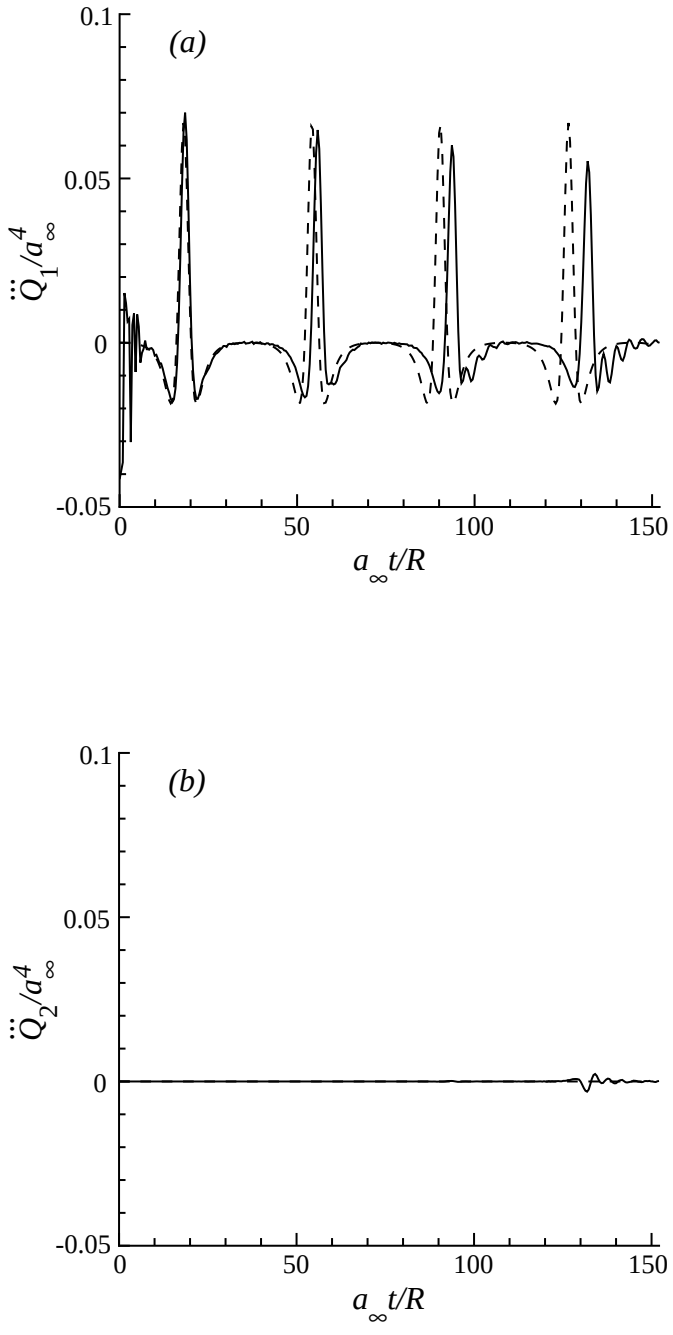

Figure 6.11: (a) $\dddot{Q}_1$ and (b) $\dddot{Q}_2$ source terms from DVPM: '——'; and point vortex model: '– – –'.

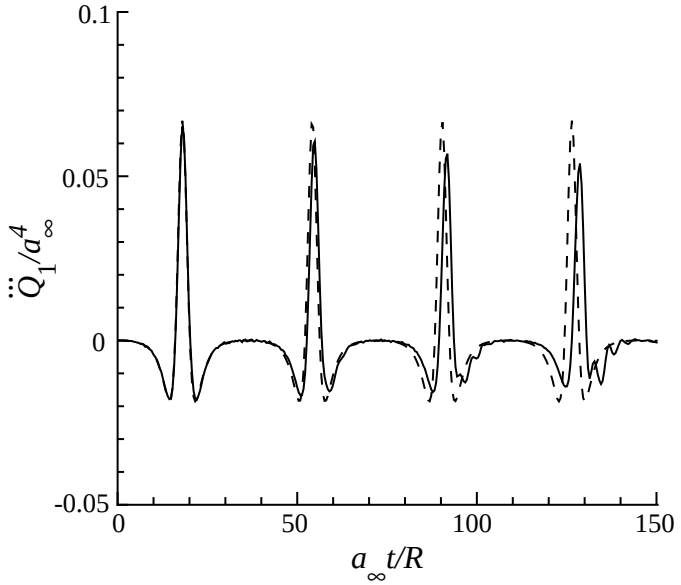

Figure 6.12: $\dddot{Q}_1$ source term from incompressible VPM: '——'; and point vortex model: '– – –'.

small oscillations during the "quiet" portions of the rotation. The latter behavior is due to finite-sized core effects. As the vortices rotate, their cores deform and subsequently nutate. Tang and Ko (2000) have shown that core deformation results in oscillations in the source terms. The period increase is partly due to compressibility effects and partly to finite-core effects. Figure 6.12 depicts the same quantity, but now with a comparison between the results from an incompressible VPM simulation (using the same flow parameters and resolution) and the point vortex model. The increase in period is still apparent, but is smaller now. There is also still a decay in magnitude. Both of these phenomena are now attributable to the effects of a finite-sized core, as core deformation draws some energy away from the rotational motion. As a check of the symmetry of the DVPM simulation, the third time derivative of Q_2 is depicted in Figure 6.11(b). At later times, the presence of some small fluctuations suggests that symmetry is not strictly maintained, but its breaking is not significant enough to affect the sound field.

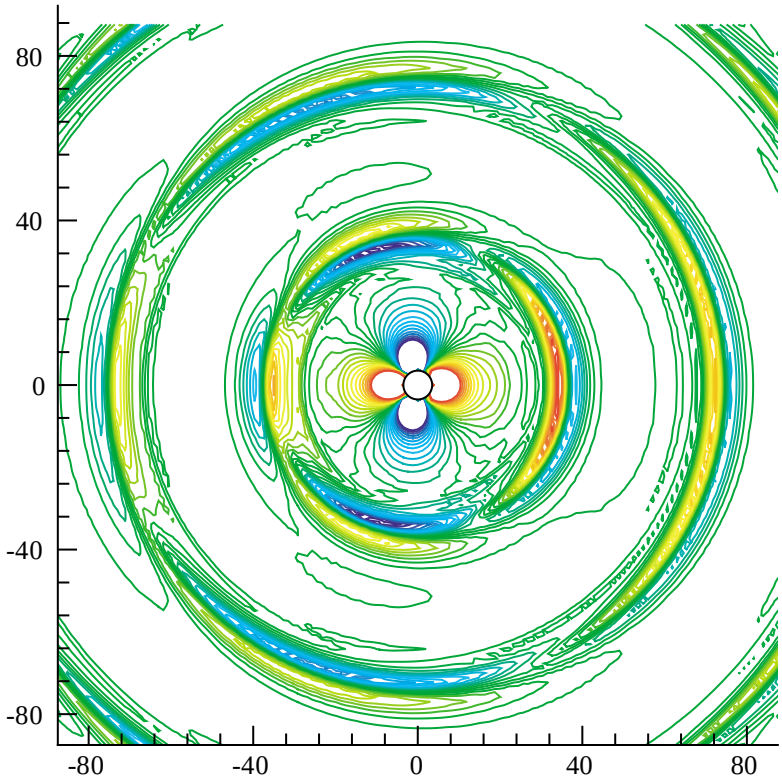

Figure 6.13: Pressure field from $r = 0.15$, $M_0 = 0.56$ leapfrogging vortices at $a_\infty t/R = 130$. The Kirchhoff surface is shown as a circle centered at the origin.

The sound radiated by this process is computed using a Kirchhoff surface at $R_s = 3.5$. The acoustic field at $t = 130$ is shown in Figure 6.13, with the Kirchhoff surface depicted by a circle at the origin. Note that the observation points are moving in the same frame as the vortex system. The acoustic formulae could be amended to account for the effects of a moving source, but the Mach number of forward motion is only 0.108 and thus Döppler effects are quite small. The acoustic nearfield exhibits a quadrupole structure, which translates into a cylindrical wave pattern in the farfield. These cylindrical waves are approximately divided into four quadrants: two above and below the vortex system, and two ahead and behind it. They do not possess a fore/aft symmetry. The quadrant ahead of the system comprises a larger sector of the circle than the one behind. This directivity is due

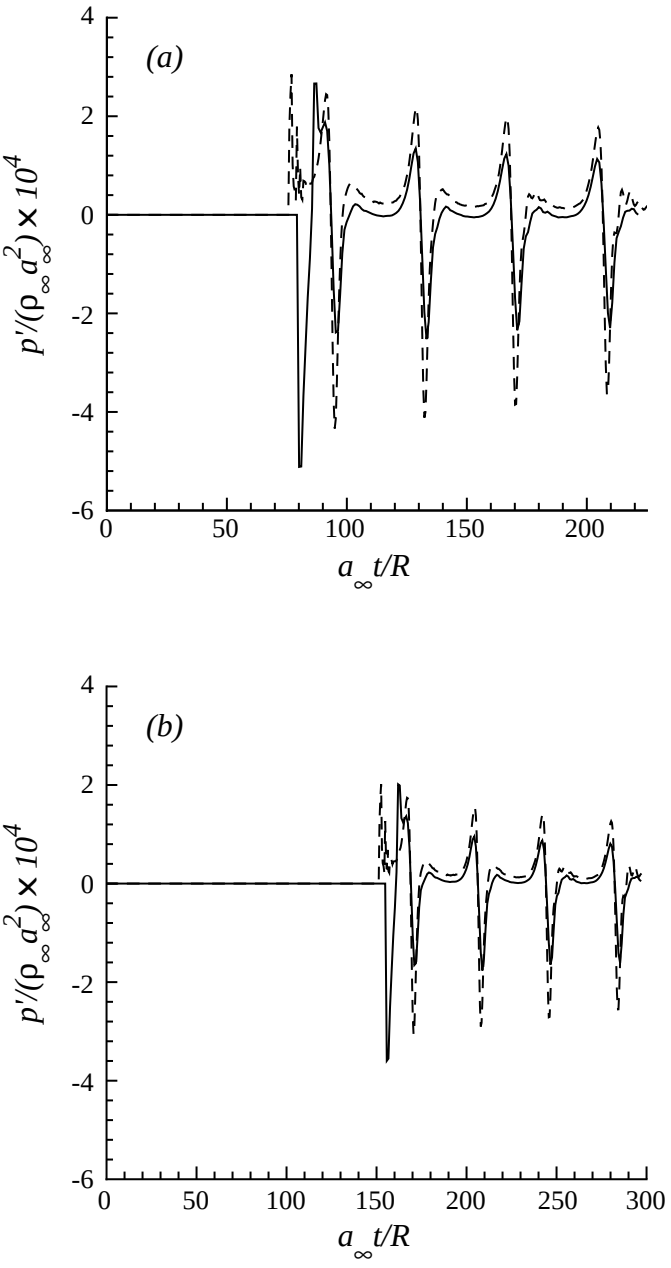

Figure 6.14: Pressure fluctuations from $r = 0.15$, $M_0 = 0.56$ leapfrogging vortices. (a) At $(r, \theta) = (2\lambda, 90°)$, and (b) at $(r, \theta) = (4\lambda, 90°)$. DVPM and Kirchhoff surface at $R_s = 3.5$: '——'; DVPM and Möhring analogy: '– – –'.

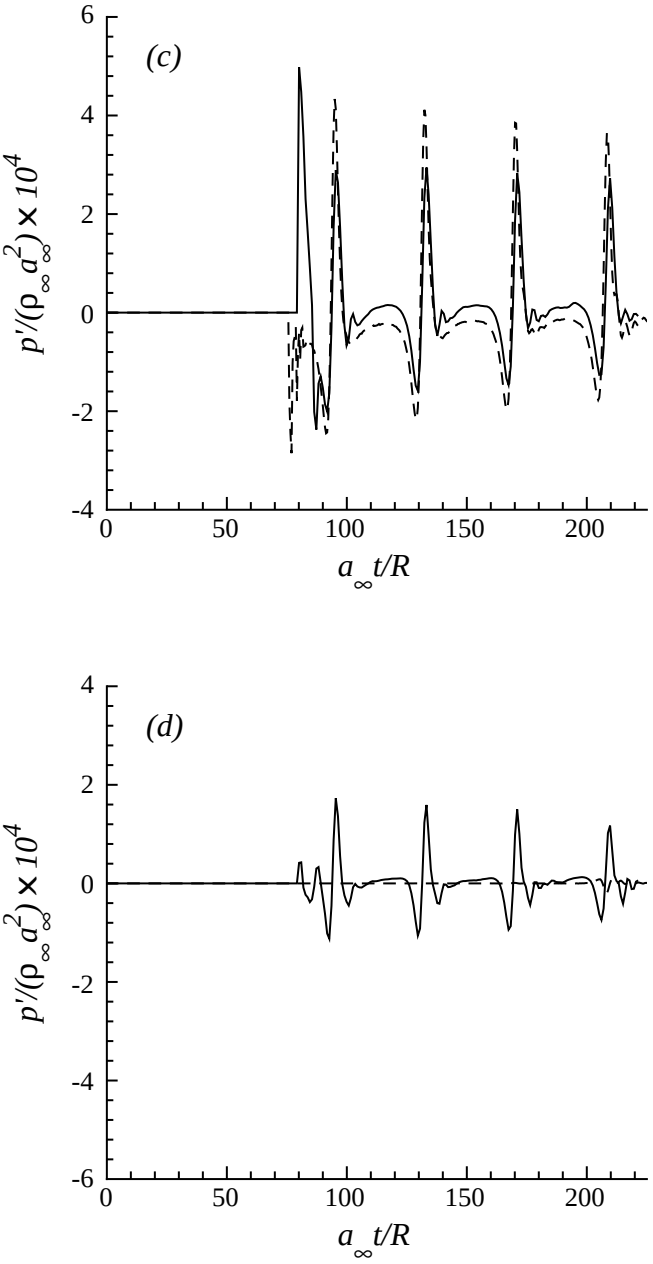

Figure 6.14: Pressure fluctuations from $r = 0.15$, $M_0 = 0.56$ leapfrogging vortices (cont'd). (c) At $(r, \theta) = (2\lambda, 0°)$, and (d) at $(r, \theta) = (2\lambda, 45°)$.

to a slight rearward shifting of the nearfield quadrupole by the dipole velocity field of the vortices.

The results from the integration of $\dddot{Q}_1$ of the DVPM through equation (5.4) are shown with the results of the DVPM/Kirchhoff surface simulation in the series of plots of Figure 6.14. It is difficult to assess *a priori* whether this vortex configuration is acoustically compact. However, Yates (1978) argues that for a co-rotating pair, noncompactness effects—most notably, the diminishing of the radiated power—arise when the co-rotation Mach number is larger than 0.1, or the acoustic wavelength is less than 30 times the radius of the pair. In the present example, the acoustic wavelength is half of the period of rotation, or approximately $\lambda = 37.8$. Thus, it is possible that compactness is not strictly obeyed. Noncompactness would become manifest in the overprediction of the sound field by Möhring's analogy, as found by Mitchell et al. (1995).

In Figure 6.14(a), the sound measured at $\theta = 90°$ (relative to the direction of motion of the vortices) and a distance of $r = 2\lambda$ is shown. As expected, the sound peaks reflect the delayed response to the sudden passage of one vortex pair through the other. The sound field computed from the Möhring formula agrees reasonably well with the Kirchhoff result. The DVPM/Möhring sound peaks are slightly stronger, likely due to the noncompactness effects discussed above. There is also some disagreement in the sound levels predicted between peaks, although this discrepancy is smaller at 4 wavelengths, as shown in Figure 6.14(b), so it is probably due to the assumption of Möhring's formula that the observation point is far from the source region.

Satisfactory agreement between the DVPM and point vortex results is also apparent in Figure 6.14(c), at $r = 2\lambda$ and $\theta = 0°$. The agreement fails, however, for the final observation point at $r = 2\lambda$ and $\theta = 45°$, depicted in Figure 6.14(d). As the presence of the factor $\cos(2\theta)$ indicates in (5.4), Möhring's analogy predicts fore-aft symmetry and lines of extinction along the diagonal axes. Even if the rearward shifting of the sound field is accounted for, Figure 6.13 indicates that the lines dividing the quadrants have lower, but nonzero sound levels. The lines

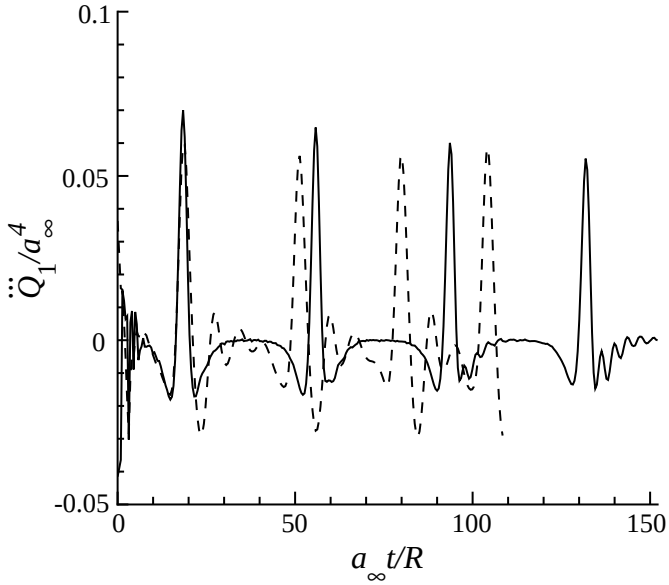

Figure 6.15: $\dddot{Q}_1$ from $r_0 = 0.15$, $M_0 = 0.56$: '——'; and $r_0 = 0.30$, $M_0 = 0.28$: '– – –'.

of extinction predicted along these diagonal axes are due to the retention of only the leading-order quadrupole term in the derivation of (5.4). The inclusion of higher-order terms would likely result in comparable sound levels.

6.3.2 Case 2: $r_0 = 0.3$, $M_0 = 0.28$

In the next case the radius of the cores is doubled to $r_0 = 0.3$ and the vortex Mach number halved to preserve the circulation. The same number of particles is used, in the same computational domain, corresponding to $N_{core} = 25$. The value of $\dddot{Q}_1$ is plotted in Figure 6.15 with the result from the previous case. In contrast with that case, the peaks are becoming more frequent as time progresses, suggesting that the vortices in each co-rotating pair are approaching each other and each pair's rotation is accelerating. Also, the fluctuations between peaks are greater, due to larger deformation of the vortex cores.

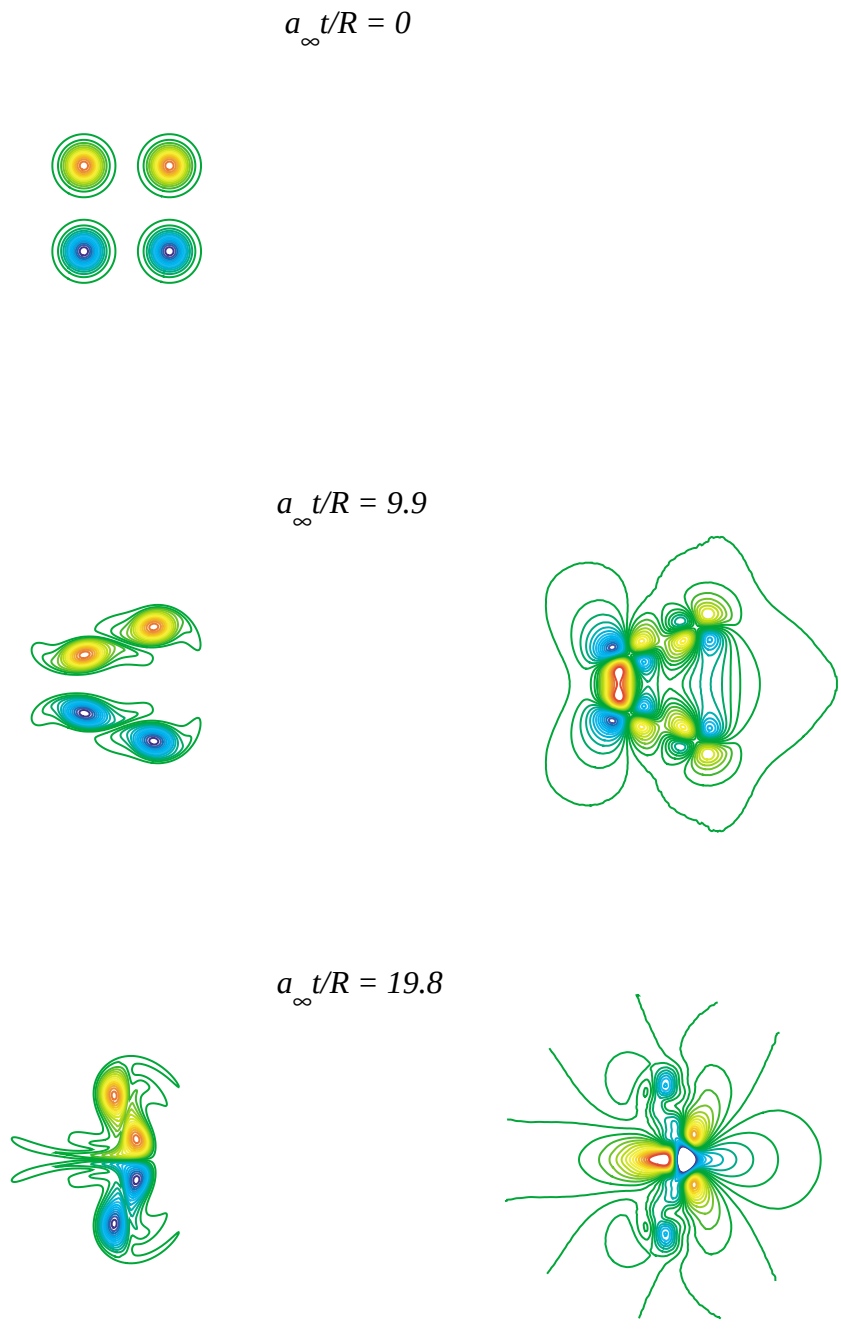

Figure 6.16: Vorticity (left) and dilatation (right) in $r_0 = 0.45$, $M_0 = 0.1867$ leapfrogging vortices problem.

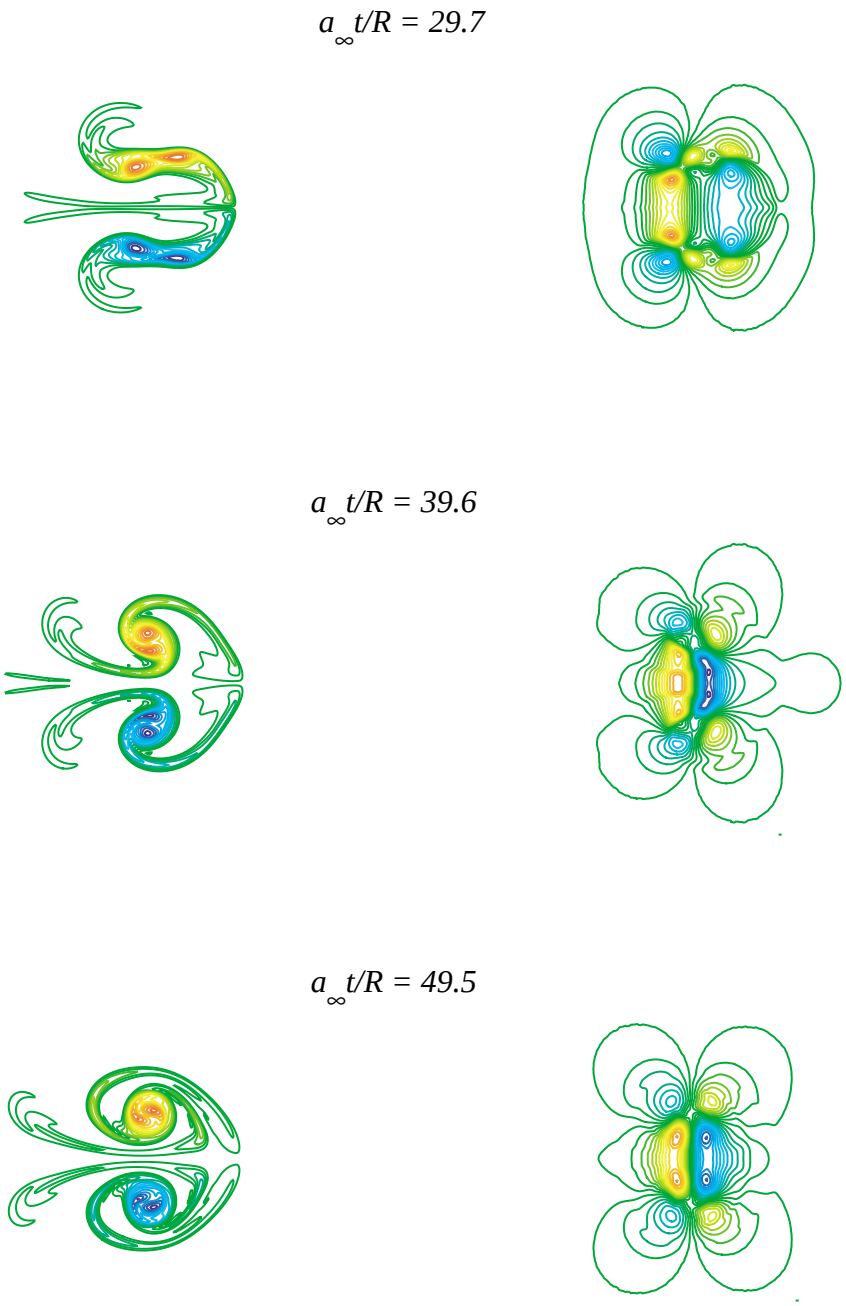

Figure 6.16: Vorticity and dilatation in $r_0 = 0.45$, $M_0 = 0.1867$ leapfrogging vortices problem (cont'd).

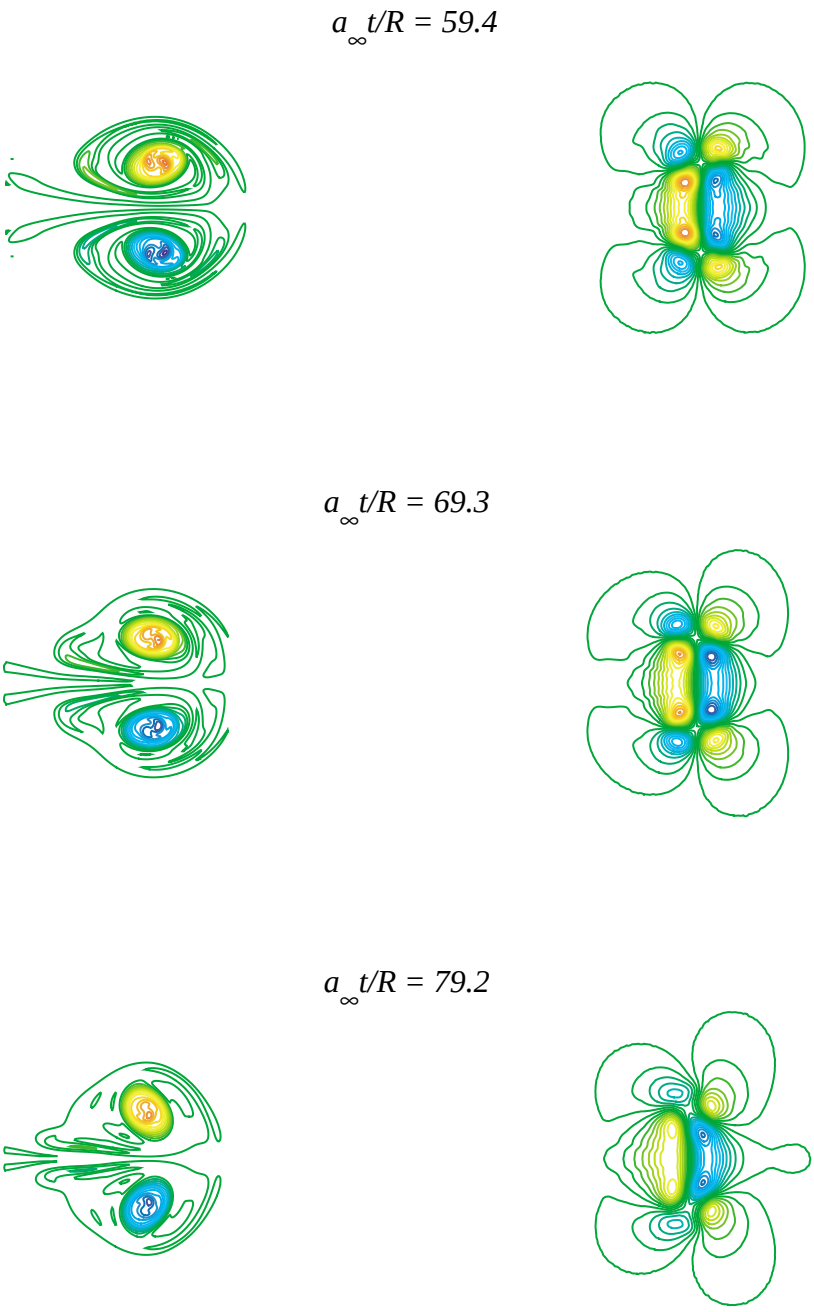

Figure 6.16: Vorticity and dilatation in $r_0 = 0.45$, $M_0 = 0.1867$ leapfrogging vortices problem (cont'd).

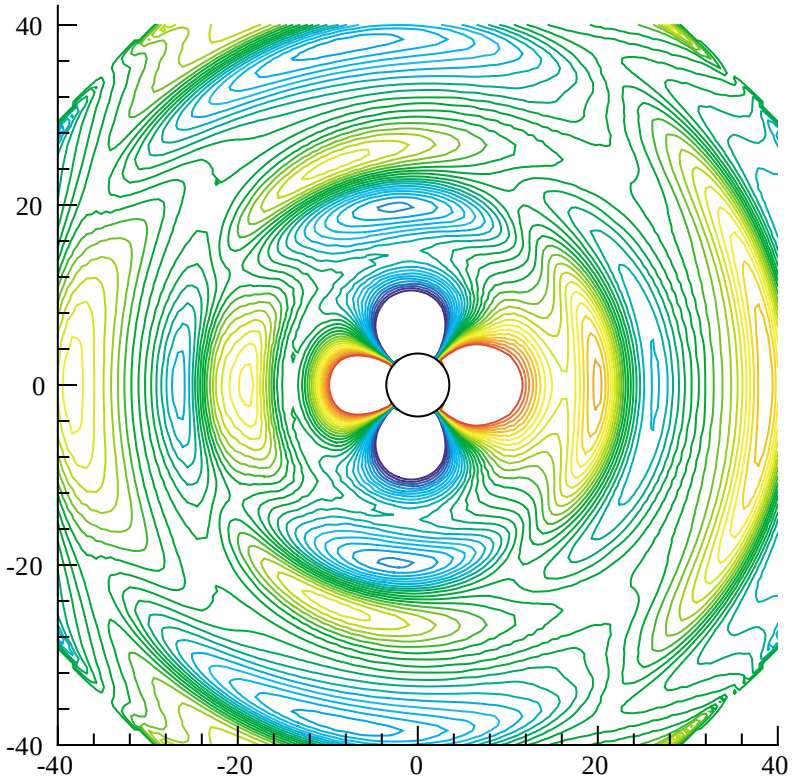

Figure 6.17: Pressure field from $r_0 = 0.45$, $M_0 = 0.1867$ leapfrogging vortices at $a_\infty t/R = 60$. The Kirchhoff surface is shown as a circle centered at the origin.

6.3.3 Case 3: $r_0 = 0.45$, $M_0 = 0.1867$

In the final case we increase the core radius of the vortices to $r_0 = 0.45$ and decrease the vortex Mach number to $M_0 = 0.1867$. The vorticity and dilatation fields at several instants are depicted in the panels of Figure 6.16. The contour levels for the vorticity are in the range $[-1.5, 1.5]$ in increments of $\Delta\omega = 0.103$, and those of the dilatation are in $[-0.01, 0.01]$ at steps of $\Delta\theta = 6.90 \times 10^{-4}$. The larger cores lead to significant overlap between the straining fields of like-sign vortices. They are quickly drawn together as they rotate, shearing each other and coalescing within one-half rotation. During this process, filaments of small vorticity are ejected by each vortex, most of which are stretched and wrap around the vortex cores as

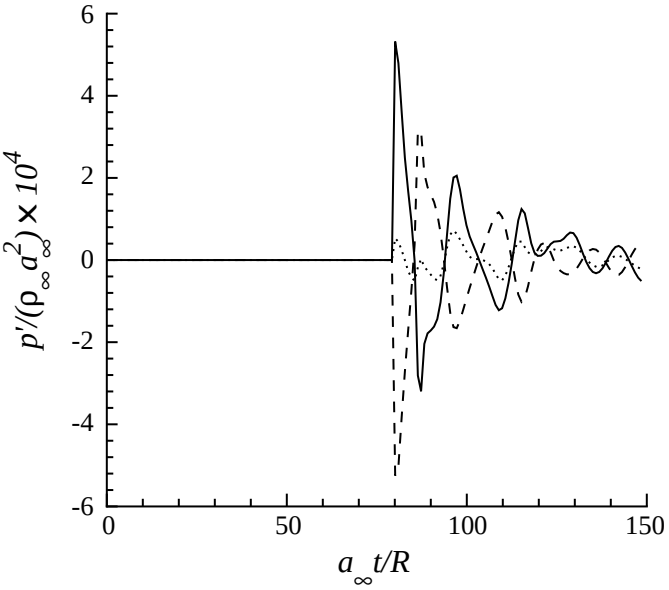

Figure 6.18: Pressure fluctuations from $r_0 = 0.45$, $M_0 = 0.1867$ leapfrogging vortices at $r = 75.6$. At $\theta = 0°$: '——'; $\theta = 90°$: '– – –'; $\theta = 45°$: '· · · · · ·'.

they merge. The remainder of the filaments are not pulled with the structures but leave the left side of the domain (or, in a fixed frame, remain stationary while the vortical structures advect forward). The merging cores eventually form two elliptical vortices. The dilatation during the merging process transforms from four quadrupole structures that advect with each distinct core, into two relatively stationary quadrupoles in the elliptical state.

The acoustic field at $t = 60$ is depicted in Figure 6.17. It exhibits the same slightly rearward-shifted quadrupole directivity as in Case 1. However, the acoustic wavelength is much smaller (approximately $\lambda = 16$), and the region between waves is not as quiet. The pressure fluctuations at three points at a radius of $r = 75.6$ are shown in Figure 6.18. After the initial transient, the fluctuations are more oscillatory than in the case of smaller cores, and their magnitude decays quickly. The results at $\theta = 90°$ are nearly 180° out of phase with those at $\theta = 0°$.

As a further evaluation of Möhring's analogy, the result from this formula at

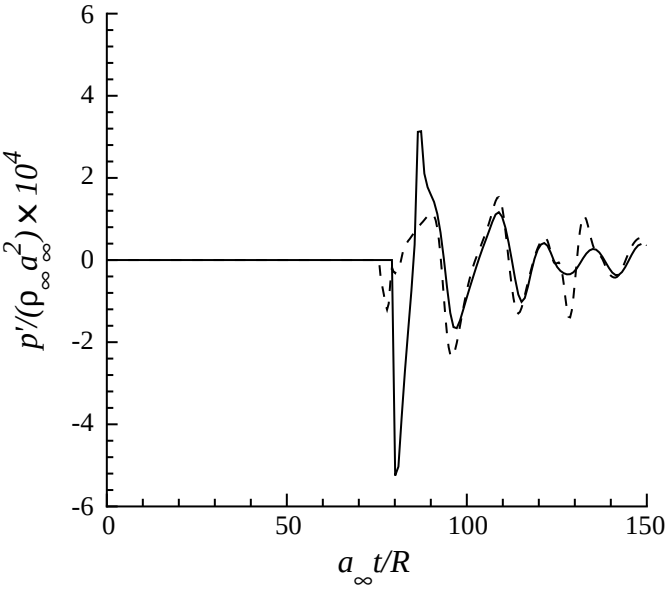

Figure 6.19: Pressure fluctuations from $r_0 = 0.45$, $M_0 = 0.1867$ leapfrogging vortices at $(r, \theta) = (75.6, 90^\circ)$. DVPM and Kirchhoff surface at $R_s = 3.5$: '——'; DVPM and Möhring analogy: '– – –'.

$(r, \theta) = (75.6, 90^\circ)$ is presented in Figure 6.19 with that of the Kirchhoff surface. The agreement is better than in the small-core case, aside from some discrepancy near the end of the merging process, due to noncompactness effects.

Chapter 7

Conclusions and Future work

A vortex particle method for unsteady two-dimensional compressible flow has been developed and applied to several problems, with good results. This is the first known Lagrangian method for the simulation of the full compressible Navier-Stokes equations. By using particles that are able to change volume and that carry vorticity, dilatation, enthalpy, entropy, and density, the equations of motion are satisfied. The vorticity description makes trivial the transformation from a compressible to incompressible flow solver by obviating the need for special treatment of the pressure in the latter case, as velocity-based methods rely on.

The natural efficiency of incompressible vortex methods has been compromised to some degree because of the need for including particles in the irrotational region. It is unmerited to view this as a weakness of the method, however, for in compressible flow simulation these outer regions are just as important to evaluate as the vortical region. Because of the small relative magnitude of the acoustic field, the method requires more delicate application of techniques that have proven robust for incompressible vortex methods, for instance computation of derivatives using PSE (which must now suppress dispersion of waves and accurately treat the balance of terms that evolve the dilatation field) and interpolation during remeshing (which must preserve smoothness in the interpolated quantities). This subtle balance comes as no surprise, as workers in computational aeroacoustics have long been cognizant of the need for high-order methods (e.g., Lele (1997)).

Out of this need, PSE has been extended in the present work through the development of higher-order-accurate kernels for use in approximating arbitrary differential operators. These new kernels allow many new applications of PSE, particularly in wave propagation problems, but also in other contexts in which particle methods are applied. Use of PSE in the wave operator raises new questions, to which we have provided answers. The dispersive character of PSE was explored and it was found that only high-order-accurate kernels should be used in contexts of wave propagation. This analysis also revealed the weaknesses of low-order-accurate kernels in diffusion problems, and suggests that commonly-used 2nd-order-accurate kernels should be used with care. We also found that increasing the order of accuracy of the kernel improves the computational efficiency, but by an amount which decreases as the order increases. For computing derivatives near the edge of the computational domain, we have developed one-sided integral operators which only look inward for information. Such a treatment is used for enforcing a non-reflecting boundary condition, but could be applied to wall-bounded flows as an alternative to the image treatment employed by Ploumhans and Winckelmans (2000). Finally, it was shown that on smoothly distorting grids PSE performs reasonably well, especially when kernels of variable size are employed, but that occasional reinitialization of the particles is ultimately essential for accuracy at long times.

Previous discussion of remeshing has only provided empirical guidance on how often it should be applied. Also, it was found that existing interpolation kernels led to poor results when applied in compressible flow simulation, due to the subtle balance of the dilatation. In the present work we developed smoothing kernels that lead to much better results, while almost exactly conserving important global quantities. Using available information about the principal axes of the rate of strain in the flow, we developed a criterion for the necessary frequency of remeshing.

A scheme for enforcing a non-reflecting boundary condition has been introduced and successfully implemented. This boundary treatment is sufficient for absorbing incident acoustic waves, but as discussed in §4.3, does not fully exploit

the decomposition of the velocity at the heart of the method. A more natural scheme could be developed that somehow exploits this decomposition, or perhaps integrates a Kirchhoff surface directly into the method.

The fast multipole method has been adapted to compressible particles for more efficient calculation. The use of such a fast summation method and the quad-tree description of the domain that it relies on are crucial to the success of the method. The $O(N^2)$ nature of the unmodified scheme is even more prohibitive in compressible flow because of the need for covering a larger domain with particles and because of the larger set of equations that must be solved. Therefore, effort was invested in finding an optimal degree of refinement of the quad-tree that avoided extraneous particle-particle interactions while retaining the necessary accuracy.

The new vortex method has been applied to co-rotating vortices and leapfrogging vortices in compressible flow, and to the baroclinic generation of vorticity, and the results agree well with those of previous work or analytical prediction. The acoustic field has been computed using a two-dimensional Kirchhoff surface, using the limited acoustic information available from a nearfield simulation. Also, the method has been demonstrated to perform well for the steepening of waves in the solution of Burgers' equation. It should be noted that problems of higher Mach number than those attempted in this work lead to larger magnitude of dilatation, and hence faster rates of change of the particle volumes. Smaller time step sizes and more frequent remeshing are required for such simulations, although the effects are somewhat mitigated by adjusting the blob size, as shown in §3.4.4.

We believe this method shows promise. The Lagrangian description makes the method well suited for simulating problems which are challenging for fixed-grid schemes. For example, mixing problems in compressible flow can be computed readily, as the advection of passive scalars is trivial. Further developments are necessary in order to solve problems of larger scale, however. A more "efficient" definition of the particles—for instance, a division of the particles into those that actively contribute to the velocity and those that are only passively convected—should be explored, possibly using domain decomposition techniques. Such a divi-

sion would permit simulations with two different time steps when the time scales of physical phenomena in the flow are distinct. Along the same lines, an implementation of the method with variably-sized particles, which would allow more efficient resolution of flows with disparate length scales, would be very useful. Such an extension would make simultaneous solution of the near- and acoustic fields practical. Certainly many interesting aeroacoustic problems involve interactions with solid boundaries, and a computational method that allows for these interactions is desirable. Some incompressible methods rely on a viscous splitting algorithm to enforce no-slip at the wall (Koumoutsakos et al., 1994); it is likely that this procedure could be adapted to flows with dilatation. Such a development would allow simulation in complex geometries that pose difficulties for fixed-grid schemes. Finally, using existing techniques for computing vortex stretching, we believe that the method is readily extendable to three-dimensional flows.

Appendix A

The 2-D particle evolution equations

Here we apply the treatments described in §3.2 and §4.3.1 to the equations of motion in two space dimensions, and then write the particle evolution equations in their entirety. To write them in their most "compact" form, we define certain shorthand symbols. In PSE, the difference of strengths between two particles is commonly used:

$$\Delta f_{qp} = f_q - f_p. \tag{A.1}$$

Many different kernels are used in the method. For instance, in the particle velocities, the regularized kernel is written as

$$\mathbf{K}_{\varepsilon,pq} = \mathbf{K}_\varepsilon(\mathbf{x}_p - \mathbf{x}_q), \tag{A.2}$$

the regularized velocity gradient kernel is shortened to

$$(R_\varepsilon^{ij})_{pq} = \frac{\partial K_{\varepsilon,i}}{\partial x_j}(\mathbf{x}_p - \mathbf{x}_q), \tag{A.3}$$

and the PSE kernel is expressed as

$$\eta_{\varepsilon,pq}^{(\alpha_1,\alpha_2)} = \eta_\varepsilon^{(\alpha_1,\alpha_2)}(\mathbf{x}_p - \mathbf{x}_q), \tag{A.4}$$

where the superscript indicates the α_1^{th} derivative in the x_1 direction and the α_2^{th} derivative in the x_2 direction. Using this notation, the full equations are

$$\frac{d\mathbf{x}_p}{dt} = \sum_q \Gamma_q \mathbf{K}_{\varepsilon,pq} \times \hat{\mathbf{e}}_3 - \sum_q Q_q \mathbf{K}_{\varepsilon,pq}, \tag{A.5a}$$

$$\begin{aligned}
\frac{d\Gamma_p}{dt} =& \frac{V_p}{\varepsilon^2} \sum_{q,r} V_q V_r \left(h_q(s_r + s_q)\eta^{(0,1)}_{\varepsilon,qr} + h_p(s_r + s_p)\eta^{(0,1)}_{\varepsilon,pr} \right) \eta^{(1,0)}_{\varepsilon,pq} \\
&- \frac{V_p}{\varepsilon^2} \sum_{q,r} V_q V_r \left(h_q(s_r + s_q)\eta^{(1,0)}_{\varepsilon,qr} + h_p(s_r + s_p)\eta^{(1,0)}_{\varepsilon,pr} \right) \eta^{(0,1)}_{\varepsilon,pq} \\
&+ \frac{1}{Re}\frac{1}{\varepsilon^2} \sum_{q,r} \left\{ \frac{V_p}{\rho_q} \left[\frac{4}{3}(V_q Q_r + V_r Q_q)\eta^{(0,1)}_{\varepsilon,qr} + (V_q \Gamma_r + V_r \Gamma_q)\eta^{(1,0)}_{\varepsilon,qr} \right] \right. \\
&\left. + \frac{V_q}{\rho_p} \left[\frac{4}{3}(V_p Q_r + V_r Q_p)\eta^{(0,1)}_{\varepsilon,pr} + (V_p \Gamma_r + V_r \Gamma_p)\eta^{(1,0)}_{\varepsilon,pr} \right] \right\} \eta^{(1,0)}_{\varepsilon,pq} \\
&- \frac{1}{Re}\frac{1}{\varepsilon^2} \sum_{q,r} \left\{ \frac{V_p}{\rho_q} \left[\frac{4}{3}(V_q Q_r + V_r Q_q)\eta^{(1,0)}_{\varepsilon,qr} - (V_q \Gamma_r + V_r \Gamma_q)\eta^{(0,1)}_{\varepsilon,qr} \right] \right. \\
&\left. + \frac{V_q}{\rho_p} \left[\frac{4}{3}(V_p Q_r + V_r Q_p)\eta^{(1,0)}_{\varepsilon,pr} - (V_p \Gamma_r + V_r \Gamma_p)\eta^{(0,1)}_{\varepsilon,pr} \right] \right\} \eta^{(0,1)}_{\varepsilon,pq},
\end{aligned} \tag{A.5b}$$

$$\begin{aligned}
\frac{dQ_p}{dt} =& 2V_p \left\{ \sum_{q,r} \left[\Gamma_q (R^{21}_\varepsilon)_{pq} - Q_q (R^{11}_\varepsilon)_{pq} \right] \left[-\Gamma_r (R^{12}_\varepsilon)_{pr} - Q_r (R^{22}_\varepsilon)_{pr} \right] \right. \\
&\left. - \sum_{q,r} \left[\Gamma_q (R^{22}_\varepsilon)_{pq} - Q_q (R^{12}_\varepsilon)_{pq} \right] \left[-\Gamma_r (R^{11}_\varepsilon)_{pr} - Q_r (R^{21}_\varepsilon)_{pr} \right] \right\} \\
&- \frac{1}{\varepsilon^2} \sum_q V_p V_q \Delta h_{qp} \eta^{\text{lap}}_{\varepsilon,pq} \\
&+ \frac{V_p}{\varepsilon^2} \sum_{q,r} V_q V_r \left(h_q(s_r + s_q)\eta^{(1,0)}_{\varepsilon,qr} + h_p(s_r + s_p)\eta^{(1,0)}_{\varepsilon,pr} \right) \eta^{(1,0)}_{\varepsilon,pq} \\
&+ \frac{V_p}{\varepsilon^2} \sum_{q,r} V_q V_r \left(h_q(s_r + s_q)\eta^{(0,1)}_{\varepsilon,qr} + h_p(s_r + s_p)\eta^{(0,1)}_{\varepsilon,pr} \right) \eta^{(0,1)}_{\varepsilon,pq} \\
&+ \frac{1}{Re}\frac{1}{\varepsilon^2} \sum_{q,r} \left\{ \frac{V_p}{\rho_q} \left[\frac{4}{3}(V_q Q_r + V_r Q_q)\eta^{(1,0)}_{\varepsilon,qr} - (V_q \Gamma_r + V_r \Gamma_q)\eta^{(0,1)}_{\varepsilon,qr} \right] \right. \\
&\left. + \frac{V_q}{\rho_p} \left[\frac{4}{3}(V_p Q_r + V_r Q_p)\eta^{(1,0)}_{\varepsilon,pr} - (V_p \Gamma_r + V_r \Gamma_p)\eta^{(0,1)}_{\varepsilon,pr} \right] \right\} \eta^{(1,0)}_{\varepsilon,pq} \\
&+ \frac{1}{Re}\frac{1}{\varepsilon^2} \sum_{q,r} \left\{ \frac{V_p}{\rho_q} \left[\frac{4}{3}(V_q Q_r + V_r Q_q)\eta^{(0,1)}_{\varepsilon,qr} + (V_q \Gamma_r + V_r \Gamma_q)\eta^{(1,0)}_{\varepsilon,qr} \right] \right. \\
&\left. + \frac{V_q}{\rho_p} \left[\frac{4}{3}(V_p Q_r + V_r Q_p)\eta^{(0,1)}_{\varepsilon,pr} + (V_p \Gamma_r + V_r \Gamma_p)\eta^{(1,0)}_{\varepsilon,pr} \right] \right\} \eta^{(0,1)}_{\varepsilon,pq},
\end{aligned} \tag{A.5c}$$

$$\frac{ds_p}{dt} = \frac{1}{Re}\frac{\Phi_p}{\rho_p h_p} + \frac{1}{RePr}\frac{1}{\rho_p h_p \varepsilon^2}\sum_q V_q \Delta h_{qp} \eta^{\text{lap}}_{\varepsilon,pq}, \tag{A.5d}$$

$$\frac{dV_p}{dt} = Q_p. \tag{A.5e}$$

The enthalpy strength is calculated from

$$\frac{dh_p}{dt} = -(\gamma-1)h_p\theta_p + \frac{\gamma}{Re}\frac{\Phi_p}{\rho_p} + \frac{\gamma}{RePr}\frac{1}{\rho_p \varepsilon^2}\sum_q V_q \Delta h_{qp}\eta^{\text{lap}}_{\varepsilon,pq} \tag{A.6}$$

and viscous dissipation is computed as follows:

$$\begin{aligned}\Phi_p = &\frac{\Gamma_p^2}{V_p^2} + \frac{4}{3}\frac{Q_p^2}{V_p^2} \\ &- 2\left\{\sum_{q,r}\left[\Gamma_q (R_\varepsilon^{21})_{pq} - Q_q (R_\varepsilon^{11})_{pq}\right]\left[-\Gamma_r (R_\varepsilon^{12})_{pr} - Q_r (R_\varepsilon^{22})_{pr}\right]\right. \\ &\left. - \sum_{q,r}\left[\Gamma_q (R_\varepsilon^{22})_{pq} - Q_q (R_\varepsilon^{12})_{pq}\right]\left[-\Gamma_r (R_\varepsilon^{11})_{pr} - Q_r (R_\varepsilon^{21})_{pr}\right]\right\}.\end{aligned} \tag{A.7}$$

In the boundary zone, equation (A.6) is replaced by the particle form of the boundary condition (4.10):

$$\frac{dh_p}{dt} = -\frac{1}{R_p \varepsilon}\sum_{q, R_q < R_p} V_q \Delta h_{pq}\left(\eta^{R,(1,0)}_{pq} x_{p,1} + \eta^{L,(0,1)}_{pq} x_{p,2}\right) - \frac{h_p - \frac{1}{\gamma-1}}{2R_p}, \tag{A.8}$$

where $R_p = |\mathbf{x}_p| = \sqrt{x_{p,1}^2 + x_{p,2}^2}$ and the notation $\eta^{L,(\alpha_1,\alpha_2)}$ indicates that the kernel is the left-sided kernel for approximating the (α_1, α_2)- derivative. The linear combination of kernels is used to approximate the gradient in the local radial direction (see Figure 4.4). Equation (A.8) holds for particles in the boundary zone, but the sum is over *all* particles, provided that $R_q < R_p$. This criterion is used to establish that the sum is over the inner half-plane, as described in §4.3.1. Clearly this restriction corresponds to a circle rather than a half-plane, and the intersection of this region with the kernel support corresponds to a lens-shaped region rather than a semi-circle, but the error is smaller than the leading-order error in the boundary condition itself. Equation (A.8) is supplemented by equations (A.5a)

(the boundary particles are allowed to move) and (A.5e). Γ_p, Q_p and s_p are assumed constant in the boundary region.

Appendix B

A list of PSE kernels

For reference, this appendix contains kernels of several orders of accuracy for application to first and second derivatives in one- and two-dimensional problems, in both full-space and one-sided operators. As a shorthand, the kernel is expressed as

$$\eta^{(\alpha_1,\alpha_2,\ldots,\alpha_d)},$$

where the superscript indicates the α_1^{th} derivative in the x_1 direction, the α_2^{th} derivative in the x_2 direction, and so on.

1-d first derivatives, full-space

$$\eta^1(x) = \frac{x}{\sqrt{\pi}} e^{-x^2} \times \begin{cases} (-2) & & & & & & & \textbf{2nd order} \\ (-5 & + & 2x^2) & & & & & \textbf{4th order} \\ (-\frac{35}{4} & + & 7x^2 & - & x^4) & & & \textbf{6th order} \\ (-\frac{105}{8} & + & \frac{63}{4}x^2 & - & \frac{9}{2}x^4 & + & \frac{1}{3}x^6) & \textbf{8th order} \end{cases}$$

1-d first derivatives, left-sided

$$\eta^{L,1}(x) = \frac{x}{\sqrt{\pi}} e^{-x^2} \times \begin{cases} (-4) & & & & & & & \textbf{1st order} \\ (-16 & + & 8x^2) & & & & & \textbf{2nd order} \\ (-40 & + & 44x^2 & - & 8x^4) & & & \textbf{3rd order} \\ (-80 & + & 144x^2 & - & 56x^4 & + & \tfrac{16}{3}x^6) & \textbf{4th order} \end{cases}$$

Right-sided kernels are identical to the left-sided ones.

1-d second derivatives, full-space

$$\eta^{2}(x) = \frac{1}{\sqrt{\pi}} e^{-x^2} \times \begin{cases} (4) & & & & & & & \textbf{2nd order} \\ (10 & - & 4x^2) & & & & & \textbf{4th order} \\ (\tfrac{35}{2} & - & 14x^2 & + & 2x^4) & & & \textbf{6th order} \\ (\tfrac{105}{4} & - & \tfrac{63}{2}x^2 & + & 9x^4 & - & \tfrac{2}{3}x^6) & \textbf{8th order} \end{cases}$$

2-d first derivatives, full-space

$$\eta^{(1,0)}(\mathbf{x}) = \frac{x_1}{\pi} e^{-|\mathbf{x}|^2} \times \begin{cases} (-2) & & & & & & & \textbf{2nd order} \\ (-6 & + & 2|\mathbf{x}|^2) & & & & & \textbf{4th order} \\ (-12 & + & 8|\mathbf{x}|^2 & - & |\mathbf{x}|^4) & & & \textbf{6th order} \\ (-20 & + & 20|\mathbf{x}|^2 & - & 5|\mathbf{x}|^4 & + & \tfrac{1}{3}|\mathbf{x}|^6) & \textbf{8th order} \end{cases}$$

Note that the $(0,1)$-derivative is approximated using the same kernels with the x_1 factor replaced by x_2.

2-d first derivatives, left-sided

$$\eta^{L,(1,0)}(\mathbf{x}) = \frac{x_1}{\pi} e^{-|\mathbf{x}|^2} \times \begin{cases} (-4) & & & & & & & \textbf{1st order} \\ (-20 & + & 8|\mathbf{x}|^2) & & & & & \textbf{2nd order} \\ (-60 & + & 52|\mathbf{x}|^2 & - & 8|\mathbf{x}|^4) & & & \textbf{3rd order} \\ (-140 & + & 196|\mathbf{x}|^2 & - & 64|\mathbf{x}|^4 & + & \tfrac{16}{3}|\mathbf{x}|^6) & \textbf{4th order} \end{cases}$$

Again, these kernels are indentical to their right-sided counterparts, and they can be adapted for use in approximating the $(0,1)$-derivative by replacing x_1 by x_2.

2-d Laplacian, full-space

$$\eta^{\text{lap}}(\mathbf{x}) = \frac{1}{\pi} e^{-|\mathbf{x}|^2} \times \begin{cases} (4) & & & & & & & \textbf{2nd order} \\ (12 & - & 4|\mathbf{x}|^2) & & & & & \textbf{4th order} \\ (24 & - & 16|\mathbf{x}|^2 & + & 2|\mathbf{x}|^4) & & & \textbf{6th order} \\ (40 & - & 40|\mathbf{x}|^2 & + & 10|\mathbf{x}|^4 & - & \tfrac{2}{3}|\mathbf{x}|^6) & \textbf{8th order} \end{cases}$$

Appendix C

The 2-D Kirchhoff surface

C.1 Formulation

We derive here the adaptation of the Kirchhoff surface methodology for application to two-dimensional problems. Consider a domain Ω_{far}, bounded internally by a stationary surface $\partial\Omega$ and extending to infinity, in which a quantity f is governed by the linear homogeneous wave equation in a medium with wave speed c_0:

$$\frac{\partial^2 f}{\partial t^2} - c_0^2 \nabla^2 f = 0. \tag{C.1}$$

We can reformulate this equation in integral form through the use of the Green's function for the wave operator. Provided that $G(\mathbf{x}, t|\boldsymbol{\xi}, \tau)$ satisfies

$$\frac{\partial^2 f}{\partial t^2} - c_0^2 \nabla^2 f = \delta(\mathbf{x} - \boldsymbol{\xi})\delta(t - \tau),$$

obeys the causality constraint $G(\mathbf{x}, t|\boldsymbol{\xi}, \tau) = 0$ for $t < \tau$, and vanishes as $|\mathbf{x}| \to \infty$, we can write (see, e.g., Stakgold, 1967)

$$\begin{aligned} f(\mathbf{x}, t) = &\int_{\Omega_{\text{far}}} \left[G(\mathbf{x}, t|\boldsymbol{\xi}, 0) \frac{\partial f}{\partial t}(\boldsymbol{\xi}, 0) + \frac{\partial G}{\partial t}(\mathbf{x}, t|\boldsymbol{\xi}, 0) f(\boldsymbol{\xi}, 0) \right] d\boldsymbol{\xi} \\ &+ c_0^2 \int_0^t \int_{\partial\Omega} [\nabla_{\boldsymbol{\xi}} G(\mathbf{x}, t|\boldsymbol{\xi}, \tau) f(\boldsymbol{\xi}, \tau) - G(\mathbf{x}, t|\boldsymbol{\xi}, \tau) \nabla_{\boldsymbol{\xi}} f(\boldsymbol{\xi}, \tau)] \cdot \mathbf{n}_\xi \, dS(\boldsymbol{\xi}) \, d\tau \end{aligned} \tag{C.2}$$

for any point $\mathbf{x} \in \Omega_{\text{far}}$, where $\mathbf{n}_\xi$ is the normal of $\partial\Omega$ at $\boldsymbol{\xi}$ pointing *into* Ω_{far}. This expression can be regarded as a solution of (C.1), provided that the necessary initial and boundary data are known.

We will assume that f and its time derivative are initially zero in Ω_{far}, so the first integral in (C.2) vanishes. Thus we are left with the formula for the acoustic field from a stationary Kirchoff surface:

$$f(\mathbf{x},t) = c_0^2 \int_0^t \int_{\partial\Omega} [\nabla_{\boldsymbol{\xi}} G(\mathbf{x},t|\boldsymbol{\xi},\tau) f(\boldsymbol{\xi},\tau) - G(\mathbf{x},t|\boldsymbol{\xi},\tau)\nabla_{\boldsymbol{\xi}} f(\boldsymbol{\xi},\tau)] \cdot \mathbf{n}_\xi \, dS(\boldsymbol{\xi}) \, d\tau. \tag{C.3}$$

The Green's function for the linear wave operator in two dimensions is

$$G(\mathbf{x},t) = \frac{1}{2\pi c_0} \frac{H(c_0 t - |\mathbf{x}|)}{(c_0^2 t^2 - |\mathbf{x}|^2)^{1/2}}, \tag{C.4}$$

which represents the response of the medium to an instantaneous, concentrated source at the origin at $t = 0$. Because of the invariance of the wave equation with respect to time and space translations, $G(\mathbf{x},t|\boldsymbol{\xi},\tau) = G(\mathbf{x}-\boldsymbol{\xi}, t-\tau)$. The presence of the Heaviside function, H, in (C.4) represents the residual response to an impulsive forcing after the wavefront has passed, unique to two-dimensional problems. We need the gradient of this function with respect to the source position,

$$\begin{aligned}
\frac{\partial G}{\partial \xi_i}(\mathbf{x},t|\boldsymbol{\xi},\tau) = \frac{1}{2\pi c_0} \Bigg\{ & -\frac{H'[c_0(t-\tau) - |\mathbf{x}-\boldsymbol{\xi}|]}{[c_0^2(t-\tau)^2 - |\mathbf{x}-\boldsymbol{\xi}|^2]^{1/2}} \frac{\partial}{\partial \xi_i} |\mathbf{x}-\boldsymbol{\xi}| \\
& + \frac{1}{2} \frac{H[c_0(t-\tau) - |\mathbf{x}-\boldsymbol{\xi}|]}{[c_0^2(t-\tau)^2 - |\mathbf{x}-\boldsymbol{\xi}|^2]^{3/2}} \frac{\partial}{\partial \xi_i} |\mathbf{x}-\boldsymbol{\xi}|^2 \Bigg\} \\
= \frac{1}{2\pi c_0} \Bigg\{ & \frac{H'[c_0(t-\tau) - |\mathbf{x}-\boldsymbol{\xi}|]}{[c_0^2(t-\tau)^2 - |\mathbf{x}-\boldsymbol{\xi}|^2]^{1/2}} \\
& - \frac{H[c_0(t-\tau) - |\mathbf{x}-\boldsymbol{\xi}|]}{[c_0^2(t-\tau)^2 - |\mathbf{x}-\boldsymbol{\xi}|^2]^{3/2}} |\mathbf{x}-\boldsymbol{\xi}| \Bigg\} \hat{e}_{R,i},
\end{aligned}$$

where $\hat{e}_{R,i} = \frac{x_i - \xi_i}{|\mathbf{x}-\boldsymbol{\xi}|}$ is the unit vector from the source to the observation point. We

note that $H'(\eta)\partial\eta/\partial\tau = \partial H/\partial\tau$, so the first term can be written as

$$-\frac{1}{2\pi c_0^2}\frac{\frac{\partial}{\partial\tau}H[c_0(t-\tau)-|\mathbf{x}-\boldsymbol{\xi}|]}{[c_0^2(t-\tau)^2-|\mathbf{x}-\boldsymbol{\xi}|^2]^{1/2}}\hat{e}_{R,i}.$$

Now we can regard (C.3) as the sum of three integrals over space and time,

$$f(\mathbf{x},t) = I_1(\mathbf{x},t) + I_2(\mathbf{x},t) + I_3(\mathbf{x},t),$$

each of which we consider separately. The first integral requires some work:

$$\begin{aligned} I_1(\mathbf{x},t) &= c_0^2\int_0^t\int_{\partial\Omega} f(\boldsymbol{\xi},\tau)\left\{-\frac{1}{2\pi c_0^2}\frac{\frac{\partial}{\partial\tau}H[c_0(t-\tau)-|\mathbf{x}-\boldsymbol{\xi}|]}{[c_0^2(t-\tau)^2-|\mathbf{x}-\boldsymbol{\xi}|^2]^{1/2}}\hat{\mathbf{e}}_R\right\}\cdot\mathbf{n}_\xi\,dS(\boldsymbol{\xi})\,d\tau \\ &= -\frac{1}{2\pi c_0}\int_0^t\int_{\partial\Omega} f(\boldsymbol{\xi},\tau)\frac{\frac{\partial}{\partial\tau}H[c_0(t-\tau)-|\mathbf{x}-\boldsymbol{\xi}|]}{[(t-\tau)^2-|\mathbf{x}-\boldsymbol{\xi}|^2/c_0^2]^{1/2}}\hat{\mathbf{e}}_R\cdot\mathbf{n}_\xi\,dS(\boldsymbol{\xi})\,d\tau. \end{aligned}$$

We integrate with respect to τ by parts, to produce

$$\begin{aligned} I_1(\mathbf{x},t) = &-\frac{1}{2\pi c_0}\int_{\partial\Omega} f(\boldsymbol{\xi},\tau)\,\frac{H[c_0(t-\tau)-|\mathbf{x}-\boldsymbol{\xi}|]}{[(t-\tau)^2-|\mathbf{x}-\boldsymbol{\xi}|^2/c_0^2]^{1/2}}\hat{\mathbf{e}}_R\cdot\mathbf{n}_\xi\,dS(\boldsymbol{\xi})\Big|_{\tau=0}^{t} \\ &+\frac{1}{2\pi c_0}\int_0^t\int_{\partial\Omega}\frac{\partial}{\partial\tau}\left\{\frac{f(\boldsymbol{\xi},\tau)}{[(t-\tau)^2-|\mathbf{x}-\boldsymbol{\xi}|^2/c_0^2]^{1/2}}\right\}H[c_0(t-\tau)-|\mathbf{x}-\boldsymbol{\xi}|] \\ &\qquad\times\hat{\mathbf{e}}_R\cdot\mathbf{n}_\xi\,dS(\boldsymbol{\xi})\,d\tau. \end{aligned}$$

But we have already assumed that f is zero in Ω_{far}, and it is consistent with this supposition to assume that it is zero on $\partial\Omega$ as well. Furthermore, $H[c_0(t-\tau)-|\mathbf{x}-\boldsymbol{\xi}|]_{\tau=t} = H[-|\mathbf{x}-\boldsymbol{\xi}|] = 0$. Thus,

$$\begin{aligned} I_1(\mathbf{x},t) = &\frac{1}{2\pi c_0}\int_0^t\int_{\partial\Omega}\frac{\partial}{\partial\tau}\left\{\frac{f(\boldsymbol{\xi},\tau)}{[(t-\tau)^2-|\mathbf{x}-\boldsymbol{\xi}|^2/c_0^2]^{1/2}}\right\}H[t-\tau-|\mathbf{x}-\boldsymbol{\xi}|/c_0] \\ &\qquad\times\hat{\mathbf{e}}_R\cdot\mathbf{n}_\xi\,dS(\boldsymbol{\xi})\,d\tau. \end{aligned}$$

We can swap the order of integration and note that the Heaviside function vanishes when $c_0(t-\tau)-|\mathbf{x}-\boldsymbol{\xi}| < 0$, or $\tau > t-|\mathbf{x}-\boldsymbol{\xi}|/c_0$. We define a retarded time,

$t^* = t - |\mathbf{x} - \boldsymbol{\xi}|/c_0$, and expand the derivative to write

$$I_1(\mathbf{x},t) = \frac{1}{2\pi c_0}\int_{\partial\Omega}\int_0^{t^*}\left\{\frac{\frac{\partial f}{\partial\tau}(\boldsymbol{\xi},\tau)}{[(t-\tau)^2 - |\mathbf{x}-\boldsymbol{\xi}|^2/c_0^2]^{1/2}} + \frac{f(\boldsymbol{\xi},\tau)(t-\tau)}{[(t-\tau)^2 - |\mathbf{x}-\boldsymbol{\xi}|^2/c_0^2]^{3/2}}\right\} \times \hat{\mathbf{e}}_R\cdot\mathbf{n}_\xi\, d\tau\, dS(\boldsymbol{\xi}). \tag{C.5}$$

The second integral, I_2, is very simply

$$\begin{aligned} I_2(\mathbf{x},t) &= c_0^2\int_0^t\int_{\partial\Omega} f(\boldsymbol{\xi},\tau)\left\{-\frac{|\mathbf{x}-\boldsymbol{\xi}|}{2\pi c_0}\frac{H[c_0(t-\tau)-|\mathbf{x}-\boldsymbol{\xi}|]}{[c_0^2(t-\tau)^2 - |\mathbf{x}-\boldsymbol{\xi}|^2]^{3/2}}\right\}\hat{\mathbf{e}}_R\cdot\mathbf{n}_\xi\, dS(\boldsymbol{\xi}) \\ &= -\frac{1}{2\pi c_0}\int_{\partial\Omega}\int_0^{t^*}\frac{f(\boldsymbol{\xi},\tau)|\mathbf{x}-\boldsymbol{\xi}|/c_0}{[(t-\tau)^2 - |\mathbf{x}-\boldsymbol{\xi}|^2/c_0^2]^{3/2}}\hat{\mathbf{e}}_R\cdot\mathbf{n}_\xi\, d\tau\, dS(\boldsymbol{\xi}), \end{aligned} \tag{C.6}$$

and I_3 is

$$\begin{aligned} I_3(\mathbf{x},t) &= -c_0^2\int_0^t\int_{\partial\Omega}\nabla_{\boldsymbol{\xi}} f(\boldsymbol{\xi},\tau)\frac{1}{2\pi c_0}\frac{H[c_0(t-\tau)-|\mathbf{x}-\boldsymbol{\xi}|]}{[c_0^2(t-\tau)^2 - |\mathbf{x}-\boldsymbol{\xi}|^2]^{1/2}}\cdot\mathbf{n}_\xi\, dS(\boldsymbol{\xi})\, d\tau. \\ &= -\frac{1}{2\pi}\int_{\partial\Omega}\int_0^{t^*}\frac{\partial f}{\partial n_\xi}(\boldsymbol{\xi},\tau)\frac{d\tau}{[(t-\tau)^2 - |\mathbf{x}-\boldsymbol{\xi}|^2/c_0^2]^{1/2}}\, dS(\boldsymbol{\xi}). \end{aligned}$$

We combine the three integrals to form the following expression for the acoustic field in two dimensions:

$$f(\mathbf{x},t) = \frac{1}{2\pi}\int_{\partial\Omega}\int_0^{t^*}\left\{\left[\frac{1}{c_0}\frac{\partial}{\partial\tau} + \frac{1}{c_0(t-\tau)+|\mathbf{x}-\boldsymbol{\xi}|}\right] f(\boldsymbol{\xi},\tau)(\hat{\mathbf{e}}_R\cdot\mathbf{n}_\xi) - \frac{\partial f}{\partial n_\xi}(\boldsymbol{\xi},\tau)\right\} \times \frac{d\tau\, dS(\boldsymbol{\xi})}{[(t-\tau)^2 - |\mathbf{x}-\boldsymbol{\xi}|^2/c_0^2]^{1/2}}. \tag{C.7}$$

Note that the second term is proportional to $|\mathbf{x}-\boldsymbol{\xi}|^{-1} \sim |\mathbf{x}|^{-1}$ and is thus negligible in the farfield.

It is interesting to compare this expression with the three-dimensional formula (e.g., Pierce, 1989),

$$f(\mathbf{x},t) = \frac{1}{4\pi}\int_{\partial\Omega}\left\{\left[\frac{1}{c_0}\frac{\partial}{\partial\tau} + \frac{1}{|\mathbf{x}-\boldsymbol{\xi}|}\right] f(\boldsymbol{\xi},t^*)(\hat{\mathbf{e}}_R\cdot\mathbf{n}_\xi) - \frac{\partial f}{\partial n_\xi}(\boldsymbol{\xi},t^*)\right\}\frac{dS(\boldsymbol{\xi})}{|\mathbf{x}-\boldsymbol{\xi}|}.$$

The two expressions bear many similarities, but the response to a three-dimensional

disturbance is concentrated on the wavefront (known as Huyghens' principle), whereas a two-dimensional disturbance continues to affect the observation point long after the wavefront has passed, as the time integral in (C.7) accounts for.

C.2 Implementation

We describe now the numerical implementation of equation (C.7) for $\partial\Omega$ a circular surface of radius R_s. We arrange the coordinate system so that the origin coincides with the center of the circle, and thus for any point $\boldsymbol{\xi}$ on the surface, the local inward normal is equal to the radial unit vector, $\mathbf{n}_\xi = \hat{\mathbf{e}}_r$, and the normal derivative is equal to the radial derivative, $\frac{\partial}{\partial n_\xi} = \frac{\partial}{\partial r}$.

We treat the time integration first, writing (C.7) as

$$f(\mathbf{x}, t) = \frac{1}{2\pi} \int_{\partial\Omega} K(\mathbf{x}, \boldsymbol{\xi}, t)\, dS(\boldsymbol{\xi})$$

where we have defined $K(\mathbf{x}, \boldsymbol{\xi}, t)$ as the time integral. In the application of the Kirchhoff surface we will use data from the DVPM simulation, which is available only at certain time levels, for use on the surface. Thus, we break K into integrals over smaller intervals,

$$[0, t^*] = \bigcup_{n=0}^{N(t^*)-1} [t_n, t_{n+1}] \bigcup [t_{N(t^*)}, t^*].$$

The time intervals are established by the time levels at which the DVPM data is available and the resolution of the numerical quadrature that we desire; it is simplest to use a fixed interval size Δt_s that is some integral multiple of the time step size of the simulation. The initial time is $t_0 = 0$, and $N(t^*)$ is determined by the number of intervals of size Δt_s that are wholly contained within $[0, t^*]$. Since $t_n = n\Delta t_s$, then we require that $t^* - \Delta t_s < t_{N(t^*)} = N(t^*)\Delta t_s < t^*$, which is satisfied when $N(t^*) = \text{int}(t^*/\Delta t_s)$, where "int" computes the integer part of its argument.

In each time interval, the integrand is evaluated at the lower limit of the interval

and treated as constant, except for the factor $[(t-\tau)^2 - |\mathbf{x}-\boldsymbol{\xi}|^2/c_0^2]^{-1/2}$, which can vary considerably within an interval. But the resulting integral can be evaluated analytically, and we call the result the "modified" time interval, $\widetilde{\Delta t}_n$:

$$\begin{aligned}\widetilde{\Delta t}_n &= \int_{t_n}^{t_{n+1}} \frac{d\tau}{[(t-\tau)^2 - |\mathbf{x}-\boldsymbol{\xi}|^2/c_0^2]^{1/2}} \\ &= \log\left[\frac{t-t_n+\sqrt{(t-t_n)^2-|\mathbf{x}-\boldsymbol{\xi}|^2/c_0^2}}{t-t_{n+1}+\sqrt{(t-t_{n+1})^2-|\mathbf{x}-\boldsymbol{\xi}|^2/c_0^2}}\right].\end{aligned}$$

The final modified time interval is generally only a partial step, and equals

$$\widetilde{\Delta t}_{N(t^*)} = \log\left[\frac{t-t_{N(t^*)}+\sqrt{(t-t_{N(t^*)})^2-|\mathbf{x}-\boldsymbol{\xi}|^2/c_0^2}}{|\mathbf{x}-\boldsymbol{\xi}|/c_0}\right].$$

The resulting formula for K is

$$K(\mathbf{x},\boldsymbol{\xi},t) \approx \sum_{n=0}^{N(t^*)-1} \lambda(\mathbf{x},\boldsymbol{\xi},t_n)\widetilde{\Delta t}_n + \lambda(\mathbf{x},\boldsymbol{\xi},t_{N(t^*)})\widetilde{\Delta t}_{N(t^*)} \tag{C.8}$$

where

$$\lambda(\mathbf{x},\boldsymbol{\xi},\tau) = \left[\frac{1}{c_0}\frac{\partial}{\partial\tau} + \frac{1}{c_0(t-\tau)+|\mathbf{x}-\boldsymbol{\xi}|}\right] f(\boldsymbol{\xi},\tau)(\hat{\mathbf{e}}_R\cdot\hat{\mathbf{e}}_r) - \frac{\partial f}{\partial r}(\boldsymbol{\xi},\tau)$$

Finally, we treat the surface integral by dividing the circular surface into M_s intervals of size $\Delta\theta = 2\pi/M_s$, and thus $f(\mathbf{x},t)$ is computed with the formula

$$f(\mathbf{x},t) \approx \frac{1}{2\pi}\sum_{j=1}^{M_s} K(\mathbf{x},\xi_j,t)\Delta S_j, \tag{C.9}$$

where $\Delta S_j = R_s\Delta\theta$ and $\xi_j = (j-1)\Delta S_j$. Due to the periodicity of the surface, this quadrature is spectrally accurate.

Appendix D

Application to the 1-D Burgers' equation

As a simple evaluation of the behavior of this method in the presence of shocks, we consider the application of the techniques used in the method to the solution of Burgers' equation,

$$\frac{\partial u}{\partial t} + u\frac{\partial u}{\partial x} = \frac{1}{Re}\frac{\partial^2 u}{\partial x^2}. \tag{D.1}$$

Burgers' equation is useful because it is the simplest equation that contains both nonlinear convection and diffusive effects, and the balance between the two that is crucial to the physical formation of shocks. The exact solution can be found through the well-known Cole-Hopf transformation (see, e.g., Whitham, 1999). We will solve instead the first derivative of this equation,

$$\frac{\partial \theta}{\partial t} + u\frac{\partial \theta}{\partial x} = -\theta^2 + \frac{1}{Re}\frac{\partial^2 \theta}{\partial x^2}, \tag{D.2}$$

where $\theta = \partial u/\partial x$. When we discretize (D.2) with dilating particles and PSE for the viscous term, then we obtain the following set of ordinary differential equations

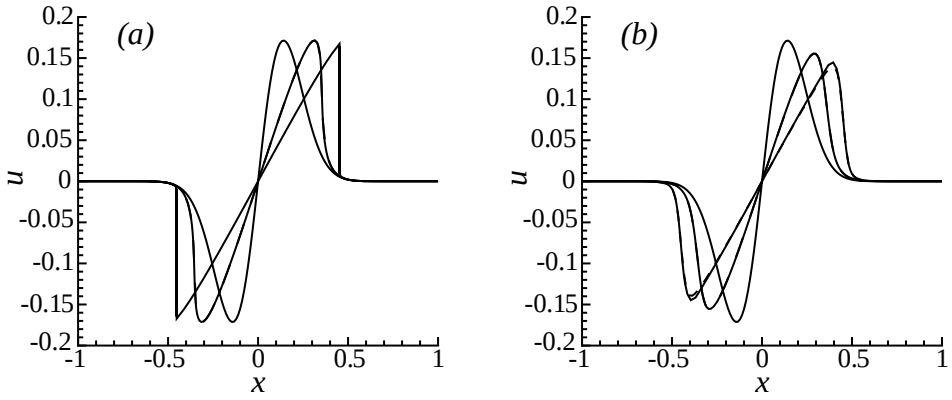

Figure D.1: Solution of Burgers' equation for N-wave. (a) Inviscid, and (b) $Re = 1000$, at $t = 0.0$, 1.0, and 2.0. Particle solution: '——'; exact: '– – –'.

to solve for the strengths, positions and volumes of the particles:

$$\begin{aligned}
\frac{dQ_p}{dt} &= \frac{1}{Re}\frac{1}{\varepsilon^2}\sum_q \left(V_pQ_q - V_qQ_p\right)\eta_\varepsilon^{\text{lap}}(x_p - x_q),\\
\frac{dx_p}{dt} &= \frac{1}{2}\sum_{x_q<x_p} Q_q - \frac{1}{2}\sum_{x_q>x_p} Q_q,\\
\frac{dV_p}{dt} &= Q_p.
\end{aligned} \tag{D.3}$$

The first of these equations governs the strengths of the particles. Note the disappearance of the $-\theta^2$ term, which was removed by combining with the volume equation. The second is the particle position equation, whose right-hand side is the velocity determined by the solution of $\partial u/\partial x = \theta$. Note that no regularizing function has been used; the one-dimensional velocity lacks the singular behavior of its higher-dimensional counterparts. Finally, the volumes are changed according to the third equation. The initial dilatation field is specified: $\theta(x,0) = f(x)$; and the initial strengths are set as $Q_p(0) = V_p(0)f(x_p(0))$.

The shock behavior is exhibited by an N-wave. Consider the following initial

distribution of the dilatation:

$$f(x) = 2\left(1 - 2\frac{x^2}{\sigma^2}\right)e^{-x^2/\sigma^2}.$$

The initial velocity field corresponding to this distribution is depicted in Figure D.1(a). Due to the nonlinear convective term, the regions of negative slope of u will tend to steepen as the solution progresses. This behavior can be seen in the other plots of Figure D.1(a), which represent the solution of equations (D.3) with $Re = 10^6$, using 181 particles on a domain of $[-1, 1]$ and 4th-order Runge-Kutta timestepping with a step size of $\Delta t = 0.01$. The PSE kernel radius was $\varepsilon = 1.8\Delta x$, although it was immaterial to this particular problem because of the very low viscosity. As the particle trajectories coalesce, shocks are formed which subsequently travel away from the origin. Shown on the same figure is the exact solution to the inviscid problem, computed via the method of characteristics. The two results are indistinguishable, because in the limit of $Re \to \infty$, equations (D.3) *are* the characteristic equations.

Figure D.1 depicts the more challenging solution of (D.3) for $Re = 1000$. With larger viscosity the timestep size must be decreased to $\Delta t = 0.005$; all other parameters remain unchanged. The exact solution is also shown, effected using the Cole-Hopf transformation and numerical integration. The delicate balance between the nonlinear and viscous effects in the steepening regions makes the accurate solution in these regions difficult, but PSE fares quite well.

Overall, the particle method performs well for this example problem. The particles trajectories coincide with the characteristics in the inviscid problem, so the method could be called optimal for Burgers' equation. It should be noted, however, that this behavior is peculiar to this problem. In shock problems of one-dimensional gasdynamics, there are three sets of characteristics, only one of which is followed by the particles. Thus, the method would not be expected to perform as optimally in that context. It is expected that the results would be comparable to those exhibited by the method of smoothed particle hydrodynamics, which has

been applied to the Sod shock tube problem in Monaghan and Gingold (1983). In that work it was found that a particular artificial viscosity was necessary to reduce the spurious oscillations. Because the particles cannot move along all of the characteristics of such a problem, it is not surprising that, without special treatment, they exhibit similar behavior to unmodified fixed-grid schemes.

Bibliography

Abramowitz, M. and Stegun, I. A., editors (1964). *Handbook of Mathematical Functions*. American Mathematical Series. National Bureau of Standards.

Anderson, C. and Greengard, C. (1985). On vortex methods. *SIAM J. Numer. Anal.*, 22(3), 413–440.

Anderson, C. R. (1985). A vortex method for flows with slight density variations. *J. Comput. Phys.*, 61, 417–444.

Barnes, J. and Hut, P. (1986). A hierarchical $O(N \log N)$ force-calculation algorithm. *Nature*, 324, 446–449.

Beale, J. T. and Majda, A. (1982). Vortex methods II: Higher order accuracy in two and three dimensions. *Math. Comp.*, 39(159), 29–52.

Beale, J. T. and Majda, A. (1985). High order accurate vortex methods with explicit velocity kernels. *J. Comput. Phys.*, 58, 188–208.

Chu, B.-T. and Kovásznay, L. S. G. (1958). Non-linear interactions in a viscous heat-conducting compressible gas. *J. Fluid Mech.*, 3, 494–514.

Colonius, T., Lele, S. K. and Moin, P. (1997). Sound generation in a mixing layer. *J. Fluid Mech.*, 330, 375–409.

Cottet, G.-H. (1996). Artificial viscosity models for vortex and particle methods. *J. Comput. Phys.*, 127, 299–308.

Cottet, G.-H. and Koumoutsakos, P. (2000). *Vortex Methods: Theory and Practice*. Cambridge University Press.

Cottet, G.-H., Koumoutsakos, P. and Salihi, M. L. O. (2000). Vortex methods with spatially varying cores. *J. Comput. Phys.*, 162, 164–185.

Cottet, G.-H. and Mas-Gallic, S. (1990). A particle method to solve the Navier-Stokes system. *Numer. Math.*, 57, 805–827.

Crow, S. C. (1970). Aerodynamic sound emission as a singular perturbation problem. *Studies in Applied Mathematics*, XLIX(1), 21–44.

Daeninck, G. (2000). *Local refinement in Lagrangian vortex particle methods*. Master's thesis, Université Catholique de Louvain. Advised by G. S. Winckelmans.

Degond, P. and Mas-Gallic, S. (1989). The weighted particle method for convection-diffusion equations, Part 1: The case of an isotropic viscosity. *Math. Comp.*, 53(188), 485–507.

Draghicescu, C. I. and Draghicescu, M. (1995). A fast algorithm for vortex blob interactions. *J. Comput. Phys.*, 116, 69–78.

Eldredge, J. D., Colonius, T. and Leonard, A. (2001a). A vortex particle method for compressible flow. *Submitted to J. Comput. Phys.*.

Eldredge, J. D., Leonard, A. and Colonius, T. (2001b). A general deterministic treatment of derivatives in particle methods. *Submitted to J. Comput. Phys.*.

Engquist, B. and Majda, A. (1977). Absorbing boundary conditions for the numerical simulation of waves. *Math. Comp.*, 31(139), 629–651.

Epton, M. A. and Dembart, B. (1995). Multipole translation theory for the three-dimensional Laplace and Helmholtz equations. *SIAM J. Sci. Stat. Comput.*, 16, 865–897.

Fishelov, D. (1990). A new vortex scheme for viscous flows. *J. Comput. Phys.*, 86, 211–224.

Gingold, R. A. and Monaghan, J. J. (1977). Smoothed particle hydrodynamics: Theory and application to non spherical stars. *Mon. Not. Roy. Astron. Soc.*, 181, 375–389.

Givoli, D. (1991). Non-reflecting boundary conditions. *J. Comput. Phys.*, 94, 1–29.

Greengard, L. and Rokhlin, V. (1987). A fast algorithm for particle simulations. *J. Comput. Phys.*, 73(2), 325–348.

Hald, O. H. (1979). Convergence of vortex methods for Euler's equations, II. *SIAM J. Numer. Anal.*, 16, 726–755.

Hardin, J. C. and Pope, D. S. (1994). An acoustic/viscous splitting technique for computational aeroacoustics. *Theoret. Comput. Fluid Dyn.*, 6, 323–340.

Howe, M. S. (1975). Contributions to the theory of aerodynamic sound, with application to excess jet noise and the theory of the flute. *J. Fluid Mech.*, 71(4), 625–673.

Kambe, T. (1986). Acoustic emissions by vortex motions. *J. Fluid Mech.*, 173, 643–666.

Knio, O. M., Collorec, L. and Juvé, D. (1995). Numerical study of sound emission by 2D regular and chaotic vortex configurations. *J. Comput. Phys.*, 116, 226–246.

Koumoutsakos, P., Leonard, A. and Pépin, F. (1994). Boundary conditions for viscous vortex methods. *J. Comput. Phys.*, 113, 52–61.

Krishnan, A. and Ghoniem, A. F. (1992). Simulation of rollup and mixing in Rayleigh-Taylor flow using the transport-element method. *J. Comput. Phys.*, 99, 1–27.

Lamb, H. (1932). *Hydrodynamics*. Cambridge University Press, 6th edn.

Lee, D. J. and Koo, S. O. (1995). Numerical study of sound generation due to a spinning vortex pair. *AIAA J.*, 33, 20–26.

Lele, S. K. (1997). Computational aeroacoustics: A review. *AIAA Paper 97-0018*.

Leonard, A. (1980). Vortex methods for flow simulation. *J. Comput. Phys.*, 37(3), 289–335.

Lighthill, M. J. (1952). On sound generated aerodynamically I. General theory. *Proc. Roy. Soc. Lond. Ser. A*, 211, 564–587.

Lyamshev, L. M. and Skvortsov, A. T. (1988). Sound ratiation by localized vortices in a slightly compressible medium (review). *Sov. Phys. Acoust.*, 34, 447–459.

Lyrintzis, A. S. (1994). Review: The use of Kirchhoff's method in computational aeroacoustics. *J. Fluids Eng.*, 116, 665–676.

Melander, M. V., Zabusky, N. J. and McWilliams, J. C. (1988). Symmetric vortex merger in two dimensions: causes and conditions. *J. Fluid Mech.*, 195, 303–340.

Mitchell, B. E., Lele, S. K. and Moin, P. (1995). Direct computation of the sound from a compressible co-rotating vortex pair. *J. Fluid Mech.*, 285, 181–202.

Möhring, W. (1978). On vortex sound at low Mach number. *J. Fluid Mech.*, 85, 685–691.

Möhring, W. (1979). Modelling low Mach number noise. In *Mechanics of Sound Generation* (edited by E.-A. Müller). Springer-Verlag.

Möhring, W. (1997). Sound generation from convected vortices. Unpublished.

Monaghan, J. J. (1985). Particle methods for hydrodynamics. *Comp. Phys. Rep.*, 3, 71–124.

Monaghan, J. J. (1989). On the problem of penetration in particle methods. *J. Comput. Phys.*, 82, 1–15.

Monaghan, J. J. (1997). SPH and Riemann solvers. *J. Comput. Phys.*, 136, 298–307.

Monaghan, J. J. and Gingold, R. A. (1983). Shock simulation by the particle method SPH. *J. Comput. Phys.*, 52, 374–389.

Müller, E.-A. and Obermeier, F. (1967). The spinning vortices as a source of sound. In *Proc. Conf. on Fluid Dynamics of Rotor and Fan Supported Aircraft at Subsonic Speeds*, AGARD CP-22.

Obermeier, F. (1984). Aerodynamic sound generation caused by viscous processes. *J. Sound Vib.*, 99, 111–120.

Oxford English Dictionary (1989). 2nd edn. Ed. Simpson, J. A. and Weiner, E. S. C.

Pierce, A. D. (1989). *Acoustics: An Introduction to its Physical Principles and Applications*. Acoustical Society of America, Woodbury, New York.

Ploumhans, P. and Winckelmans, G. S. (2000). Vortex methods for high-resolution simulations of viscous flow past bluff bodies of general geometry. *J. Comput. Phys.*, 165, 354–406.

Pothou, K. P., Voutsinas, S. G., Huberson, S. G. and Knio, O. M. (1996). Application of 3-d particle method to the prediction of aerodynamic sound. In *Vortex Flows and Related Numerical Methods II*, vol. 1 of *ESAIM*.

Powell, A. (1964). Theory of vortex sound. *J. Acoust. Soc. Am.*, 36(1), 177–195.

Puckett, E. G. (1993). Vortex methods: An introduction and survey of selected research topics. In *Incompressible Computational Fluid Dynamics: Trends and Advances* (edited by M. D. Gunzburger and R. A. Nicolaides), pages 335–408. Cambridge University Press.

Raviart, P. A. (1983). An analysis of particle methods. In *Numerical Methods in Fluid Dynamics* (edited by F. Brezzi), vol. 1127 of *Lecture Notes in Mathematics*, pages 243–324. Como.

Rayleigh, Lord (1894). *The Theory of Sound*. Macmillan.

Sarpkaya, T. (1989). Computational methods with vortices—The 1988 Freeman Scholar Lecture. *J. Fluids Eng.*, 111, 5–52.

Schoenberg, I. J. (1973). *Cardinal Spline Interpolation*. SIAM, Philadelphia.

Shariff, K. and Leonard, A. (1992). Vortex rings. *Ann. Rev. Fluid Mech.*, 24, 235–279.

Sommerfeld, A. (1964). *Partial Differential Equations in Physics*, vol. 6 of *Lectures on Theoretical Physics*. Academic Press, New York.

Soteriou, M. C. and Ghoniem, A. F. (1998). On the effects of the inlet boundary condition on the mixing and burning in reacting shear flows. *Combust. Flame*, 112, 404–417.

Stakgold, I. (1967). *Boundary Value Problems of Mathematical Physics*. Macmillan, New York.

Stüber, B. (1970). Radiation of sound and excitation of sound in solid bodies by vortices. *Acustica*, 23, 82–92.

Tang, S. K. and Ko, N. W. M. (1997). Sound generation by interaction of two inviscid two-dimensional vortices. *J. Acoust. Soc. Am.*, 102, 1463–1473.

Tang, S. K. and Ko, N. W. M. (2000). Sound sources in the interactions of two inviscid two-dimensional vortex pairs. *J. Fluid Mech.*, 419, 177–201.

Tsynkov, S. V. (1998). Numerical solution of problems on unbounded domains. A review. *Appl. Numer. Math.*, 27, 405–532.

Whitham, G. B. (1999). *Linear and Nonlinear Waves*. Wiley, New York.

Winckelmans, G. S. and Leonard, A. (1993). Contributions to vortex particle methods for the computation of three-dimensional incompressible unsteady flows. *J. Comput. Phys.*, 109(2), 247–273.

Yates, J. E. (1978). Application of the Bernoulli enthalpy concept to the study of vortex noise and jet impingement noise. *Tech. Rep. CR-2987*, NASA.